1. SILICON VIDICON IMAGING OF JUPITER 4100-8300Å: SPECTRAL REFLECTIVITY, LIMB-DARKENING, AND ATMOSPHERIC STRUCTURE

2. SIMULTANEOUS ULTRAVIOLET (0.36 μm) AND INFRARED (8-20 μm) IMAGING OF VENUS: PROPERTIES OF CLOUDS IN THE UPPER ATMOSPHERE

Thesis by

David Joseph Diner

In Partial Fulfillment of the Requirements

for the Degree of

Doctor of Philosophy

California Institute of Technology

Pasadena, California

1978

(Submitted 2 November 1977)

To my parents

with gratitude, and especially, with love

Persons attempting to find a motive in this narrative will be prosecuted; persons attempting to find a moral in it will be banished; persons attempting to find a plot in it will be shot.

BY ORDER OF THE AUTHOR.

- Mark Twain
The Adventures of Huckleberry Finn

ACKNOWLEDGMENTS

It is a pleasure to acknowledge the assistance given by numerous people on various aspects of this work. I am particularly indebted to my research advisor, James Westphal, whose helpful advice, supervision, generosity and infinite patience are greatly appreciated. The opportunities to use the Palomar observing facilities as well as some fascinating hardware were uniquely provided by our association, and if I have assimilated but a fraction of Professor Westphal's practical knowledge and expertise, then I have indeed been extremely fortunate.

I would like to thank Dr. Andrew Ingersoll for his guidance and valuable criticisms of my ventures into the field of planetary atmospheres. I am also indebted to other members of the Caltech faculty and staff: Drs. Duane Muhleman and Peter Goldreich for their helpful scientific and academic advice; Dr. Guido Münch for his assistance regarding the observational and theoretical aspects of radiative transfer; Dr. Alfred Ferrari for his help with the theory of least-squares and data analysis; Dr. George Rossman for providing access to his laboratory spectrophotometers; Dr. Gerry Neugebauer, Keith Matthews and Gordon Forrester and other members of the Caltech infrared group for their loan of much of the equipment used in the 8-20 μm observations; and Dr. Jerome Kristian for his insight into the peculiarities of silicon vidicons. I also thank Drs. Jay

Bergstralh, John Martonchik, Glenn Orton, and Fredric Taylor of the Jet Propulsion Laboratory for their constant encouragement and critical reading of the preliminary stages of this manuscript.

Thanks are due to many friends who accompanied me to Palomar and assisted with the observations: Janet Bailey, Bruce Bills, John Dvorak, Robert Harrison, Carol Lyon, Philip Nicholson, Carolyn Porco, Peter Schloerb, and Richard Terrile. It has been a pleasure to work with the night assistants of the 60-inch and 200-inch telescopes: Brad Bailey, Steve Barry, Juan Carrasco, Kevin Jordan, Gary Tuton, and Chip Williams. I appreciate the gracious efforts of the members of the Hale Observatories staff who helped to make my visits to Palomar enjoyable. For assistance with the design, development, and construction of electronics, hardware, and software I am grateful to Michael Carr, Richard Lucinio, Victor Nenow, Peter Schloerb, DeVere Smith, and Richard Terrile.

I would like to acknowledge the assistance and advice of Jan Scott in the drafting of illustrations. For typing the manuscript and seeing it through its final stages, I am indebted to Kay Campbell, Melissa Magdaleno, Brenda Parson, and Carol Storm.

Finally, I thank my family for their encouragement and love and for giving me confidence, support, and hope.

This research was funded by Grant NGL 05-002-003 of the National Aeronautics and Space Administration.

ABSTRACT

Part 1 presents the results of high spatial resolution area photometry of Jupiter in six continuum wavelength channels from 4100-8300Å. Spectral reflectivity and limb-darkening data in belts and zones are fitted by a simple semi-infinite homogeneous scattering model which provides a convenient parameterization of the results, as well as a determination of the spectral and spatial variations in the continuum single scattering albedo and information regarding the shape of the single scattering phase functions. It is found that belts are generally more backscattering than zones, particularly in the blue, and there is a trend toward increased forward scattering at longer wavelengths. The numerical results are compared to earlier ground-based observations of jovian limb-darkening (Harris, 1961; Binder and McCarthy, 1973; Pilcher and Kunkle, 1976) and significant disagreement is found in some cases. Extrapolations of the limb-darkening data to 12° phase angle are compared with the results of the Pioneer 10 imaging photopolarimeter (IPP) experiment (Tomasko et al., 1976). Although there is quantitative disagreement between the vidicon results and the IPP data, the ground-based and Pioneer 10 results show the same relative spectral and regional trends in the shape of the limb structure profiles from the blue to the red and between a belt and a zone. The limb-darkening profiles are also compared to models derived from measurements of the spatial distribution

of equivalent width of the H_2 4-0 S(1) quadrupole line (Cochran, 1976). It is found that these models fare reasonably well in the South Tropical Zone but are much too limb-darkened relative to the data in the North Equatorial Belt. A discussion of the possible causes of the differences between the vidicon data and other ground-based, Pioneer 10, and spectroscopic results is presented.

Some numerical examples of limb-darkening expected from simple models are presented. In particular, the effects of Rayleigh scattering, either by a fine, colored dust, or by the gaseous atmosphere on the spectral characteristics of limb-darkening are investigated. It is found that the observed backscattering may be explained by a combination of molecular scattering and scattering by small dust particles, and the increased forward scattering in the red arises from the λ^{-4} dependence of Rayleigh scattering optical depth and inclusion of forward scattering cloud particles. Such a model works reasonably well in the North Equatorial Belt, but predicts a spectral variation in limb-darkening that is greater than the observations imply for the South Tropical Zone.

Part 2 discusses high spatial resolution images of Venus which were obtained in the 0.36 μm and 8-20 μm spectral regions throughout the 1974, 1975, and 1977 apparitions. The observing system, method of image acquisition, and data reduction and processing techniques are presented along with a discussion of the spectral, temporal, and spatial characteristics of the infrared and ultraviolet flux from

the planet. The infrared data are compared with previous ground-based results obtained at lower spatial and spectral resolution (Sinton and Strong, 1960; Murray et al., 1963; Westphal et al., 1965; Ingersoll and Orton, 1974) and Venera 9 and 10 infrared radiometer results (Ksanfomality et al., 1976).

Day-night contrasts in equatorial infrared flux were observed in images in which the evening and morning terminators were near the central meridian. A systematic increase in 8-14 μm flux associated with the emergence of the atmosphere from daylight into evening was observed, and is shown to exhibit significant day-to-day variability. The data also show that the daytime side of the morning terminator is warmer than the dark side, but this night-day asymmetry is systematically smaller than the day-night brightening seen in the Venus evening.

South and north infrared polar anomalies similar to the one observed near the Venus south pole by Murray et al. (1963) have been observed during the 1974 and 1975 apparitions, respectively. The observations indicate that the feature is most prominent between Venus midnight and dawn.

The infrared limb-darkening in the equatorial and polar directions are compared and it is seen that the magnitude and spectral variation of the polar darkening are in general greater than the equatorial darkening. The magnitude of the equatorial darkening is consistent with a temperature lapse rate of roughly -3°K/km,

assuming a model in which aerosol is distributed exponentially and mixed homogeneously with the atmospheric gas.

Evidence for a correlation between features observed in simultaneous infrared (8-14 μm) and ultraviolet (0.36 μm) images has been found. The sense of the correlation is such that bright UV markings correspond to bright (warm) IR features, and similarly, dark UV markings correspond to dark (cool) IR features. This result implies that dark UV clouds are higher or denser than the bright regions.

CONTENTS: Part 1

FIGURES: Part 1

FIGURES: Part 1 (Continued)

FIGURES: Part 1 (Continued)

TABLES: Part 1

CONTENTS: Part 2

FIGURES: Part 2

FIGURES: Part 2 (Continued)

TABLES: Part 2

Part 1

SILICON VIDICON IMAGING OF JUPITER 4100-8300Å: SPECTRAL REFLECTIVITY, LIMB-DARKENING, AND ATMOSPHERIC STRUCTURE

Chapter 1

INTRODUCTION

"Where shall I begin, please your Majesty?"
he asked.
"Begin at the beginning," the King said, gravely,
and go on until you come to the end: then stop."

- Lewis Carroll
Alice's Adventures in Wonderland

The center-to-limb variation in intensity across the disk of Jupiter and its spectral dependence at visible wavelengths are governed by the nature and distribution of particles and gases which absorb and scatter in the planet's atmosphere. Both the absolute reflectivity and limb-darkening (or brightening) of a given region are determined by the single scattering phase functions of the gases and aerosols which are present, the vertical layering of clouds and gas, and the relative optical depths of the various atmospheric constituents. In collaboration with broadband spacecraft observations of the angular distribution of reflected sunlight at many phase angles (Tomasko et al., 1974; Tomasko et al., 1976), measurements of the center-to-limb variation in the equivalent widths of gaseous absorption features (Bergstralh, 1972; Woodman, 1976; Cochran et al., 1976), and input regarding atmospheric chemistry and the expected levels of cloud formation (Weidenschilling and Lewis, 1973), narrowband photometry across isolated regions provides information that is of considerable value in the development and constraint of physical models of the jovian visible cloud structure.

Absolute reflectivity data and limb-darkening curves have been obtained in six continuum wavelength channels from 4100 to 8300Å for the North Tropical Zone, North Equatorial Belt, South Equatorial Belt, and South Tropical Zone. The channels are placed so as to avoid strong absorption features in the jovian spectrum. In the following chapters, the observing system and the reduction of the two-dimensional data to spatially resolved absolute reflectivities are described, and attention is focused upon the possible sources of error in the relative as well as absolute brightness calibrations. Although the largest source of error resides in the absolute photometric calibration, there is excellent agreement between the central meridian reflectivity data presented here and the observations of Orton (1975a).

Analysis of the limb-structure data indicates that the single scattering phase function of some atmospheric constituent with appreciable optical depth exhibits enhanced backscatter for wavelengths shortward of $\sim$ 5000Å. This backscatter is more pronounced in belts than in zones. Equilibrium chemical models (Weidenschilling and Lewis, 1973) suggest that the main cloud constituents are in the solid phase, so one may expect that the aerosol particles are nonspherical; therefore, the observed backscatter probably should not be attributed to the glory phenomenon associated with spherical droplets. Instead, the data are discussed in connection with simple atmospheric models which rely upon Rayleigh scattering to account for the observed backscatter and spectral dependence of the

reflectivity and limb-darkening. Future lines of research which may be used to evaluate these models further are suggested.

Quantitative measurements of the scattering properties of a planetary atmosphere, such as the data presented here, are useful for investigating a number of issues. In addition to information regarding the cloud structure *per se*, these include: 1) the vertical distribution of solar energy deposition and its influence on thermal structure; 2) the interpretation of spectroscopic data in terms of absolute abundances of optically active molecules; and 3) the atmospheric energy budget and magnitude of internal energy sources. The latter question has been discussed in some detail in a global sense for Jupiter (see Ingersoll *et al.*, 1975 for a review), but with the procurement of spatially resolved visible and infrared photometry, the belt vs. zone energy balance may be addressed.

Present understanding of the scattering properties of Jupiter's atmosphere is rudimentary, and the questions outlined above are only beginning to be answered. Earth-based and spacecraft observations will continue to help unravel the jovian atmospheric structure. Hopefully, data of the type presented in the following chapters will play an integral role in such studies.

Chapter 2

OBSERVING SYSTEM

When the blazing sun is gone
When he nothing shines upon,
Then you show your little light,
Twinkle, twinkle, all the night.

- Jane Taylor
The Star

Jupiter was observed on several nights during the fall of 1975 at the Cassegrain focus of the Palomar 60-inch telescope. Direct digital imaging was accomplished with an RCA type 4532 silicon diode array TV camera tube. A detailed description of the tube and data system may be found in McCord and Westphal (1972) and Westphal (1973). The following represents a brief description of the salient features and items specifically related to these observations.

The primary elements of the silicon vidicon tube, or SIVIT, are a photoconducting target consisting of a grid of discrete silicon diodes, and an electron gun which provides the beam current for target readout. Each diode is back-biased and acts as a tiny capacitor which discharges due to diffusion of charge carriers created by photons incident upon the target. Following an exposure, the target is scanned by the electron beam, which recharges each diode creating a flow of current. This current is proportional to the incident photon flux and constitutes the video signal. Focusing and deflection of the electron beam are controlled by magnetic fields. In practice, the readout beam is defocused to include a number of diodes in each resolution element. This practice improves the signal-to-noise ratio and eliminates Moire

patterns which may result from misregistration of the readout raster with the discrete diode array. The readout format is a raster of 256 lines with 256 samples/line in a 10 x 10 mm area on the silicon target.

The target is prepared in a uniform manner for each exposure by saturation with a bright light, followed by erasure with a fixed number of readout scans. This procedure ensures that the target is in a repeatable, uniform state in readiness for the next data frame, and removes any trace of a residual image which may have been retained from the previous exposure. After each exposure, the video signal is read out and amplified, then digitized to 12-bits and written on digital magnetic tape using a Cipher Data Products 9-track 800 bits-per-inch tape recorder. A digital scan converter and television monitor permit real-time display of each incoming data frame.

In order to decrease thermal dark current, the SIVIT and video preamplifier were housed in a cold box and cooled with dry ice. A transparent quartz window was located at the entrance port of the cold box, and was mounted in a copper ring wrapped with a high resistance Nichrome heating coil to preclude frost formation. The bulk of the electronics - including the video amplification and scan control circuits, an oscilloscope for line-by-line display of each frame, plus the scan converter, television monitor, and tape recorder - was contained in an external rack and communicated with the cold box via shielded cables. A photometer base was sandwiched between the cold box and the face plate of the telescope. This photometer base con-

tained a swinging 45° flat mirror which was used to intercept the incoming light for diversion into the finding optics and which was positioned out of the way in the imaging mode; supported the electromagnetically operated shutter mechanism; contained the light and fiber optics arrangement which was used to saturate the target during an erase cycle; and held a 1" Barlow lens which converted the f/8.75 beam from the telescope's secondary to f/16 to increase the image size. Spectrolab 1" and Oriel 2" interference filters were contained in interchangeable slides or rotating wheels and also housed within the base assembly.

The combination of external optics and the sampling density of target readout with a net focal ratio of f/16 resulted in an average plate scale of about 0.33 arcsec/40 μm resolution element. The plate scale was measured by recording double exposures of a star which was moved a known angular distance between openings of the shutter. The plate scale was found to vary by a few percent from one wavelength to another and differed slightly along the horizontal and vertical axes of the target due to unequal H and V deflections of the readout beam. These differences in picture element (pixel) spacing presented no real problem and their values and associated errors were taken into account in the data reduction. Jupiter's equatorial diameter was just under 50 arcsec at the time of these observations, so the sample spacing was nearly 1/150 of the disk diameter. However, atmospheric seeing proved to be the limiting factor in determining the ultimate spatial resolution. Since much

of the information contained in measurements of the center-to-limb variation in intensity is found near the planetary limbs, good seeing is absolutely essential. The smearing of data due to a point-spread function of finite width is most severe near the limbs where the absolute value of the slope increases markedly. In principle, the images can be deconvolved if the point-spread function is known; however, seeing is variable both spatially and temporally and there is no guarantee that the smearing function determined by imaging a point source (a star) is appropriate for a particular planetary image. In addition, the deconvolution process tends to enhance any noise present in the data. In light of the risks involved, the decision was made to utilize only those images obtained under the best seeing conditions and to ignore data close to the limbs. The criterion for choosing the viewing angle beyond which data are not considered is discussed in a later chapter. Selection of nights with clear skies (and thus well-determined extinction corrections) as well as good seeing (1-2 arcsec, determined from measured stellar point-spread profiles) limited the data set to images recorded on UT October 25 and November 16. The jovian phase angles for these dates, and the effective wavelengths and full width at half-maximum (FWHM) bandwidths of the filter set are summarized in Table I. The spectral transmission characteristics of each filter were measured on a Cary 17I recording spectrophotometer. Rejection of light at wavelengths other than those included in the nominal bandpasses was quite good, and contributions due to filter leaks were less than 0.3%.

TABLE I

Summary of vidicon observations

Date	Jovian phase angle	Filter	FWHM bandpass
UT 25 Oct. 1975	2°.6	4865Å	40Å
"	"	5810Å	200Å
"	"	7440Å	150Å
UT 16 Nov. 1975	6°.9	4115Å	160Å
"	"	5460Å	220Å
"	"	8290Å	55Å

Chapter 3
DATA REDUCTION

It is a capital mistake to theorize before one has data.

- Sir Arthur Conan Doyle
"A Scandal in Bohemia,"
from The Adventures of
Sherlock Holmes

Four stages of reduction of the vidicon data were necessary before the images were in a form from which calibrated center-to-limb scans could be extracted: 1) subtraction of a zero offset level; 2) correction for pixel-to-pixel gain variations, or "flat field" response; 3) corrections for the small departures from linearity; and 4) conversion of data numbers to intensity values by standard star photometry. Each of these shall be considered in turn.

The zero level in the SIVIT was measured by recording frames in which the target was not exposed to light but in all other respects were identical to actual data frames. Particular attention was paid to the time delay between completion of an erase cycle and readout of the tube; during this time the target becomes nonuniformly backlighted by photons from the heated filament of the electron gun. Although for the short exposure times involved (1-10 sec) this effect is practically negligible, the time delay was kept constant whether or not an exposure was made so that the backlighting was subtracted out during this stage of the calibration. Constancy of the time delay between conclusion of an exposure or erase cycle and target readout also insures that any signal due to thermally induced dark

current will be identical in all frames. More significant and worrisome changes in the zero level occurred as the tube warmed during sublimation of the dry ice coolant; this problem was of particular concern in the arrangement used here in which the cold box was mounted upside-down. This effect was assessed by continually monitoring the appearance of zero frames (ZF's) in real-time at the low bit levels; small variations were detected in this manner. To minimize errors due to low-frequency periodic or secular changes in the zero level, zero frames were recorded frequently and dovetailed with actual data frames, and similar consecutive ZF's were averaged together and used to "dezero" only intervening data frames. Deviations in data number from one ZF to another in a group introduced an uncertainty of less than 0.1% to the data.

Variations in the pixel-to-pixel gain across the target were assessed by recording images of a uniformly illuminated diffuse source, or flat field (FF). The source used was the daytime sky, and several FF's were recorded at each wavelength during both the afternoon preceding and morning following a night of observation. Nonuniformity in data number across frames illuminated in such a manner can arise from a number of causes. In addition to statistical noise, these include: 1) variation in sensitivity of a particular group of diodes; 2) variation in the electron beam landing pattern; and 3) optical effects such as vignetting or spatial transmission variations across a filter or lens in the light path. FF's were

found to remain stable throughout a typical 16-hour observing period, exhibiting random fluctuations at about the 1% level. In reducing the data, FF's were subjected to the same dezeroing process applied to actual data frames. Each data frame was then divided by the normalized average of all FF's at its particular wavelength. This process appears to be photon noise limited and contributes an uncertainty of $\sim$ 1.0% to the Jupiter data.

Although the SIVIT should, in principle, have a linear response, some deviations from linearity have been found. In theory, the data number, or DN, of a picture element should be proportional to the incident intensity and exposure time, i.e.,

$$DN \propto I \cdot t \quad . \tag{1}$$

However, experience has shown that for a variety of detectors the behavior may be better represented empirically by

$$DN = CI^{\gamma_1} t^{\gamma_2} \tag{2}$$

where in the classic case of photographic emulsions the exponents may differ markedly from unity. The condition in which the gammas are unequal, such that variation of the light intensity by a certain factor does not have the same effect on the recorded signal as a similar variation in exposure time, is known as reciprocity failure. γ_1 and γ_2 were experimentally determined in the laboratory for the SIVIT used in these observations by illuminating the target with a uniform diffuse source and either keeping the exposure time constant

and varying the intensity (to measure γ_1) or by varying exposure time at a constant intensity (for γ_2). The illumination level was continuously monitored with a photomultiplier and pulse counter. The gammas were determined by fitting a straight line by least-squares to a plot of log DN vs. log I or log DN vs. log t; the slopes are γ_1 and γ_2, respectively. In the experimental determination of γ_1 it was necessary for the vidicon and photomultiplier to be illuminated by photons of the same wavelength since the color temperature of the light source was dependent upon the applied voltage; reduction of the voltage so as to result in diminution in intensity by a certain factor at a given wavelength λ_1 would not necessarily yield a reduction by the same factor at another wavelength λ_2. γ_1 and γ_2 were measured at a variety of locations across the target and within their uncertainties are constant across the photocathode and do not depend strongly on wavelength. The measurements yielded the following values: $\gamma_1 = 0.959 \pm 0.002$ and $\gamma_2 = 0.977 \pm 0.002$. The uncertainties were determined from the slight variations of γ_1 and γ_2 across the target and from repeated tests on several occasions. The deviations from linearity probably arise, at least in part, from the fact that a single readout of the vidicon target does not completely erase the extant signal. Although the measured gammas are close to unity, significant errors can be incurred if the proper corrections are not made.

Combining equations (1) and (2), it is seen that the corrected data numbers, DN_c, are related to the measured values, DN_m, by

$$DN_c = \left(DN_m^{1/\gamma_1}\right)\left(t^{1-\gamma_2/\gamma_1}\right) \quad . \tag{3}$$

The experiments reveal a strong correlation between the gammas, so that the ratio γ_2/γ_1 is much better determined than either of the values individually. Since the laboratory measurements were carried out at dry ice temperature, and the tube demonstrates considerable long-term stability, it is reasonable to adopt the laboratory values in reduction of the data obtained at the telescope. The uncertainties in γ_1 and γ_2, combined in a statistical sense with the flat field and zero level uncertainties, yield a net internal accuracy of 1.5 - 2.0% in relative measurement of intensity across the disk of Jupiter.

For the purpose of comparing the observed limb structure with theoretical predictions from models, it is vital to measure absolute reflectivities as well as relative variations across the disk. The standard star ξ^2 Cet was observed at each wavelength to provide the absolute flux calibrations. The ξ^2 Cet/α Lyr flux ratios of Oke (1964) and the α Lyr spectrum of Oke and Schild (1970) were used to calculate absolute intensities. Exponential extinction with air mass according to Beer's law was assumed and extinction coefficients were determined at each wavelength either by imaging ξ^2 Cet at a number of air masses or by observing the star at two widely separated zenith angles

and imaging the satellite J4 at a larger number of air masses. In the latter case, the linear least-squares best fit extinction coefficient from the J4 measurements was used as an a priori estimate of this parameter. All star and satellite frames were corrected for zero level, flat field response, and nonlinearities in the same manner as Jupiter frames. The total flux received from a star or satellite was calculated by adding all data numbers within a circle of a given radius and subtracting from the DN in each pixel an average sky level determined from points in an annulus lying outside this circle. Experimental uncertainties in these total flux values were derived by using different values of the radius as well as varying the nonlinearity factors γ_1 and γ_2 within their experimental uncertainties. The absolute spectrum of ξ^2 Cet and the Arvesen et al, (1969) solar spectrum were weighted by each of the filter spectral characteristics and the vidicon spectral responsivity. The latter was taken from the published RCA specifications for the vidicon tube. Applying the estimated errors in each of the quantities involved results in a systematic uncertainty of $\pm$ 5% in all of the reflectivities along any one limb structure curve.

Chapter 4

RESULTS OF OBSERVATIONS

"What's the good of Mercator's North Poles and Equators
Tropics, Zones and Meridian Lines?"
So the Bellman would cry: and the crew would reply,
"They are merely conventional signs!"

- Lewis Carroll
The Hunting of the Snark

The results are presented for each wavelength as values of I/F, where I is the specific intensity of Jupiter and πF is the incident solar flux. These values are calculated from the relation

$$\frac{I}{F} = \frac{DN_{Jup}}{\Sigma DN_{star}} \cdot \frac{t_{star}}{t_{Jup}} \cdot \frac{\pi F_{star}}{\pi F} \cdot \left(\frac{R}{a}\right)^2 \cdot \frac{\pi}{A} \qquad (4)$$

where

DN_{Jup} = data number of a picture element on the jovian disk

ΣDN_{star} = sum of data numbers under the standard star point-spread function

t_{Jup} = exposure time of Jupiter frame

t_{star} = exposure time of standard star frame

πF_{star} = standard star absolute spectral irradiance

R = Sun-Jupiter distance at time of Jupiter observation

a = Earth-Sun distance at time of measurement of πF

A = angular area of one pixel.

For comparison with theoretical curves and parameterization of the data in terms of simple scattering models, the spatially resolved reflectivity values are considered to depend on three geometric variables: μ_o, the cosine of the angle between the local normal and

direction to the illuminating source (the Sun); μ, the cosine of the angle between the local normal and direction to the observer; and $\cos(\varphi - \varphi_o)$, the cosine of the local azimuth difference between the directions to the source and the observer. These geometric variables, as well as planetocentric longitude relative to the central meridian, Φ_{CM}, were calculated for all points lying within four latitude bins on the planet. Effects of the oblateness of Jupiter, differences between the planetocentric latitudes of the Sun and the Earth, and the inclination of Jupiter's pole were included in the geometric computations. The latitude bins chosen are 18°N - 19°N, 13°N - 14°N, 1°S - 2°S, and 22°S - 23°S, and correspond, respectively, to the North Tropical Zone (NTrZ), the North Equatorial Belt (NEB), the northern part of the South Equatorial Belt (SEB), and the southern component of the South Tropical Zone ($STrZ_s$). A 5810Å north-south scan identifying various regions including those specifically considered in the analysis is displayed in Figure 1. The geometry is referenced to a single datum on a particular image: the disk center, i.e., the pixel location where $\mu = 1$. A first guess for the location of this point is arrived at by making use of the known plate scale and measuring inward from the limbs. This guess is refined by verifying that on the average the limb structure curves satisfy the Helmholtz reciprocity principle, which requires that:

$$\mu I(\mu,\mu_o,\varphi - \varphi_o)/F = \mu_o I(\mu_o,\mu,\varphi_o - \varphi)/F \quad . \qquad (5)$$

Figure 1. - North-south scan from a 5810Å silicon vidicon image of Jupiter recorded on UT 25 October 1975. Various regions including those considered in the limb-darkening analysis are identified as follows: NTeZ = North Temperate Zone; NTeB = North Temperate Belt; NTrZ = North Tropical Zone; NEB = North Equatorial Belt; SEB = South Equatorial Belt; $STrZ_n$ = northern component of the South Tropical Zone; STrB = South Tropical Belt; $STrZ_s$ = southern component of the South Tropical Zone.

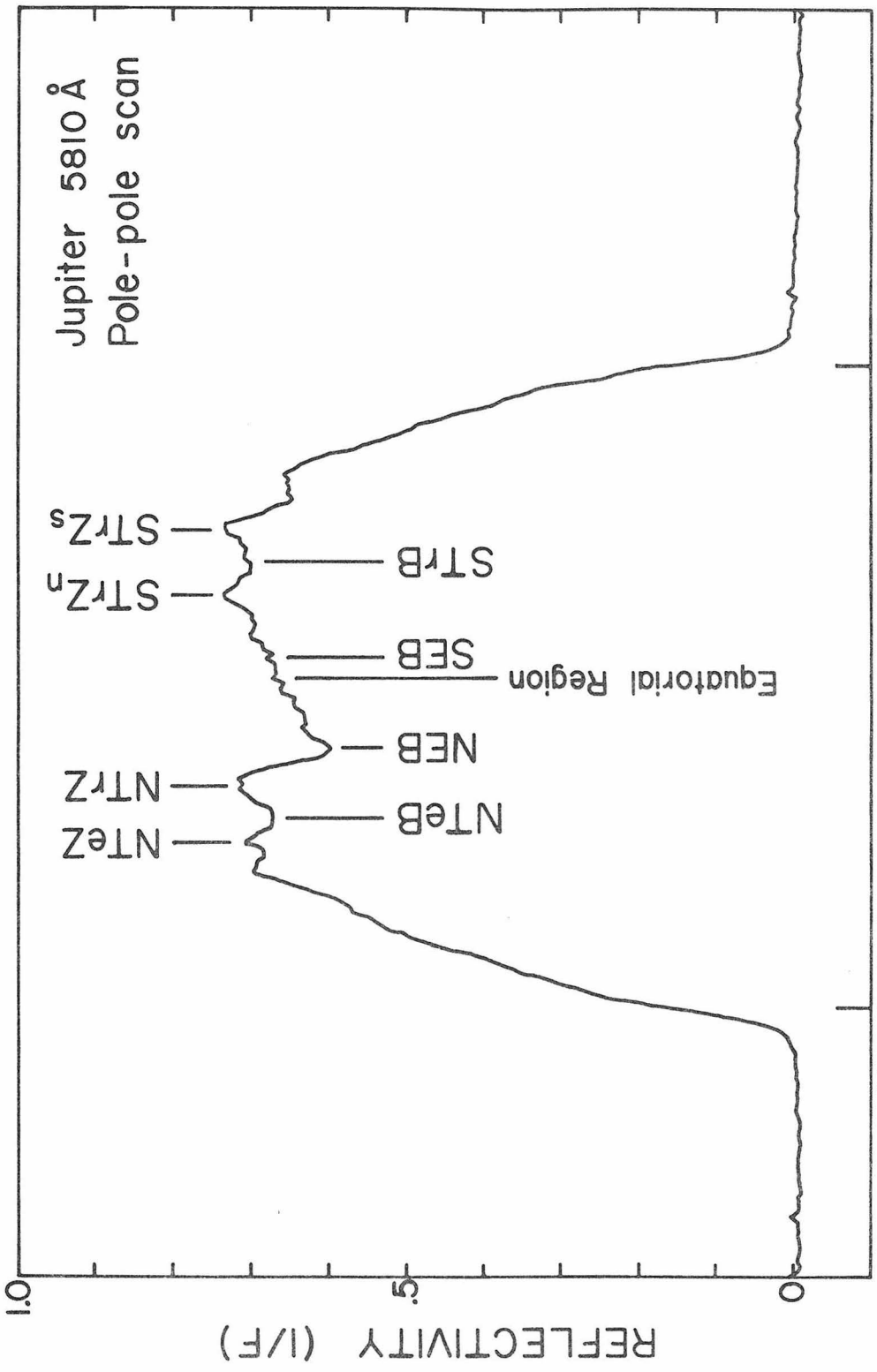
Jupiter 5810 Å
Pole-pole scan
REFLECTIVITY (I/F)
1.0
.5
0
North limb
South limb
NTeZ
NTeB
NTrZ
NEB
Equatorial Region
SEB
STrB
STrZn
STrZs

Fig. 1

In cases where this relation was not satisfied to within the random uncertainties, the central datum was shifted accordingly. The initial guess was rarely in error by more than 2 pixel widths from the final location. It is felt that utilization of an entire image in the determination of positional control yields considerably greater accuracy and precision than are possible using a single aperture detector and scanning or sampling only localized regions of the planetary disk.

The limb structure curves in each wavelength channel for the four latitude bins are shown in Figures 2-7. In each case data from two independent images taken several minutes apart are superimposed. In view of the difficulty in displaying the values of I/F vs. the three variables μ, μ_o and $\cos(\varphi - \varphi_o)$, the sine of longitude relative to the central meridian has been chosen as the abscissa. Data at points where $\left|\sin\Phi_{CM}\right| > 0.92$ have been excluded due to the adverse smearing effects of seeing near the planetary limb. The rationale behind this restriction is illustrated by the following experiment. A theoretical limb-darkening curve for a semi-infinite, homogeneous and isotropically scattering atmosphere with single scattering albedo $\tilde{\omega}_o = 0.99$ was calculated by a method which will be described below. The shape of the limb-darkening is typical of the solutions found from actual data. A model disk radius comparable to the angular size of Jupiter on the dates of observation was assumed, and the limb-darkening function was convolved with gaussian curves of 1 arcsec and 2 arcsec half-widths in

Figure 2. - Reflectivity vs. sine of longitude relative to the central meridian for the jovian NTrZ, NEB, SEB and $STrZ_s$. The plus signs and crosses represent data from two 4115Å vidicon images recorded several minutes apart. The random uncertainty in an individual data point is roughly 1.5 - 2.0% as discussed in the text. Best-fit scattering models are represented by the solid lines.

Figures 3-7. - Same as Figure 2, except for 4865, 5460, 5810, 7440 and 8290Å, respectively.

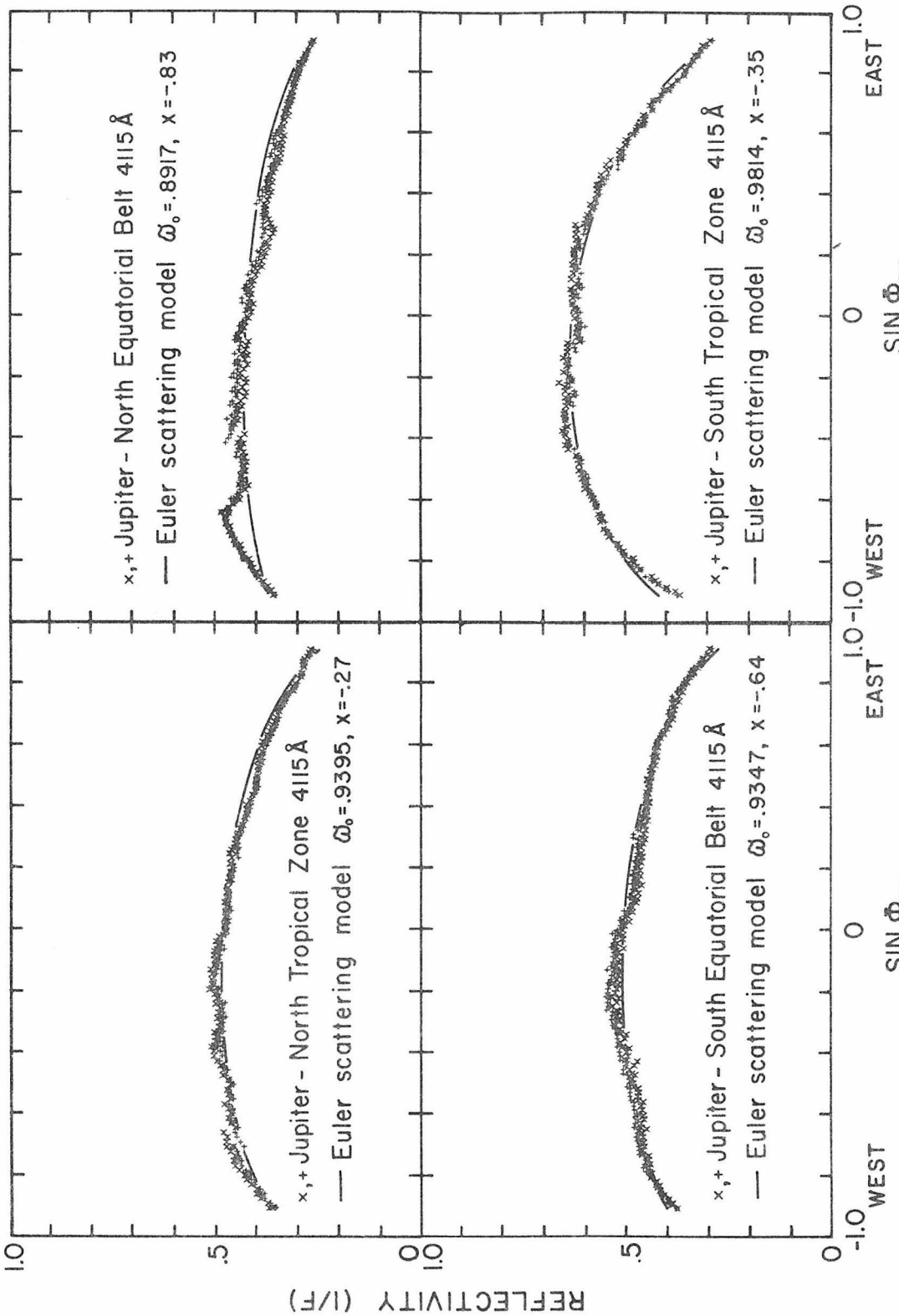
x,+ Jupiter - North Equatorial Belt 4115 Å
— Euler scattering model ϖ₀=.8917, x=-.83
x,+ Jupiter - North Tropical Zone 4115 Å
— Euler scattering model ϖ₀=.9395, x=-.27
x,+ Jupiter - South Tropical Zone 4115 Å
— Euler scattering model ϖ₀=.9814, x=-.35
x,+ Jupiter - South Equatorial Belt 4115 Å
— Euler scattering model ϖ₀=.9347, x=-.64
REFLECTIVITY (I/F)
1.0
.5
0
-1.0 WEST
0
SIN Φ_CM
1.0 EAST

Fig. 2

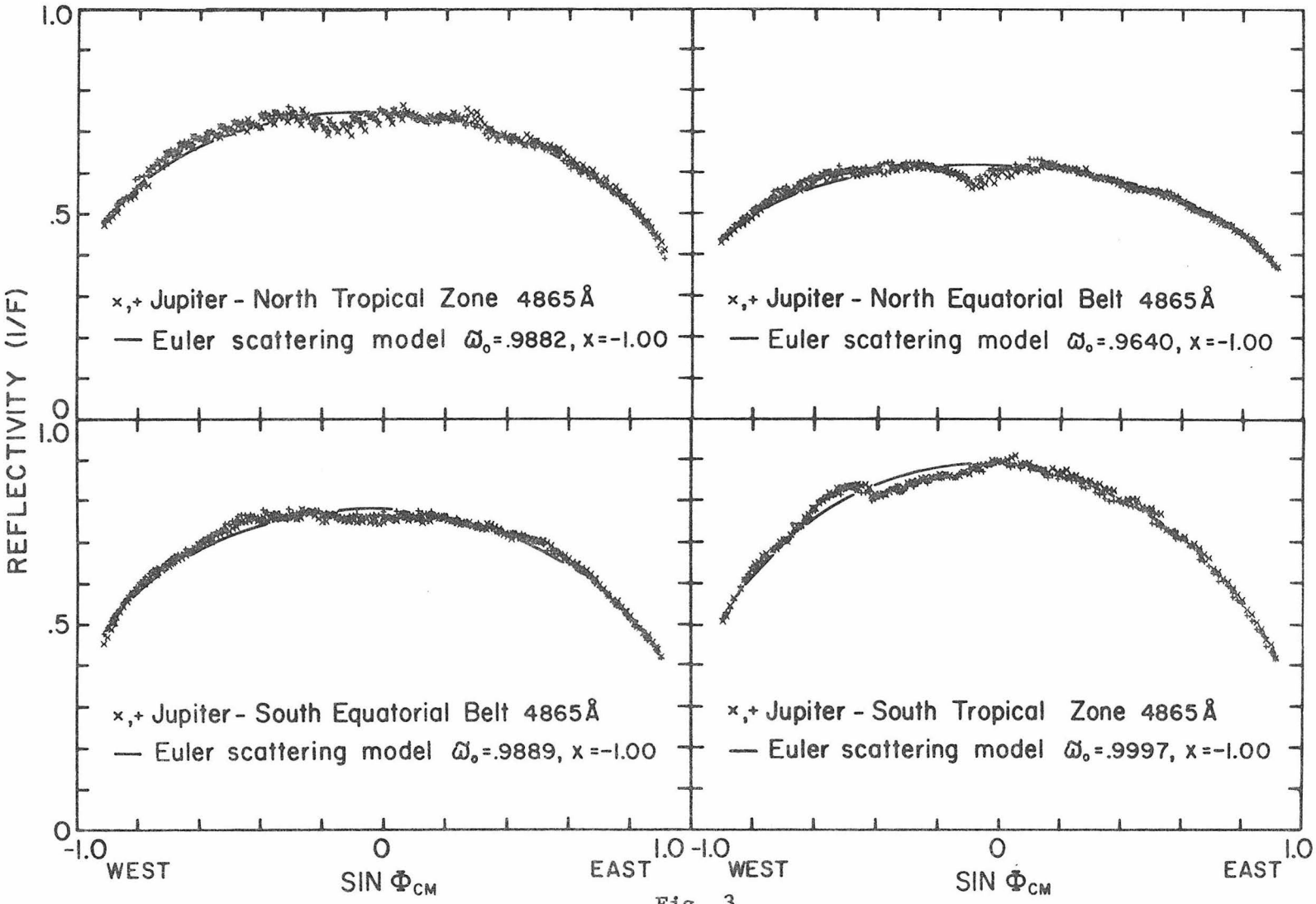
REFLECTIVITY (I/F)
1.0
.5
0
×,+ Jupiter - North Tropical Zone 4865 Å
— Euler scattering model ϖ₀=.9882, x=-1.00
×,+ Jupiter - North Equatorial Belt 4865 Å
— Euler scattering model ϖ₀=.9640, x=-1.00
×,+ Jupiter - South Equatorial Belt 4865 Å
— Euler scattering model ϖ₀=.9889, x=-1.00
×,+ Jupiter - South Tropical Zone 4865 Å
— Euler scattering model ϖ₀=.9997, x=-1.00
-1.0
WEST
0
SIN Φ_CM
1.0
EAST

Fig. 3

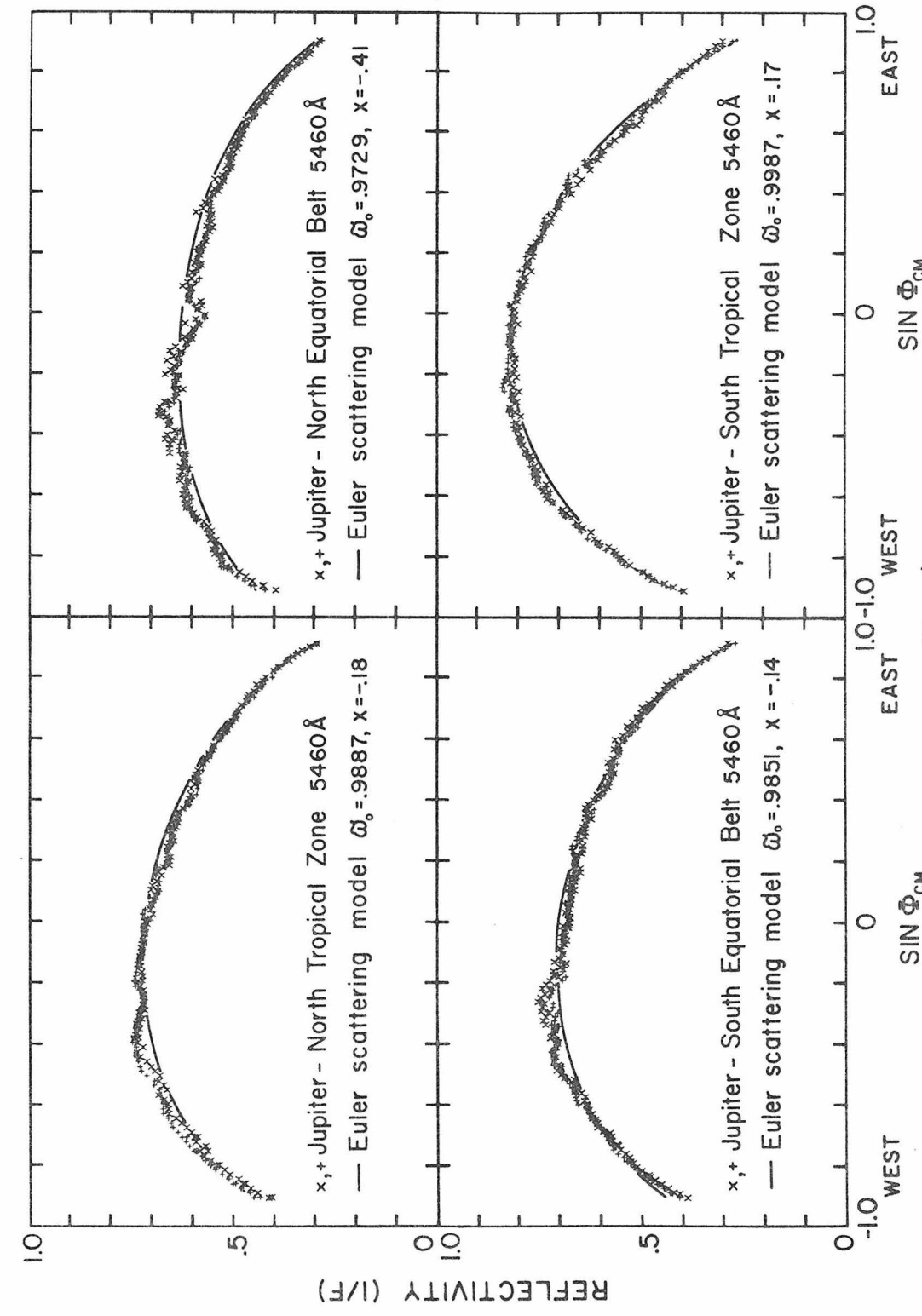
REFLECTIVITY (I/F)
1.0
.5
0
x,+ Jupiter - North Tropical Zone 5460Å
— Euler scattering model ω₀=.9887, x=-.18
x,+ Jupiter - North Equatorial Belt 5460Å
— Euler scattering model ω₀=.9729, x=-.41
x,+ Jupiter - South Equatorial Belt 5460Å
— Euler scattering model ω₀=.9851, x=-.14
x,+ Jupiter - South Tropical Zone 5460Å
— Euler scattering model ω₀=.9987, x=.17
-1.0 WEST
0
SIN Φ_CM
1.0 EAST

Fig. 4

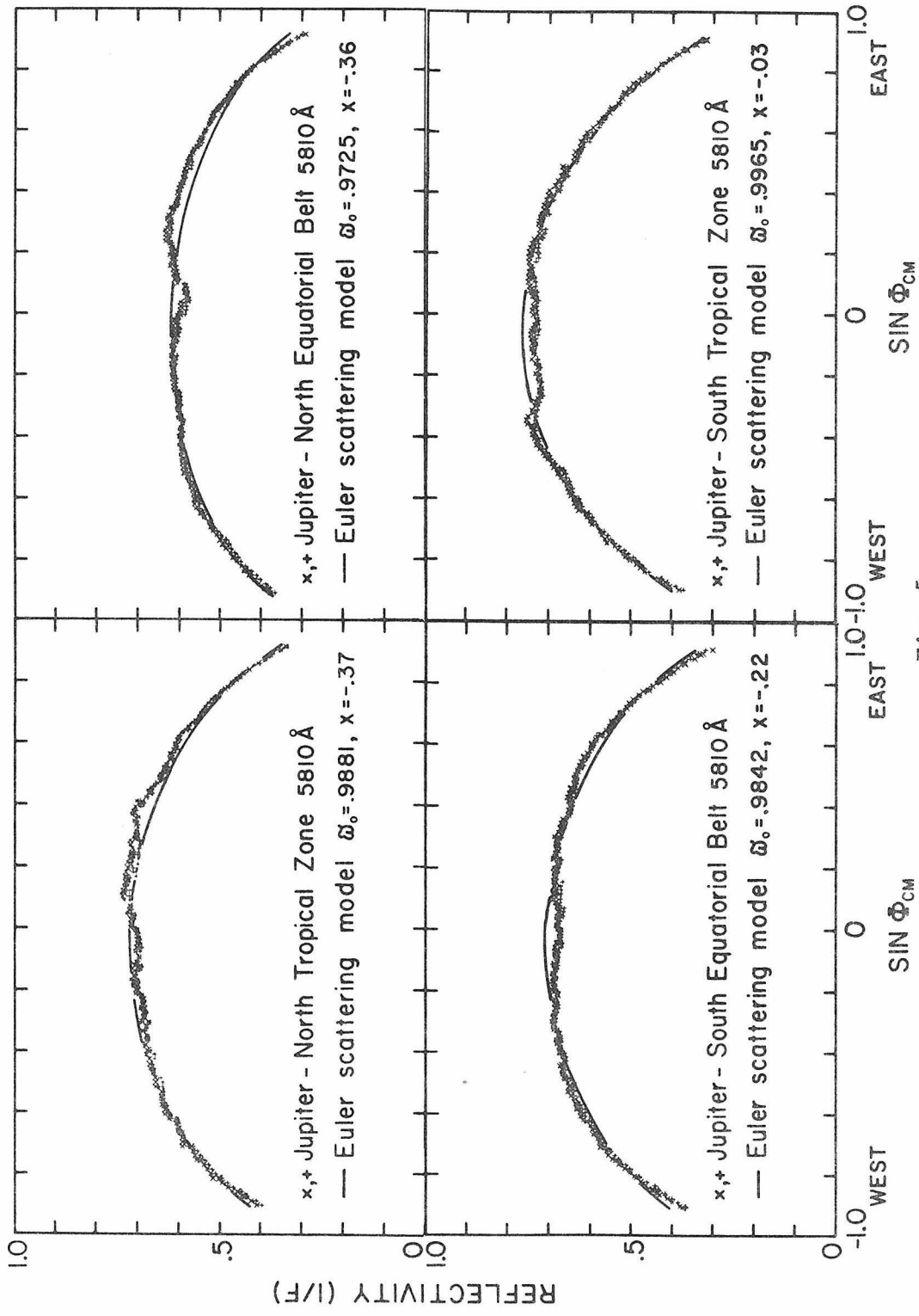
REFLECTIVITY (I/F)
1.0
.5
0
x,+ Jupiter - North Tropical Zone 5810 Å
— Euler scattering model ϖ₀=.9881, x=-.37
x,+ Jupiter - North Equatorial Belt 5810 Å
— Euler scattering model ϖ₀=.9725, x=-.36
x,+ Jupiter - South Equatorial Belt 5810 Å
— Euler scattering model ϖ₀=.9842, x=-.22
x,+ Jupiter - South Tropical Zone 5810 Å
— Euler scattering model ϖ₀=.9965, x=-.03
-1.0 WEST
0
1.0 EAST
SIN Φ_CM

Fig. 5

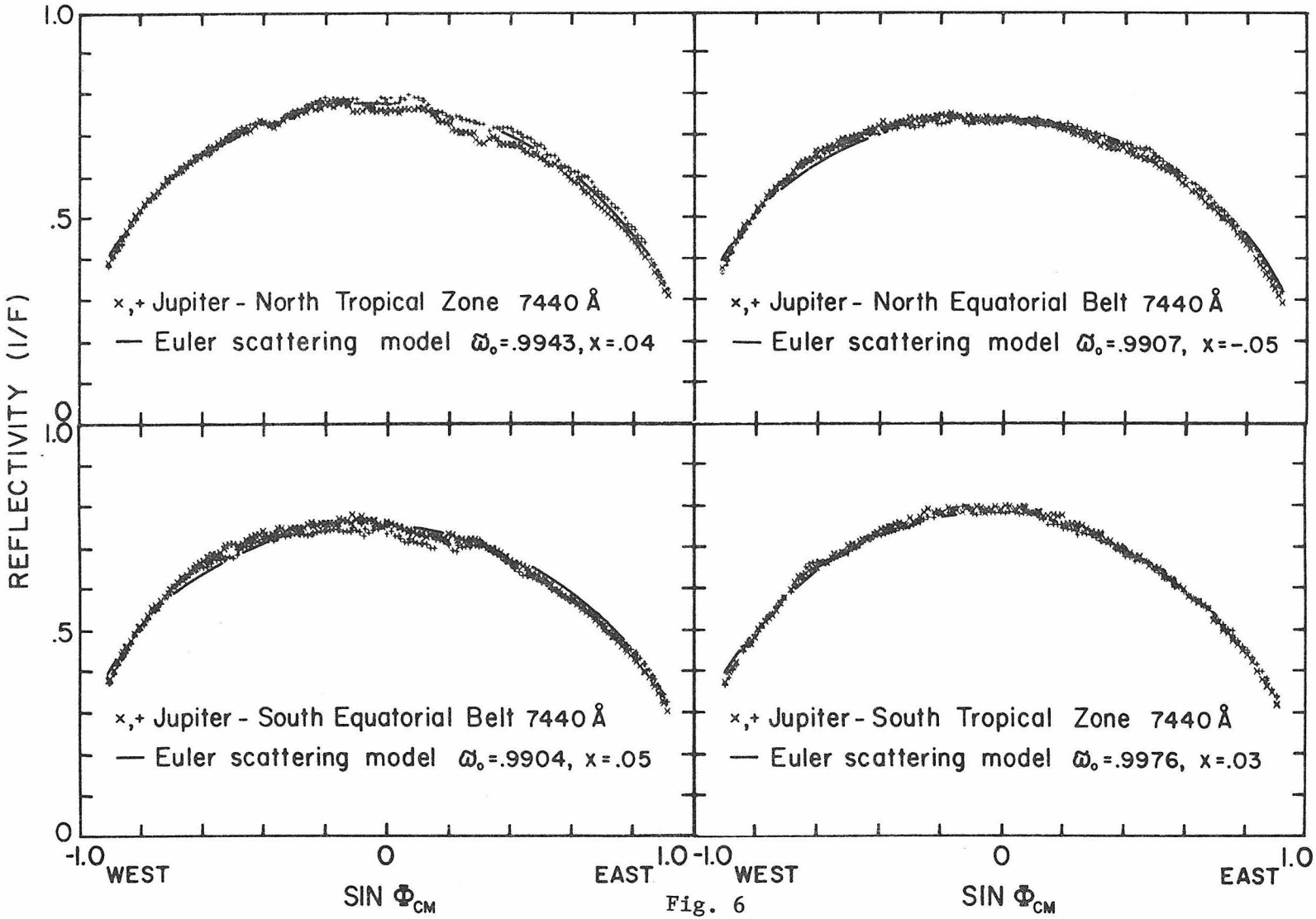
REFLECTIVITY (I/F)
1.0
.5
0
×,+ Jupiter - North Tropical Zone 7440 Å
— Euler scattering model ϖ₀=.9943, x=.04
×,+ Jupiter - North Equatorial Belt 7440 Å
— Euler scattering model ϖ₀=.9907, x=-.05
×,+ Jupiter - South Equatorial Belt 7440 Å
— Euler scattering model ϖ₀=.9904, x=.05
×,+ Jupiter - South Tropical Zone 7440 Å
— Euler scattering model ϖ₀=.9976, x=.03
-1.0
WEST
0
EAST
1.0
SIN Φ_CM

Fig. 6

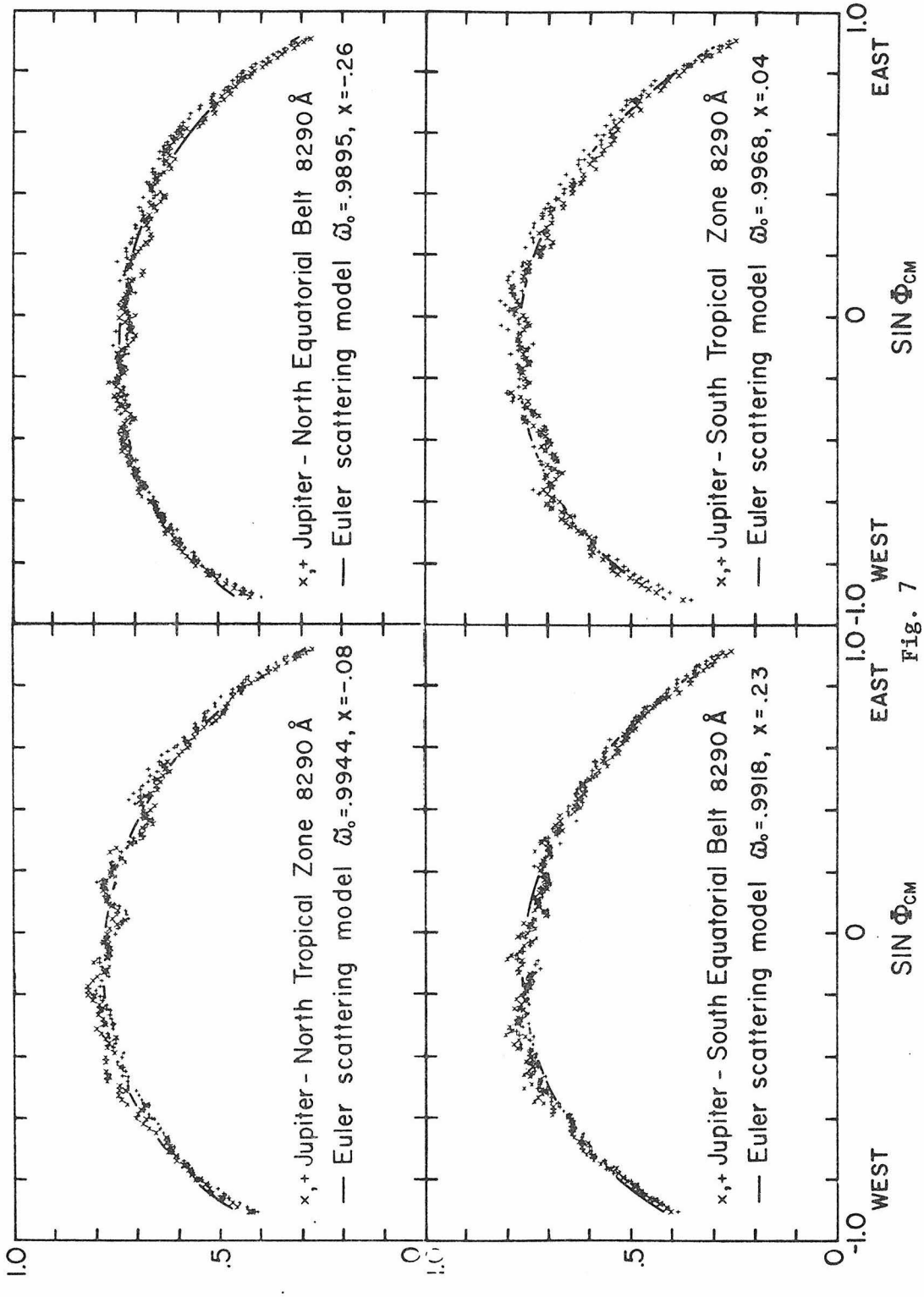
x,+ Jupiter - North Equatorial Belt 8290 Å
— Euler scattering model ω₀=.9895, x=-.26
x,+ Jupiter - North Tropical Zone 8290 Å
— Euler scattering model ω₀=.9944, x=-.08
x,+ Jupiter - South Tropical Zone 8290 Å
— Euler scattering model ω₀=.9968, x=.04
x,+ Jupiter - South Equatorial Belt 8290 Å
— Euler scattering model ω₀=.9918, x=.23
1.0
.5
0
WEST
EAST
-1.0
0
1.0
SIN Φ_CM

Fig. 7

an attempt to assess the effects of atmospheric seeing. It was found that the smeared limb-darkening function agrees with the unconvolved theoretical curve to better than 1% (well within the uncertainties in the data) out to $\left|\sin\Phi_{CM}\right| = 0.93$. The more conservative value of $\left|\sin\Phi_{CM}\right| = 0.92$ was chosen as the actual cutoff for the specific reasons that: 1) the "tails" of typical point-spread functions due to seeing are somewhat more extended than gaussians; 2) at the tropical latitudes the width of the seeing function represents a slightly larger fraction of the zonal chord length; and 3) the actual limb-darkening is probably not due to isotropic scattering and thus may have a more complicated shape close to the limbs which would convolve differently with the gaussians. In the interest of approaching as close to the limb as possible (since much of the information on scattering is contained in observations at oblique viewing geometries), while not compromising the results, the value of $\left|\sin\Phi_{CM,\,max}\right| = 0.92$, corresponding to a μ of 0.4 on the equator, appears reasonable.

In order to put the large quantities of data in a form which would expedite comparison of the results with other measurements or theoretical models, a simple parameterization of the limb structure curves has been sought. For this purpose a two-parameter model in which the atmosphere is assumed to be locally plane-parallel, semi-infinite, homogeneous and composed of particles which individually scatter according to the Euler phase function $p(\cos\theta) = \tilde{\omega}_o(1 + x\cos\theta)$ has been chosen. θ is defined as the angle between the initial and scattered directions

of a photon, and the parameters $\tilde{\omega}_o$ and x are, respectively, the albedo for single scattering and an asymmetry parameter which varies between +1 for predominantly forward scattering and -1 for predominantly backward scattering. The parameter x is related to the standard phase function asymmetry parameter g such that g = x/3, where by definition,

$$g = \langle \cos\theta \rangle = \frac{1}{2\tilde{\omega}_o} \int_{-1}^{1} \cos\theta \; p(\cos\theta) \; d(\cos\theta) \quad . \qquad (6)$$

The foregoing set of conditions will hereafter be referred to as the Euler scattering model. It is to be emphasized that these calculations are not necessarily intended to represent explicit physical models, but are designed primarily to provide a convenient parameterization of the data, and secondarily to provide a semi-quantitative evaluation of regional and spectral variations in the scattering properties of the jovian atmosphere.

As shown by Chandrasekhar (1960), the solution to the multiple scattering problem in the context of the Euler scattering model yields the following expression for surface brightness, or reflectivity:

$$I(\mu,\mu_o,\varphi - \varphi_o)/F = \frac{1}{4}\tilde{\omega}_o \frac{\mu_o}{\mu + \mu_o} \psi(\mu)\,\psi(\mu_o) - x\phi(\mu)\phi(\mu_o) + x(1 - \mu^2)^{1/2} \cdot$$

$$\cdot \; H^{(1)}(\mu)(1 - \mu_o^2)^{1/2} \; H^{(1)}(\mu_o) \cos(\varphi - \varphi_o) \qquad (7)$$

where

$$\psi(\mu) = H(\mu)\;(1 - c\mu)$$

$$\phi(\mu) = q\mu H(\mu)$$

and H and $H^{(1)}$ are Chandrasekhar H-functions which satisfy the following integral relationships:

$$H(\mu) = 1 + \mu H(\mu) \int_0^1 \frac{\frac{1}{2}\tilde{\omega}_o[1 + x(1 - \tilde{\omega}_o)\mu'^2]}{\mu + \mu'} H(\mu')d\mu' \qquad (8)$$

$$H^{(1)}(\mu) = 1 + \mu H^{(1)}(\mu) \int_0^1 \frac{\frac{1}{4}x\tilde{\omega}_o(1 - \mu'^2)}{\mu + \mu'} H^{(1)}(\mu')\, d\mu' \qquad (9)$$

and the constants c and q are given by

$$c = \frac{x\tilde{\omega}_o(1 - \tilde{\omega}_o)\,\alpha_1}{2 - \tilde{\omega}_o\,\alpha_o} \quad ; \quad q = \frac{2(1 - \tilde{\omega}_o)}{2 - \tilde{\omega}_o\,\alpha_o} \qquad (10)$$

where α_o and α_1 are the zeroth and first moments of H. The nth moment of an H- function is defined as

$$\alpha_n = \int_0^1 \mu^n H(\mu)d\mu \quad . \qquad (11)$$

A computer program was written which calculates ψ, ϕ, $H^{(1)}$, and the required moments. The functions are calculated for values of μ ranging from 0 to 1 in steps of 0.01, for any combination of $\tilde{\omega}_o$ and x. The heart of the program is the solution for H and $H^{(1)}$, which is obtained iteratively by making use of equations (8) and (9) above and beginning with the initial guess $H(\mu) = H^{(1)}(\mu) = 1$. All integrations are performed using 8-point gaussian quadrature in μ. Once

equations (8) and (9) have converged, it is possible to calculate H and $H^{(1)}$ for arbitrary values of μ. The convergence is extremely rapid. As a check, the computations and published results for ψ, ϕ, and $H^{(1)}$ (Chandrasekhar, 1960) were compared for various values of $\tilde{\omega}_o$ with x = 0 and x = 1. The agreement is to better than 1 part in 10^4.

Due to the highly nonlinear nature of the radiative transfer equations, best-fitting models were arrived at by the method of "brute force" least-squares. Model I/F values assuming various combinations of $\tilde{\omega}_o$ and x are calculated at the observed values of μ, μ_o, and $\cos(\varphi - \varphi_o)$ and the sum of the squares of the residuals between the data and each model are computed. A two-dimensional paraboloid is then fit to the $(\tilde{\omega}_o, x)$ pairs which yield the lowest residuals; the location of the minimum determines the best-fitting values of $\tilde{\omega}_o$ and x. The root-mean-square (RMS) residuals are generally one to two times larger than the estimated RMS uncertainty in the individual data points. In some instances, particularly at the short wavelengths in the NEB, the RMS residuals were three times as large as the 1σ uncertainty in the data. It is possible that this is indicative of a real failure of the model, either in its assumption of vertical homogeneity, or in the simple form of the particle phase function, or both. However, the estimate of the 1σ noise level does not include the contribution of intermediate spatial frequency noise due to lateral inhomogeneities (local bright or dark spots) in the limb structure curves. It is difficult to make estimates of the magnitude of the contribution of such features to

the formal error. Independent reductions of data from images taken several hours apart, such that a different spatial distribution of local inhomogeneities was observed, yield very similar model results. It may be concluded that individual limb structure profiles are fairly well represented by the two-parameter characterization. The best-fit models for the four chosen latitude bands are shown superimposed upon the data in Figures 2-7.

The results of fitting the Euler scattering model to the data at all wavelengths are summarized in Figures 8 and 9. The error bars on $\tilde{\omega}_o$ and x represent the 2σ levels (85% confidence for the two-parameter case). These include the formal errors in the model parameters due to random noise in the data as well as errors arising from systematic biasing of the limb-darkening curves due to uncertainty in the absolute photometric calibration. At 4865Å, the residuals steadily decreased as x was permitted to become more negative. Within the limits of the Euler scattering model, the best-fit solution was determined for all latitudes by letting x = -1, and solving for the best value of $\tilde{\omega}_o$. Consequently, no error bars are shown on x at this wavelength. This result has been verified from two sets of images obtained 2 hours apart, and is therefore not a peculiarity of the particular spatial distribution of longitudinal inhomogeneities in the belts and zones at a given rotational phase.

Figure 8. - Values of single scattering albedo, $\tilde{\omega}_o$, for the Euler scattering model vs. wavelength for the NTrZ, NEB, SEB and $STrZ_s$. The error bars represent the $\pm 2\sigma$ or 85% confidence level.

Figure 9. - Values of the Euler scattering model asymmetry parameter, x, vs. wavelength for the same four regions as in Figure 8. The error bars represent the $\pm 2\sigma$ or 85% confidence level.

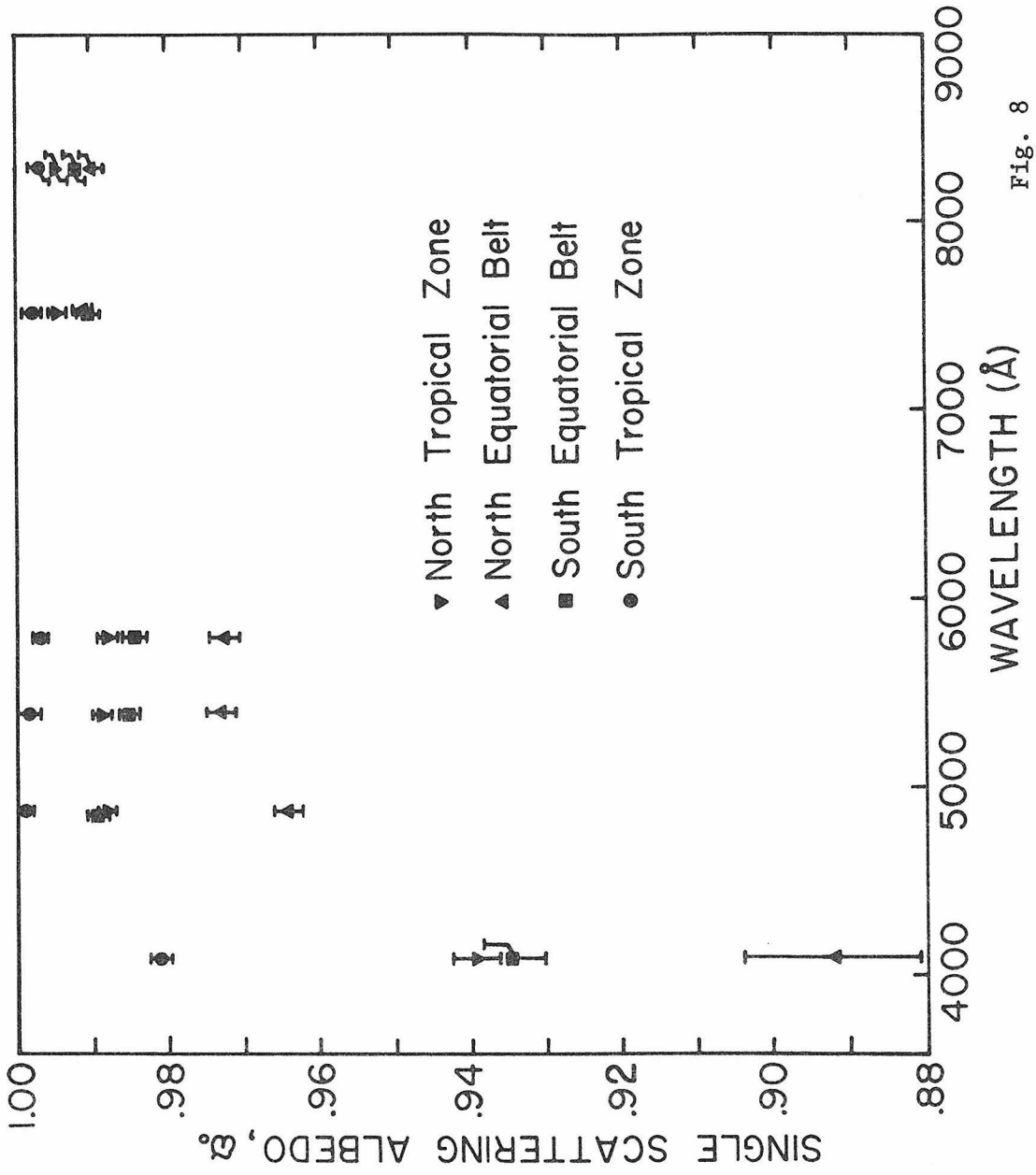
SINGLE SCATTERING ALBEDO, ω
1.00
.98
.96
.94
.92
.90
.88
4000
5000
6000
7000
8000
9000
WAVELENGTH (Å)
North Tropical Zone
North Equatorial Belt
South Equatorial Belt
South Tropical Zone

Fig. 8

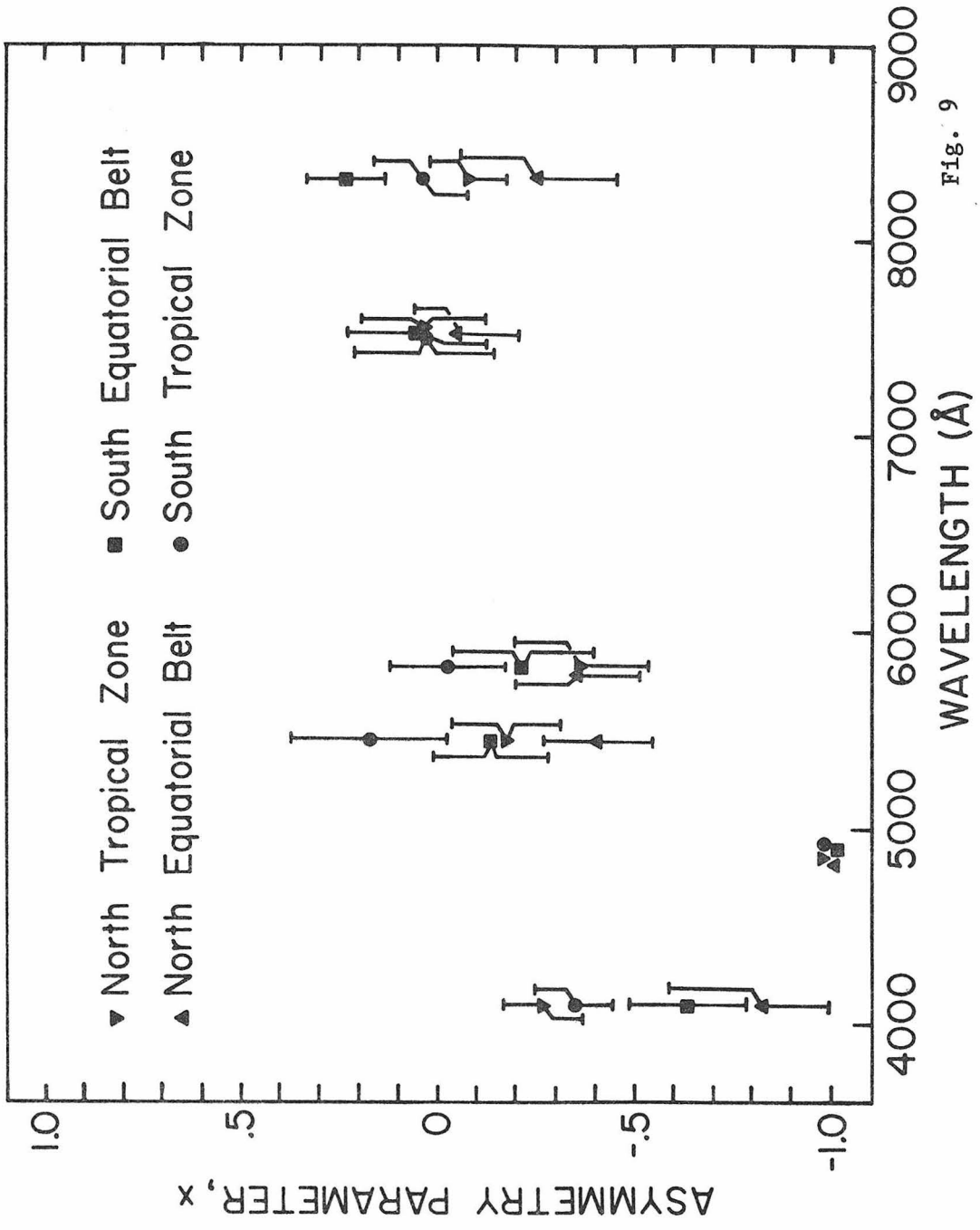
North Tropical Zone
South Equatorial Belt
North Equatorial Belt
South Tropical Zone
ASYMMETRY PARAMETER, x
1.0
.5
0
-.5
-1.0
4000
5000
6000
7000
8000
9000
WAVELENGTH (Å)

Fig. 9

The Euler model solutions have been used to calculate full phase limb-darkening curves for the four latitude bins considered. These curves, normalized to the reflectivity at the point where $\mu = \mu_o = 1$, are shown in Figure 10. The profiles may be put on an absolute scale by referring to Table II, which gives absolute spectral reflectivity for the point of normalization.

Figure 10. - Normalized full phase limb-darkening curves determined by fitting the vidicon data with the Euler scattering model in each of the continuum wavelength channels for the NTrZ, NEB, SEB and $STrZ_s$. The error bars, for simplicity shown only on the curves labeled "a," represent an estimate of the $\pm 3\sigma$ formal uncertainty in the shape of the limb-darkening profiles. This estimate is applicable to each of the curves displayed.

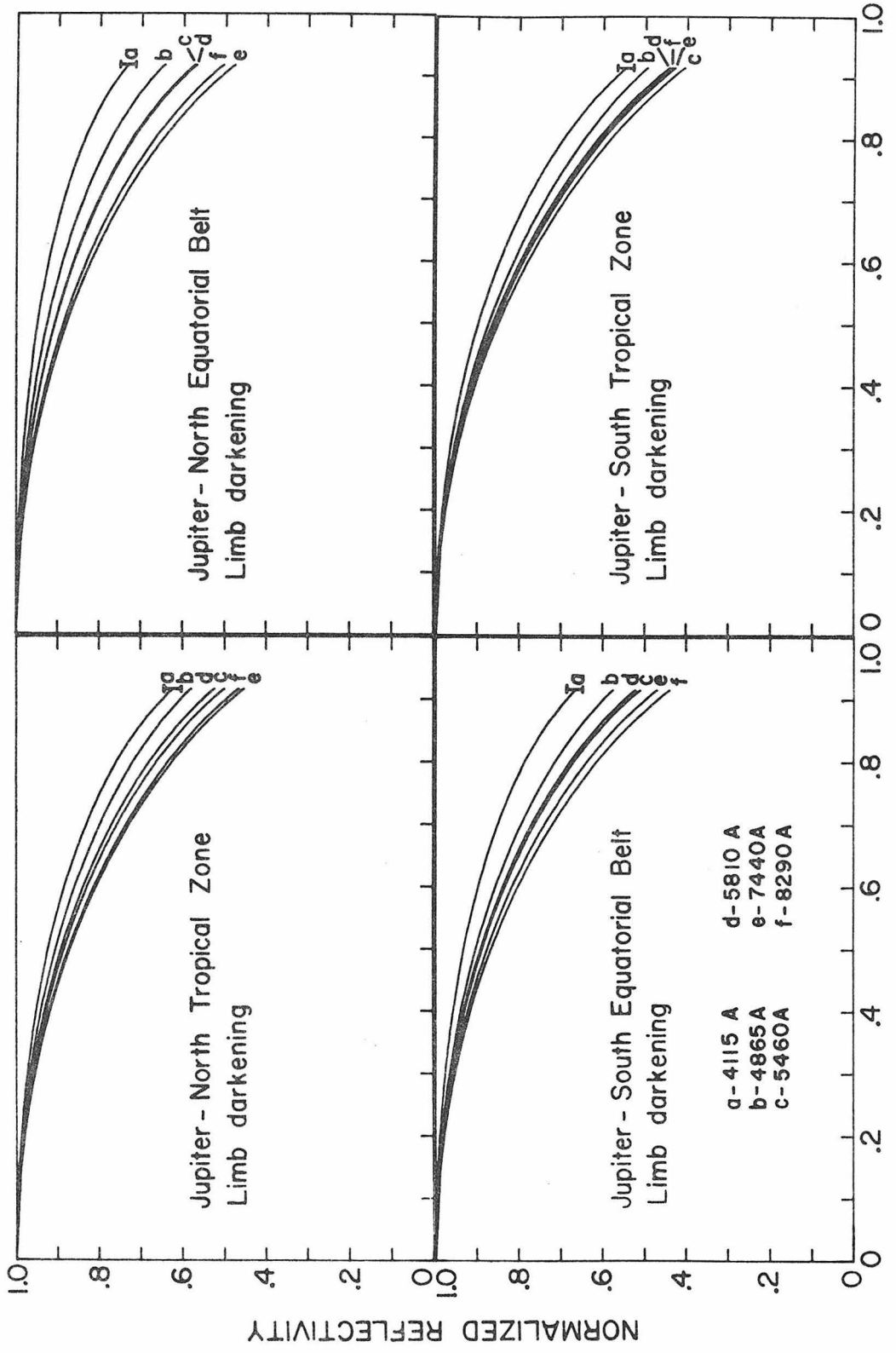
Jupiter - North Equatorial Belt
Limb darkening
Jupiter - North Tropical Zone
Limb darkening
Jupiter - South Tropical Zone
Limb darkening
Jupiter - South Equatorial Belt
Limb darkening
a - 4115 A
b - 4865 A
c - 5460A
d - 5810 A
e - 7440A
f - 8290 A
NORMALIZED REFLECTIVITY
NORMALIZED RADIUS
0
.2
.4
.6
.8
1.0

Fig. 10

TABLE II

Reflectivities at full phase for the point where $\mu = \mu_o = 1$ calculated from the best-fit Euler scattering models. The uncertainty is $\sim \pm 5\%$.

	NTrZ	NEB	SEB	$STrZ_s$
4115Å	0.50	0.44	0.51	0.69
4865Å	0.78	0.63	0.79	0.99
5460Å	0.75	0.64	0.71	0.93
5810Å	0.75	0.64	0.71	0.87
7440Å	0,81	0.77	0.75	0.91
8290Å	0.82	0.77	0.77	0.88

Chapter 5

COMPARISON WITH EARLIER MEASUREMENTS

To observations which ourselves we make
We grow more partial for th' observer's sake.

- Alexander Pope
Moral Essays

The largest source of error in the data is the uncertainty in the absolute photometric calibration. The most recently published comprehensive study of spatially resolved reflectivities of Jupiter is the work of Orton (1975a). His observations are very extensive and cover many rotational aspects of the planet, so the random effects of lateral inhomogeneities have been averaged to some extent. Since the vidicon images are essentially "snapshots," they do not provide this "advantage." Therefore, one may expect to obtain the optimum estimate of reflectivity at a given location and viewing geometry (e.g., on the central meridian) using the least-squares best-fit models described in the previous chapter. This provides a direct comparison of the SIVIT photometry and Orton's data. It should be remembered that Jupiter's cloud bands have changed in morphology in the time since Orton's observations were made (1973-74). In addition, the latitudes of specific features, in particular the South Tropical Zone, have changed; in fact, in 1975 the STrZ split into two components separated by a band of belt-like material. Reference to Figure 1 of Orton (1975a) shows that in 1973-74 the STrZ was much more homogeneous and nearer the equator. Since this accounts for a non-negligible difference in

viewing geometry, the model calculations have been used to extrapolate to the geometry as it was observed by Orton. Figure 11 compares I/F values for the NTrZ, NEB, SEB, and STrZ from the smoothed fits to the vidicon data with Orton's central meridian results. The agreement is quite good, and in most cases is well within experimental errors. Slight differences may be accounted for by real changes in the properties of the jovian atmosphere.

With respect to the shape of the limb structure curves, there are significant differences with the results of earlier investigations. Reference to Figure 9 shows that in the majority of cases, the asymmetry parameter x takes on negative values or values close to zero. The largest value of x that was found in this work is in the case of the SEB at 8290Å, where the value $x = 0.23 \pm 0.12$ was obtained. These results are in disagreement with other work.

One of the earliest published attempts to fit the Euler phase function to jovian limb-darkening was the work of Harris (1961). Using full disk photometry by Hardie (1954) and limb-darkening measurements taken from photographs (Barabashev and Semejkin, 1933), Harris arrived at the phase function $p(\cos\theta) = 0.98 \cdot (1 + 0.6 \cos\theta)$ for the visible region. However, the 21 year interval that separates the limb-darkening measurements and absolute photometry, the low spatial resolution, and possible errors arising from the use of photographs are matters of some concern. It is therefore possible that Harris' results

Figure 11. - Comparison of Orton's (1975a) photometry in the NTrZ, NEB, SEB and STrZ with the SIVIT results. The error bars are ± 1σ. The best-fit Euler scattering model solutions have been used to correct for the small but significant differences in viewing geometry between Orton's observations and those reported here.

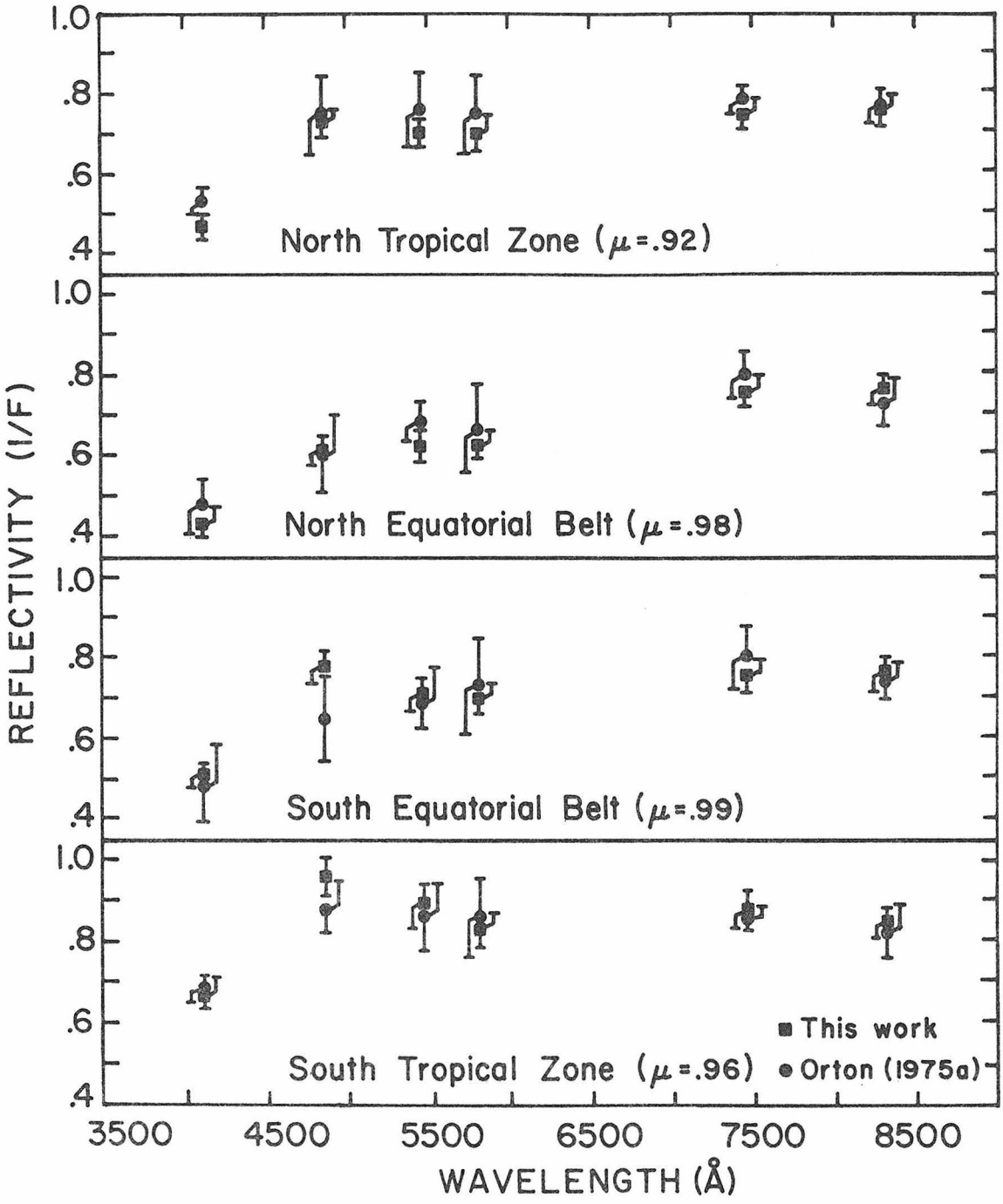
1.0
.8
.6
.4
North Tropical Zone (μ=.92)
North Equatorial Belt (μ=.98)
South Equatorial Belt (μ=.99)
South Tropical Zone (μ=.96)
REFLECTIVITY (I/F)
■ This work
● Orton (1975a)
3500
4500
5500
6500
7500
8500
WAVELENGTH (Å)

Fig. 11

are inaccurate, but it must be recognized that over the past several decades Jupiter's atmosphere may have experienced real changes in its scattering properties.

A more recent spectrophotometric study of the scattering in spatially resolved regions on the disk of Jupiter was undertaken by Binder and McCarthy (1973). These observations consisted of measurements of absolute reflectivity at various locations in certain belts and zones, using a single aperture detector with an effective spatial resolution of 3-4 arcsec. In reducing their data to an Euler scattering model parameterization, Binder and McCarthy used a two-step procedure in which they first fit the data to the empirical Minnaert reflection law

$$I/F = (I/F)_o \mu_o^k \mu^{k-1} \quad . \tag{12}$$

They then determined the Euler model parameters $\tilde{\omega}_o$ and x which were consistent with the previously calculated values of $(I/F)_o$ and k. They arrived at the solution $p(\cos\theta) = 0.989 \cdot (1 + 0.54 \cos\theta)$ at 5940Å and $p(\cos\theta) = 0.987 \cdot (1 + 0.55 \cos\theta)$ at 8230Å for the STrZ, which may be directly compared with the SIVIT results which yield $p(\cos\theta) = 0.997 \cdot (1 - 0.03 \cos\theta)$ at 5810Å and $p(\cos\theta) = 0.997 \cdot (1 + 0.04 \cos\theta)$ at 8290Å. At other visible and near-IR wavelengths, Binder and McCarthy found x to vary from a minimum of 0.42 to as high as 0.80 in the STrZ. As a test of the validity of their two-step reduction technique, a direct fit of the Euler scattering model to

Binder and McCarthy's published 8230Å STrZ data has been made using the "brute force" least-squares technique. The solution $p(\cos\theta) = 0.970 \cdot (1 + 0.28 \cos\theta)$ was returned by this method, a result which is inconsistent with Binder and McCarthy's solution from the same data. The computer program has been tested and checked repeatedly and appears to work properly. Thus, the reason for the discrepancy is not obvious, but one possibility is that Binder and McCarthy's two-step procedure, which initially makes use of the simple Minnaert law, may result in some loss of curvature information contained in the actual data. Other discrepancies arise from the fact that Binder and McCarthy's I/F values are some 15-25% lower than those presented here and Orton's (1975a). This is consistent with their solution of high positive values of the asymmetry parameter x, since these values imply low backscattering of sunlight toward the Earth near full phase.

One final test of the SIVIT data has been made in order to put to rest any lingering qualms that the vidicon data contain some systematic error. This test involves the corrections which have been applied to compensate for nonlinearity and reciprocity failure in the vidicon tube. The experimentally determined values for γ_1 and γ_2 (see Chapter 3) are at variance with the results obtained for other vidicons in which gammas very much closer to unity were measured (Westphal, 1973). The following analysis supposes that the experimentally determined gammas are incorrect and that the SIVIT is in fact linear with $\gamma_1 = \gamma_2 = 1$. Standard star reductions and limb-darkening

model fits were repeated for the 5810Å channel under this assumption, and Table III presents a comparison of reflectivities and model parameters for the "linear" case and the "measured" case. The absolute reflectivities assuming $\gamma_1 = \gamma_2 = 1$ are not significantly different from the values determined when the experimentally determined corrections were applied. Furthermore, the values of the asymmetry parameter x are not appreciably altered, and thus this potential source of doubt can be reasonably eliminated. In summary, then, either Binder and McCarthy's photometry is in error, the SIVIT calibrations (and Orton's) are somehow faulty, or Jupiter has brightened by a considerable amount since 1971-72.

Pilcher and Kunkle (1976) have constructed limb-darkening profiles of several regions on Jupiter using overlapping area scans with about 1 arcsec spatial resolution. Their continuum channels at 6300Å and 8200Å are sufficiently close to the 5810Å and 8290Å filters used in this study so as to permit first-order comparisons of the data. Pilcher and Kunkle assumed an isotropically scattering model (a special case of the Euler model in which x = 0) and determined the range of $\tilde{\omega}_o$ values which gave the closest fit to the measurements. Calculations with the vidicon data in which x was assumed to be zero returned values of $\tilde{\omega}_o$ which agreed in most cases with Pilcher and Kunkle's solutions to within two or three units in the third decimal place.

TABLE III

Comparison of SIVIT data reduction assuming the measured values

$\gamma_1 = 0.959$, $\gamma_2 = 0.977$ with the "linear" case $\gamma_1 = \gamma_2 = 1$ at 5810Å.

	$\gamma_1 = 0.959$, $\gamma_2 = 0.977$			$\gamma_1 = \gamma_2 = 1$		
	$(I/F)_{CM}$	$\tilde{\omega}_o$	x	$(I/F)_{CM}$	$\tilde{\omega}_o$	x
NTrZ	0.71 ± 0.04	0.988 ± 0.002	-0.37 ± 0.17	0.69 ± 0.04	0.984 ± 0.001	-0.33 ± 0.11
NEB	0.61 ± 0.04	0.973 ± 0.002	-0.36 ± 0.16	0.59 ± 0.04	0.968 ± 0.002	-0.33 ± 0.12
SEB	0.68 ± 0.04	0.984 ± 0.002	-0.22 ± 0.18	0.65 ± 0.04	0.980 ± 0.002	-0.22 ± 0.12
$STrZ_s$	0.74 ± 0.04	0.997 ± 0.001	-0.03 ± 0.15	0.71 ± 0.04	0.992 ± 0.001	-0.20 ± 0.10

Tomasko et al. (1976) present the results of high spatial resolution imaging by the imaging photopolarimeter (IPP) experiment aboard the Pioneer 10 spacecraft which encountered Jupiter in December of 1973. At the heart of the IPP experiment were two channeltron detectors with spectral response limited to a blue (3900-5000Å) channel and a red (5950-7200Å) channel. The effective wavelengths of these channels are about 4400 and 6400Å, respectively. Images were obtained at a variety of phase angles from 12° to 150°. Tomasko et al. have reduced the IPP data in the blue and red channels for two regions on Jupiter, the South Equatorial Belt and South Tropical Zone. Since the SIVIT data were obtained near full phase, the most direct comparison between the vidicon data and the IPP results can be made using the spacecraft data at 12° phase angle. This requires an extrapolation of the vidicon data to this phase angle using the best-fit Euler scattering models. Tomasko et al. present data numbers for points along the SEB and STrZ for which they give the appropriate values of μ, μ_o, and $\cos(\varphi - \varphi_o)$. There is no simple relation between these geometric variables as in the case of a planet observed in the same plane as the planetary equator and the illuminating source, due to the inclination of the spacecraft trajectory and spin-scan mode of data acquisition. Thus, the simplest method of comparing the vidicon and spacecraft data is to calculate the Euler model reflectivities at the values of μ, μ_o, and $\cos(\varphi - \varphi_o)$ given by Tomasko et al. The limb-darkening curves for the relevant geometries were computed at

4115 and 4865Å, which essentially bracket the Pioneer blue channel, and at 5810 and 7440Å, which bracket the red channel. The results are plotted against μ_o and shown in Figures 12a,b and 13a,b for the SEB and STrZ, respectively. The IPP and extrapolated ground-based results are normalized to the reflectivity at the largest value of μ_o. Except for the SEB data in the blue, the Pioneer limb-darkening curves are steeper than the extrapolated ground-based profiles. There are several possible explanations for these differences. First, if the atmospheric scatterers exhibit a sharp backscattering feature confined to the largest scattering angles, the character of the limb-darkening curves which were fitted to the low phase angle data would be different from those obtained at larger angles. This scenario is unlikely, since the combination of different species of scatterers and the expected dispersion in particle sizes and shapes would smooth out any such sharp features. Second, significant changes may have occurred in the jovian atmosphere in the two year interval between Pioneer 10 encounter and the acquisition of the vidicon data. Perhaps a third hypothesis is the most satisfactory, in which it is realized that the ground-based data were acquired at geometries such that $\cos(\varphi - \varphi_o) \sim -1$ for points in the latitude bins, whereas the inclination of the Pioneer 10 trajectory insured that $\cos(\varphi - \varphi_o)$ adopted values closer to -0.95 to -0.97. Therefore, the differences between the spacecraft and ground-based data may be indicative of a stronger dependence on $\cos(\varphi - \varphi_o)$ than allowed by the Euler scattering model.

Figure 12a. - Comparison of relative photometry from the Pioneer 10 imaging photopolarimeter "blue" channel (Tomasko et al., 1976) in the South Equatorial Belt with the vidicon results at 4115 and 4865Å. The data are plotted against μ_o and the reflectivities are normalized to the I/F value at the largest value of μ_o observed by the spacecraft. The spacecraft measurements were obtained at a phase angle of 12° and the vidicon data have been extrapolated to this viewing geometry using the Euler best-fit models in the appropriate wavelength channels.

Figure 12b. - Comparison of relative photometry from the Pioneer 10 IPP "red" channel in the SEB with the vidicon results at 5810 and 7440Å. The normalization and extrapolation of the data are as in Figure 12a and as discussed in the text.

Figure 13a. - Similar to Figure 12a except for the South Tropical Zone.

Figure 13b. - Similar to Figure 12b except for the STrZ.

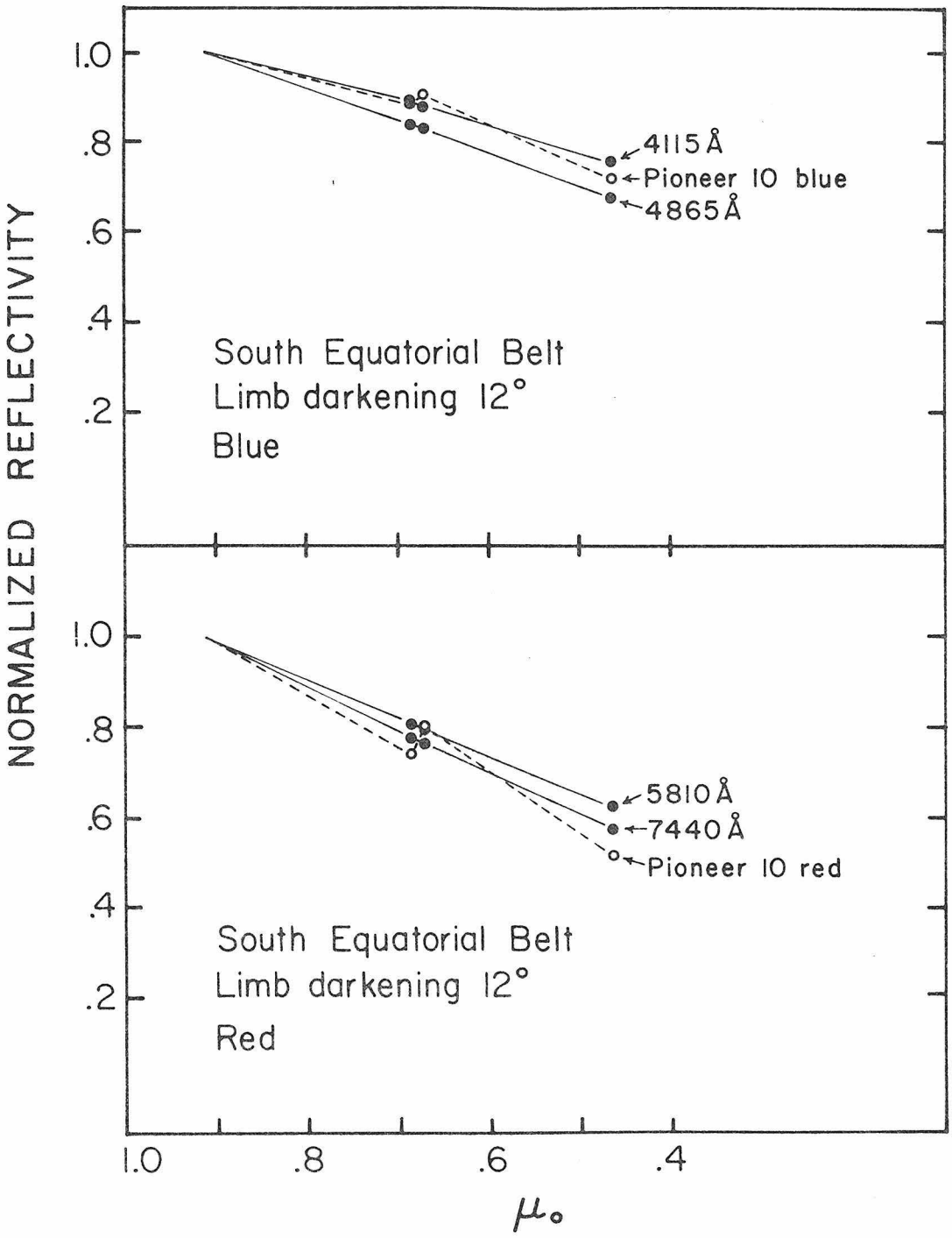
NORMALIZED REFLECTIVITY
1.0
.8
.6
.4
.2
4115 Å
Pioneer 10 blue
4865 Å
South Equatorial Belt
Limb darkening 12°
Blue
5810 Å
7440 Å
Pioneer 10 red
South Equatorial Belt
Limb darkening 12°
Red
1.0
.8
.6
.4
μ₀

Figs. 12a, 12b

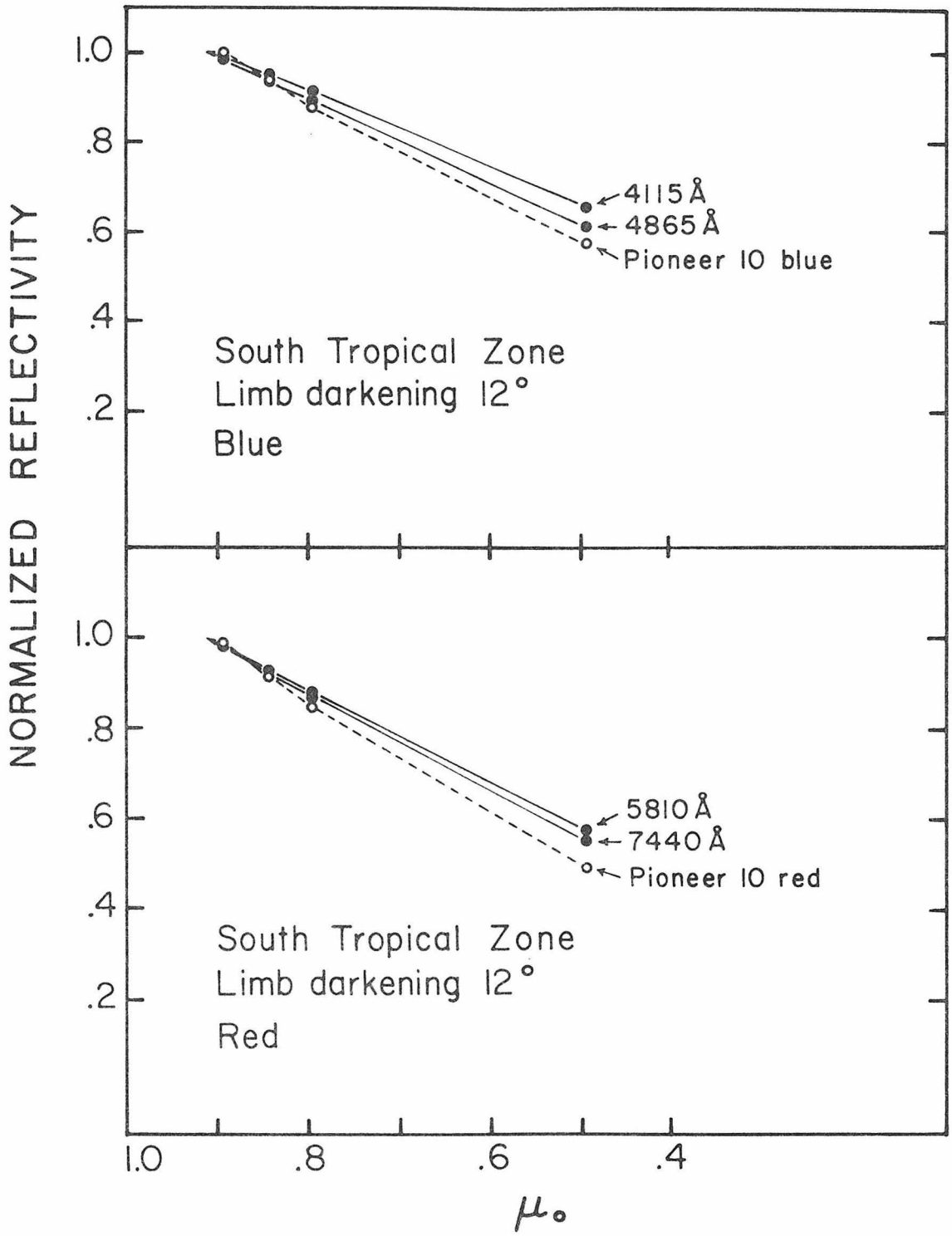
NORMALIZED REFLECTIVITY
1.0
.8
.6
.4
.2
4115 Å
4865 Å
Pioneer 10 blue
South Tropical Zone
Limb darkening 12°
Blue
5810 Å
7440 Å
Pioneer 10 red
South Tropical Zone
Limb darkening 12°
Red
1.0
.8
.6
.4
μ₀

Figs. 13a, 13b

Despite the quantitative differences in the ground-based and spacecraft data, there are several important similarities. First, the IPP and vidicon data show that the limb-darkening in the SEB is shallower than in the STrZ, and that this difference is more pronounced in the blue than in the red. Second, both sets of measurements indicate that for both the SEB and STrZ the limb-darkening in the blue is less steep than the limb-darkening in the red. These similarities between the two sets of data indicate that the observed spectral and regional contrasts represent genuine properties of the jovian atmosphere, in spite of the two-year hiatus separating the Pioneer 10 encounter and collection of the ground-based measurements, and in addition, in spite of the very different methods of data acquisition.

Chapter 6

DISCUSSION

> Every cloud has a silver lining -
> but that is small consolation when
> you cannot see through the cloud.
>
> - W. Burton Baldry
> Stray Thoughts

The implications of the model results regarding the scattering properties of the jovian atmosphere shall now be discussed. Considering first the single scattering albedo, $\tilde{\omega}_o$ (Figure 8), it appears that the NTrZ and SEB are similar at all wavelengths, whereas a marked difference is demonstrated between the NEB (the darkest belt) and the $STrZ_s$ (the brightest zone). The decrease in single scattering albedo toward shorter wavelengths is much more severe in the NEB than in the NTrZ and SEB, and this dropoff is least pronounced in the $STrZ_s$.

With regard to the asymmetry parameter, x (Figure 9), the data suggest a trend toward more negative values at the shorter wavelengths. Since the data were collected when Jupiter was at nearly full phase, the observations are most sensitive to the backscattering lobe of the single scattering phase function and the derived values of x may not be representative of the predominant asymmetry in the actual phase functions. Therefore, it is possible that the actual phase functions are mainly forward scattering. However, the following discussion shows that the observed negative values of x imply that the effective atmospheric single scattering phase function must have a somewhat

enhanced backscattering lobe (i.e., the first derivative of the scattering phase function is ≥ 0 at high scattering angles). This correlation can be demonstrated by fitting the Euler scattering model to full phase limb-darkening curves for a number of simulated model atmospheres. Various models, which differ in the magnitudes and relative proportions of forward and backward scattering, will be considered. It will be shown that the effective Euler asymmetry parameter, x, is positive if the atmospheric single scattering phase function is primarily forward scattering without an enhanced back-scatter lobe, and that x decreases (and eventually becomes negative) as the backscatter intensity increases.

The single scattering phase functions used in this demonstration are the Rayleigh phase function

$$p(\cos\theta) = \frac{3}{4}\tilde{\omega}_o\,(1 + \cos^2\theta) \tag{13}$$

and the double Henyey-Greenstein phase function

$$p(\cos\theta) = \tilde{\omega}_o \left\{ \frac{f(1-g_1^2)}{(1+g_1^2 - 2g_1\cos\theta)^{3/2}} + \right.$$

$$\left. + \frac{(1-f)\,(1-g_2^2)}{(1+g_2^2 - 2g_2\cos\theta)^{3/2}} \right\} \tag{14}$$

in which g_1 and g_2 are asymmetry parameters ranging between -1 and +1. By choosing g_1 positive and g_2 negative, and appropriate values

for the parameter f, a number of differently shaped phase functions with varying proportions of forward to backward scattering can be obtained. Figure 14a shows three phase functions of this type; in each case, $\tilde{\omega}_o = 0.99$, $g_1 = 0.5$, $g_2 = -0.5$ and the first case has $f = 1.0$, the second $f = 0.9$ and the third $f = 0.8$. The Rayleigh phase function with $\tilde{\omega}_o = 1$ is also shown in Figure 14a. Model atmospheres composed of particles with these phase functions were assumed to be plane-parallel, semi-infinite, and homogeneous. Full phase limb-darkening data for the Rayleigh phase function were taken from Dlugach and Yanovitskij (1974) and for the double Henyey-Greenstein functions were calculated using a doubling program kindly provided by J. Hansen, and which is described in Hansen and Travis (1974). This program expands the single scattering phase function in a Legendre series. In its original form, the program calculated the Legendre coefficients from numerical integration of $p(\cos\theta)$. The program was modified to eliminate this numerical integration and replace it with a subroutine which employs the expansion formula

$$\frac{(1-g^2)}{(1+g^2 - 2g\cos\theta)^{3/2}} = \sum_{n=0}^{\infty} (2n+1)g^n P_n(\cos\theta) \qquad (15)$$

(MacRobert, 1967) so that for the double Henyey-Greenstein phase function the Legendre coefficients were calculated analytically by

$$a_n = (2n+1)\left[f\cdot g_1^n + (1-f)\cdot g_2^n\right] \qquad (16)$$

Figure 14a. The three double Henyey-Greenstein phase functions and the Rayleigh phase function used in simulations in which limb-darkening curves were computed and fitted using the Euler scattering model.

Figure 14b. Euler phase functions corresponding to the scattering models which gave the best fit to the limb-darkening for the phase functions in Figure 14a. The limb structure for the phase function labeled "a" in Figure 14a was fit by an Euler scattering model which corresponds to the phase function labeled "a" in this figure. A similar correspondence holds for "b," "c," and "d."

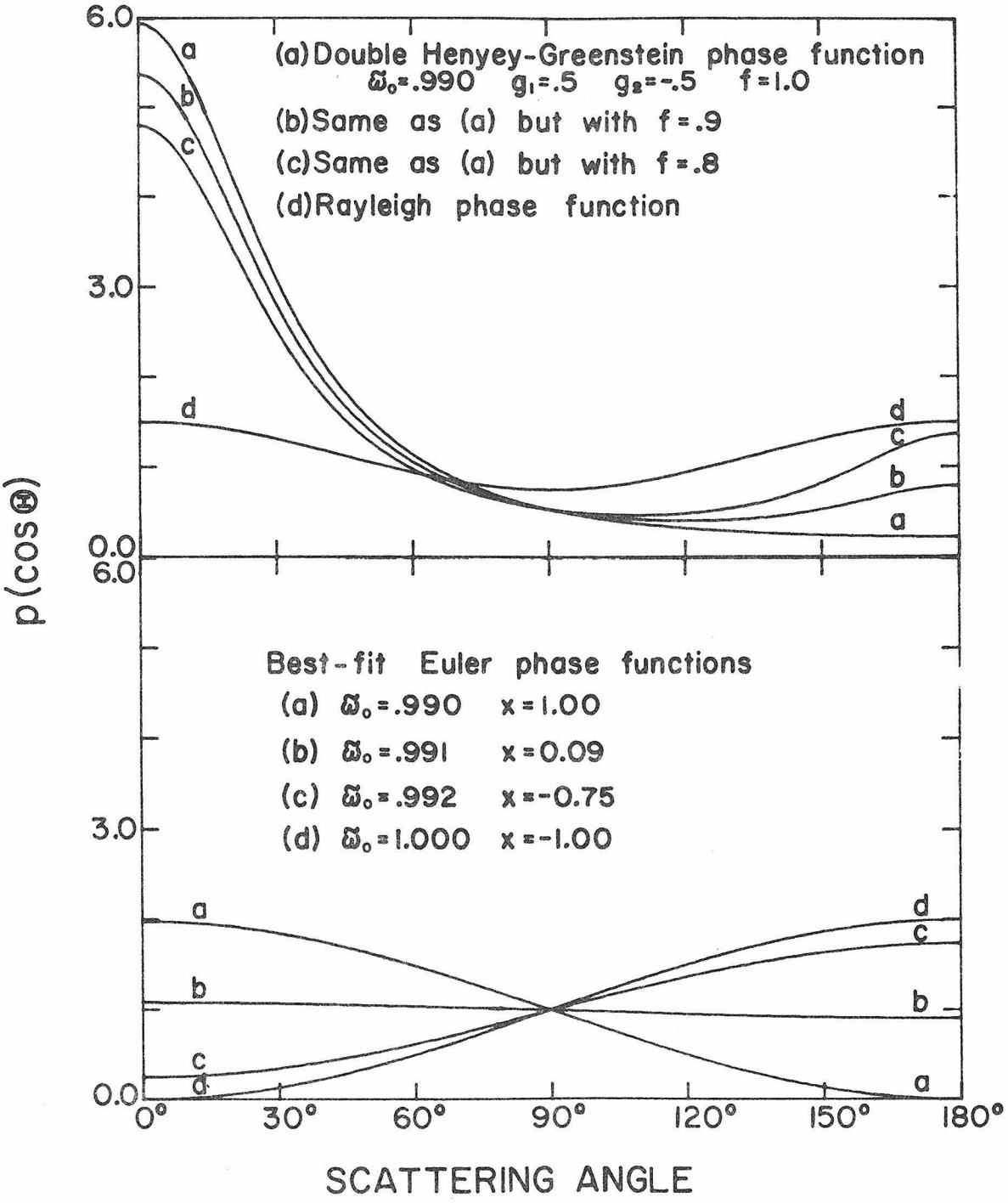
(a) Double Henyey-Greenstein phase function
ϖ₀=.990 g₁=.5 g₂=-.5 f=1.0
(b) Same as (a) but with f=.9
(c) Same as (a) but with f=.8
(d) Rayleigh phase function
Best-fit Euler phase functions
(a) ϖ₀=.990 x=1.00
(b) ϖ₀=.991 x=0.09
(c) ϖ₀=.992 x=-0.75
(d) ϖ₀=1.000 x=-1.00
p(cosΘ)
6.0
3.0
0.0
0°
30°
60°
90°
120°
150°
180°
SCATTERING ANGLE

Figs. 14a, 14b

In practice, the series in equation (15) is terminated at a value of n beyond which additional terms result in no significant contribution to the form of the phase function.

Best-fit limb-darkening curves predicted by the Euler scattering model were arrived at for the limb-darkening of the Rayleigh and Henyey-Greenstein models in the same manner as was done for the actual Jupiter data, following the practice of ignoring data close to the limbs. The best-fit values of $\tilde{\omega}_o$ and x for each of the four models are tabulated in Figure 14b. The limb-darkening curves for each model and their associated best-fit Euler limb-darkening profiles are displayed in Figure 15. In the case of the Rayleigh phase function and the most forward-throwing Henyey-Greenstein function, the best-fit values of x are -1 and +1, respectively, and are therefore, in a sense, "up against the stops," since $|x|$ can not be larger than unity. This gives rise to the situation that the limb-darkening curves of the best-fit Euler models in these two cases are only fair approximations to the limb-darkening predicted by the actual phase functions. On the other hand, for the two double Henyey-Greenstein phase functions with backscattering lobes, the returned x values are well within the allowable limits (i.e., $-1 < x < 1$), and the Euler limb-darkening profiles agree with the limb-darkening of the Henyey-Greenstein functions to better than 1.5-2.0% at all points. In all cases, the modeling returns values of $\tilde{\omega}_o$ which are very close to the single scattering albedos of the input phase functions, but the returned values of x

Figure 15. Comparison of full phase limb-darkening curves for each of the semi-infinite model atmospheres having the four phase functions shown in Figure 14a with the best-fit Euler scattering models having the phase functions shown in Figure 14b. The curves are labeled "a," "b," "c," and "d" for identification with the phase functions in Figures 14a and 14b. In the two cases in which the Euler best-fit asymmetry parameter is either +1 or -1, the Euler limb-darkening is only a fair approximation; however, when the asymmetry parameter adopts values that are well within the allowable range ($-1<x<1$), the Euler limb-darkening never deviates by more than 2% at any point from the limb-darkening of the more complicated models. (DHG = double Henyey-Greenstein phase function.)

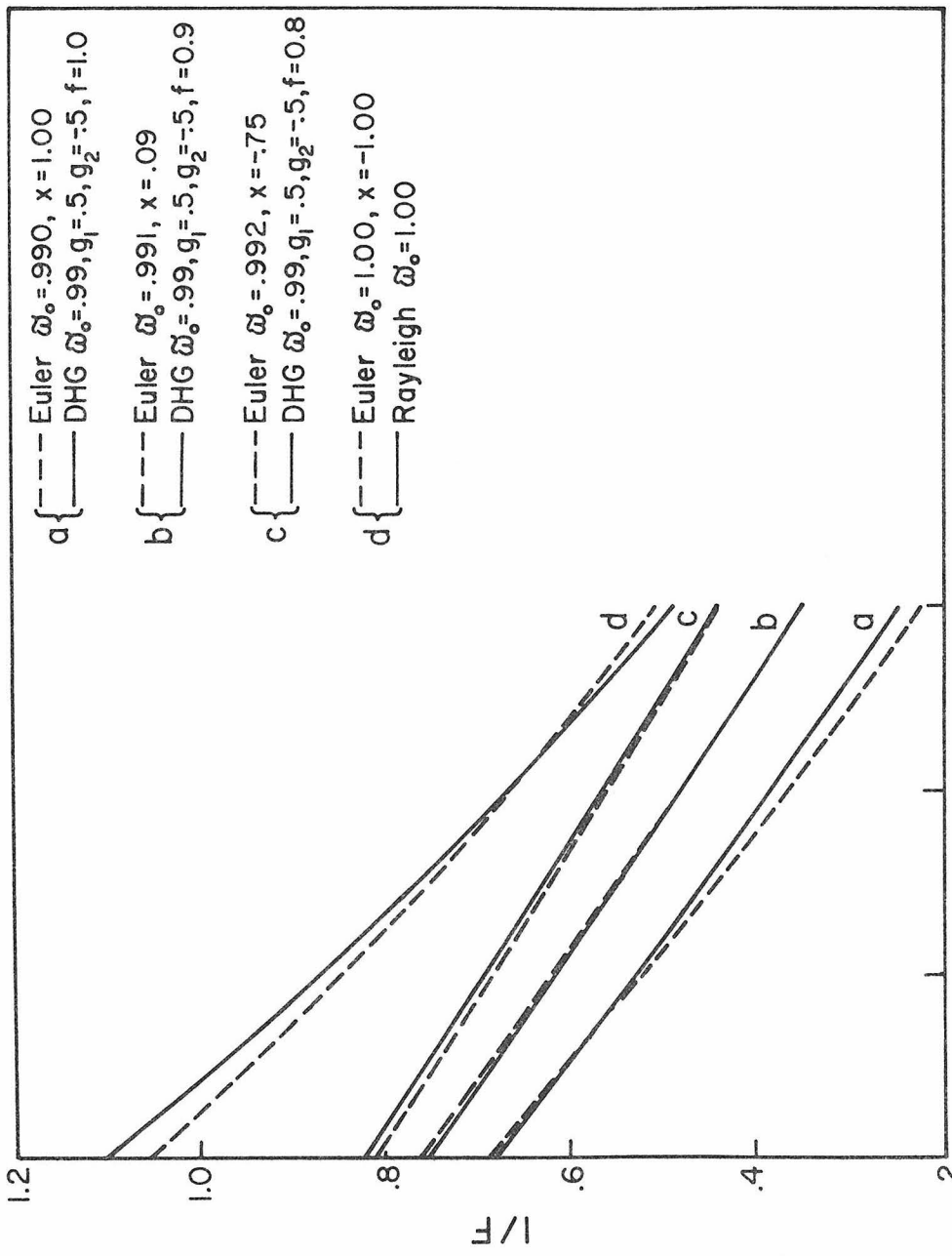
a {--- Euler ϖ₀=.990, x=1.00
—— DHG ϖ₀=.99, g₁=.5, g₂=-.5, f=1.0
b {--- Euler ϖ₀=.991, x=.09
—— DHG ϖ₀=.99, g₁=.5, g₂=-.5, f=0.9
c {--- Euler ϖ₀=.992, x=-.75
—— DHG ϖ₀=.99, g₁=.5, g₂=-.5, f=0.8
d {--- Euler ϖ₀=1.00, x=-1.00
—— Rayleigh ϖ₀=1.00
1/Γ
μ
1.2
1.0
.8
.6
.4
.2
1.0
.8
.6
.4
a
b
c
d

Fig. 15

do not necessarily indicate the overall shape of this function. Although this demonstration reveals some of the limitations of the Euler scattering model, the significant result is that as the magnitude of the backward scattering lobe of the single scattering phase function increases, the value of x determined from a fit of the Euler model to the full phase limb-darkening tends toward more negative values. This point deserves considerable emphasis, since it implies that relative trends in x from one spectral or spatial region to another indicate actual differences in the shapes of the single scattering phase functions, at least qualitatively.

Returning to the observations, the difference between belts and zones is most pronounced at 4115Å, where both the NEB and SEB are more backward scattering than the NTrZ and $STrZ_s$. The NEB at all wavelengths is more backscattering than the $STrZ_s$, but the NTrZ and SEB are not as readily distinguishable. This behavior, and reference to Figures 14a and 14b, in which it was demonstrated that Rayleigh scattering is consistent with large negative values of x (i.e., $x \sim -1$), suggest that Rayleigh scattering may be a strong factor governing the reflection properties of the jovian atmosphere at visible wavelengths. The overall trend toward more positive values of x with increasing wavelength is qualitatively consistent with the decrease in cross-section for Rayleigh scattering. Furthermore, the observation that the NEB is more backscattering than the $STrZ_s$ is consistent with the vertical structure of jovian clouds inferred

from 5 μm measurements (Terrile and Westphal, 1977), which suggest that the cloud decks are deeper in the belts than in the zones and thus have a greater abundance of overlying gas. If the Rayleigh scattering is attributed solely to the gaseous atmosphere, the fact that the single scattering albedo is always less than unity implies that some "dirty" material is also present, since molecular scattering is conservative (i.e. $\tilde{\omega}_o = 1$). Alternatively, the Rayleigh scatterers might be particles which are small compared to visible light wavelengths, with single scattering albedos <1. Such fine, absorbing particles may consist of hydrocarbons produced from the photolysis of methane and ethane (Strobel, 1969); their presence has been postulated frequently to account for the reflecting-scattering properties of the jovian atmosphere and to serve as sinks for solar energy, resulting in a thermal inversion near the 100 mbar level (Orton, 1975b). This hypothetical high-altitude "dust layer" is often called Axel dust after Axel (1972) who proposed such a material to explain Jupiter's low UV albedo.

Rayleigh scattering is not the only mechanism which can give rise to enhanced backscatter in single scattering phase functions. A description of the physical basis for backscatter in various types of particles, and a discussion of their relevance to the jovian atmosphere, will be given in the next chapter. It will be argued that Rayleigh scattering is the most promising candidate to explain the backscattering properties implied by the limb structure data, and

simple numerical models which attempt to attribute the spectal dependence of the jovian limb-darkening to molecular scattering and nonconservative Rayleigh scattering will be considered. The remainder of this chapter is devoted to a comparison of the limb-darkening observations to limb-darkening predictions derived from spatially resolved spectroscopic observations across the jovian disk.

From measurements of the center-to-limb variation of the equivalent widths of the H_2 4-0 S(1) quadrupole line (Cochran et al., 1976), Cochran (1976) has developed models of the jovian cloud structure. The equivalent widths are nearly constant across the disk, with a possible initial decrease away from the disk center, followed by an increase at the limb (however, it is not clear how significant the latter variations are, given the estimated errors of the measurements). This behavior is inconsistent with reflecting-layer and homogeneous scattering models. In a reflecting-layer model, in which clear gas overlies a dense cloud, the equivalent widths of absorption features will increase monotonically toward the limb, due to the increased path length through the gas at oblique viewing angles. This type of model is characterized by a long photon mean free path in the clear region above the cloud, and the cloud is assumed to be so dense that photons do not penetrate very deeply and absorption by gas within the cloud is neglected. Homogeneous scattering models, in which the photon mean free path is relatively short, are those in which cloud particles and gas are uniformly mixed. In such models, the equivalent

widths of absorption features decrease toward the limbs, due to the decrease in the mean number of scattering events for photons at high angles of incidence. Danielson and Tomasko (1969) suggested that the relative constancy of equivalent width across most of the disk (compared with the variation predicted by both the reflecting-layer and homogeneous scattering models) could be explained by a model which combines the long mean free path of the reflecting-layer model with the short mean free path of the homogeneous scattering model. They proposed a vertically inhomogeneous two-cloud model with a semi-infinite lower cloud and a finite thickness upper cloud. Cloud-free H_2 gas exists in the region between the two clouds and also overlies the upper cloud. Photons which were directly reflected from the upper cloud or which penetrated the upper cloud and were multiply reflected between the boundaries of the upper and lower clouds before emergence would provide the long mean free path characteristic of the reflecting layer model, and photons which were multiply scattered within the upper cloud would have the short mean free path characteristic of the homogeneous scattering model. Danielson and Tomasko demonstrated that this model is capable of predicting uniform or slightly decreasing equivalent widths across the disk for the H_2 3-0 and 4-0 S(1) quadrupole lines except for sharp increases near the planetary limb. Cochran (1976) considered such a model, and varied the scattering properties of the cloud particles and the abundance of H_2 in and above the clouds so as to obtain a good fit to the observational data.

The precise magnitude and slope of the increase in equivalent width at the limb is difficult to measure due to the smearing effect of atmospheric seeing. Cochran modeled the observed increase by including a backscattering lobe in the phase function of the upper cloud, although isotropic scattering in this cloud would serve as well. Since the data close to the limb are subject to severe smearing, it is problematical whether this backscatter lobe in the cloud particle phase function is absolutely required. In any case, Cochran found a satisfactory fit to the equivalent width data by assuming 35 km-amagat of H_2 between the two clouds, 25 km-amagat of H_2 above the upper cloud, 2 km-amagat of H_2 within the upper cloud, a single scattering albedo of 0.991 for both clouds, and a single scattering phase function of the upper cloud of the type given by equation (14), with $g_1 = 0.71$, $g_2 = -0.76$, and $f = 0.96$. The upper cloud has an optical depth for scattering of 4. The models were not sensitive to the specific shape of the single scattering phase function of the lower cloud, and the photon mean free path was assumed to be small within this cloud so that absorption by H_2 could be neglected. With this model, it was necessary to include a dust layer of small particles with complex index of refraction varying as $\lambda^{-2.5}$ in order to match the spectral reflectivity data of Orton (1975a). Regional reflectivity contrasts were accounted for by assuming a larger abundance of dust in belts relative to zones, and the upper 10 km-amagat of gas were left dust-free so that molecular scattering in the clouds would provide

qualitatively shallower limb-darkening in the blue relative to the red. Cochran also considered a second model which contained an upper layer of cloud-free H_2 gas overlying a homogeneous mixture of cloud particles and gas. In this reflecting-scattering model, as in the two-cloud model, the gas abundances and cloud scattering parameters were adjusted to fit the observed center-to-limb variation in the line equivalent widths. The decrease in reflectivity of Jupiter toward the ultraviolet was again accounted for by the inclusion of a fine, colored dust in the clouds. In the reflecting-scattering model, as with the two-cloud model, an enhanced backscattering lobe was included in the particle single-scattering phase function, and the identical double Henyey-Greenstein function was adopted.

Cochran's models are fairly complex, but there is no guarantee that the gas abundances and cloud scattering parameters which he derived are unique. Unfortunately, the parameters of the single scattering double Henyey-Greenstein phase function were not derived independently from the center-to-limb equivalent width measurements but were adapted from a fit of this analytic function (Kattawar, 1975) to the phase function of a polydispersion of spherical particles with a particle mode radius of 0.07 μm [Deirmendjian's (1969) "Haze L" distribution] and refractive index of 1.55. Cochran points out that an isotropically scattering cloud can also reproduce the center-to-limb variation in the H_2 line; although he remarks that the limb-darkening of such an isotropically scattering model would be too

shallow, he cites no quantitative comparison with actual limb-darkening observations. In fact, Figure 9 (see Chapter 4) shows that longward of 5000Å most regions on the jovian disk exhibit limb-darkening that is consistent with isotropic scattering. Since the shapes of cloud single scattering phase functions affect not only the magnitudes of increases in equivalent widths near the planetary limb but the shapes of limb-darkening profiles as well, it is clear that the center-to-limb variation in continuum brightness is an indispensable constraint in the formulation of atmospheric models.

Cochran calculated full phase limb-darkening profiles for his two-cloud and reflecting-scattering models. Although both models fit the equivalent width data equally well, they are distinguishable by their predictions regarding limb-darkening. The spectral variation of the limb-darkening is determined by the changing Rayleigh scattering optical depth and the wavelength dependence of the dust properties. Cochran's results for the STrZ and NEB at 4000, 5000, and 6000Å are shown in Figures 16 and 17, respectively, superimposed upon the Euler scattering model fits to the SIVIT data at 4115, 4865, and 5810Å. Despite the fact that Cochran did not use quantitative limb-darkening measurements in the development of his two-cloud and reflecting-scattering models, both are moderately successful in matching the normalized STrZ limb-darkening data. [Note, however, that when Cochran's limb-darkening curves are plotted in units of I/F, they do not match the observations very well, i.e., they are

Figure 16. Comparison of the limb-darkening curves at 4115, 4865, and 5810Å with Cochran's (1976) inhomogeneous models for the South Tropical Zone at 4000, 5000, and 6000Å.

Figure 17. Same as Figure 16 but for the North Equatorial Belt.

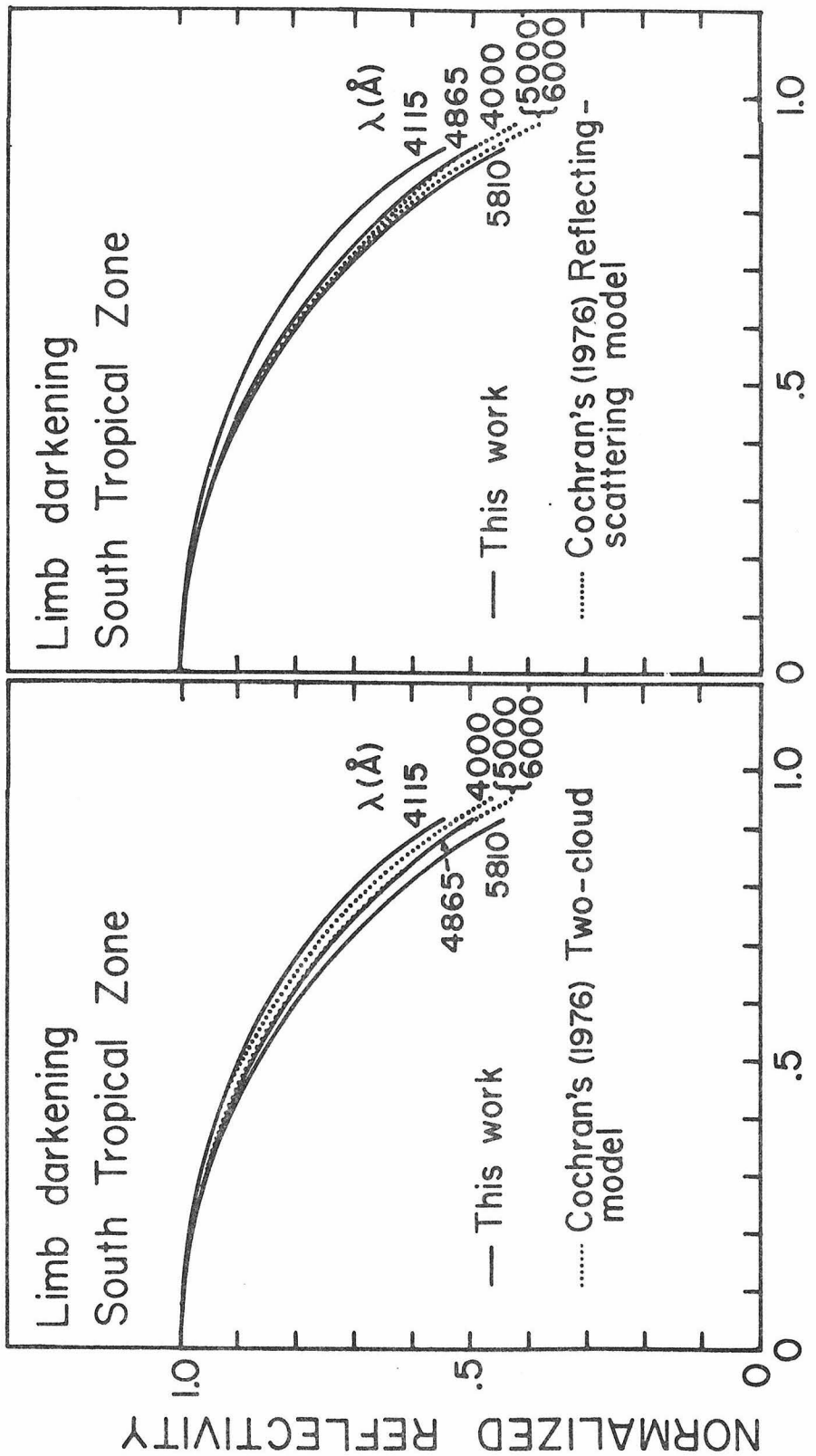
Limb darkening
South Tropical Zone
λ(Å)
4115
4865
5810
4000
5000
6000
This work
Cochran's (1976) Two-cloud model
Cochran's (1976) Reflecting-scattering model
NORMALIZED REFLECTIVITY
NORMALIZED RADIUS
0
.5
1.0

Fig. 16

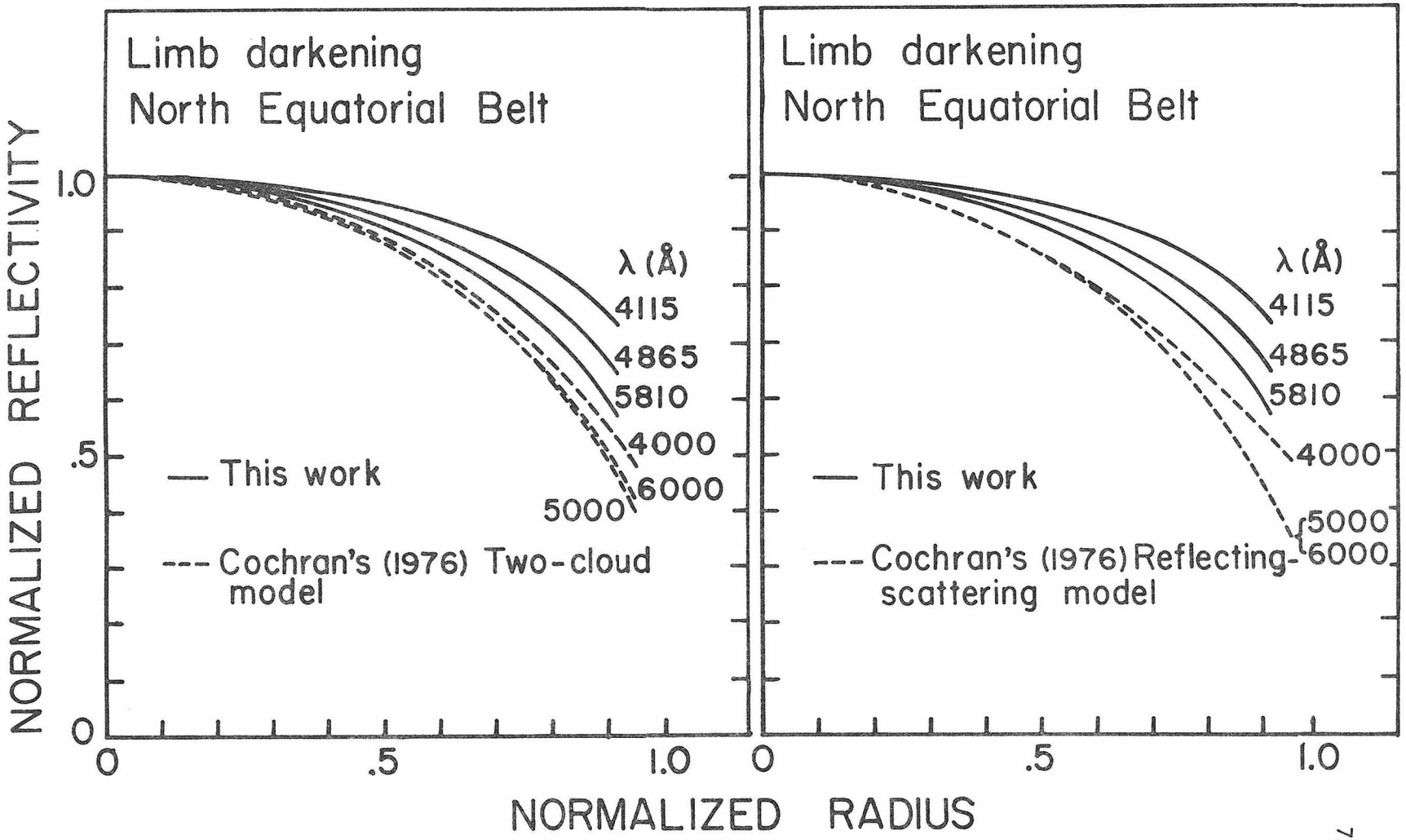
Limb darkening
North Equatorial Belt
Limb darkening
North Equatorial Belt
NORMALIZED REFLECTIVITY
1.0
.5
0
0
.5
1.0
λ (Å)
4115
4865
5810
4000
6000
5000
— This work
--- Cochran's (1976) Two-cloud model
— This work
--- Cochran's (1976) Reflecting-scattering model
NORMALIZED RADIUS

Fig. 17

systematically too low (Bergstralh, 1977)]. The two-cloud model is in better agreement with the normalized data at the shortest wavelength, where the modeling of the dust properties and Rayleigh scattering is most critical. On the other hand, neither model adequately predicts the shape of the NEB limb structure data. The observed limb-darkening is in general less steep than that predicted by the models; however, Cochran points out that the NEB equivalent width data may be influenced by contributions from adjacent bright zones due to poor seeing. The vidicon data also reveal a statistically significant difference in the shapes of the limb-darkening profiles near 5000 and 6000Å, a result which is not duplicated by either of Cochran's models for the STrZ, nor in the reflecting-scattering model for the NEB; the difference in the limb-darkening at 5000 and 6000Å in the two-cloud NEB model is in the sense opposite to the observations. Improved fits to the NEB limb-darkening data might be obtained by decreasing the cloud single scattering albedo, by increasing the amount of backscattering by the cloud particles, and/or by including a greater contribution to the atmospheric reflection function by Rayleigh scattering. It is also possible that Cochran's hypothesis that the only difference between belts and zones is in the relative abundance of dust is oversimplified (Tomasko et al., 1976), and that the vertical structure of the STrZ may be on the whole quite different from the NEB. Simultaneous center-to-limb equivalent width and reflectivity measurements would resolve any doubts that arise from the fact that the data discussed by Cochran were obtained in

1974 while the limb-darkening measurements were obtained late in 1975, a predicament which leaves open the possibility that the structure of Jupiter's clouds changed during this time interval. Simultaneous measurements would provide a useful data base upon which models consistent with both the spatial equivalent width and spectral reflectivity variations could be derived.

Chapter 7

ATMOSPHERIC STRUCTURE

"Contrariwise," continued Tweedledee,
"if it was so, it might be;
and if it were so, it would be:
but as it isn't, it ain't. That's logic."

- Lewis Carroll
Alice Through the Looking Glass

In this chapter, several atmospheric models which incorporate the Euler scattering parameterization discussed in the preceding chapter will be considered in an attempt to explain the observed jovian limb-darkening. For models with more than two parameters, the problem of fitting solutions of the highly non-linear multiple scattering equations to actual data is rather gruesome. A simpler approach was introduced in the preceding chapter, in which model limb-darkening curves were fitted by the two-parameter Euler scattering model, and the solutions for $\tilde{\omega}_o$ and x were compared with the values determined for these parameters from actual data. Since absolute reflectivity dominates the solution for $\tilde{\omega}_o$, and the relative shape of a limb structure profile mainly influences the value for x, this technique is reasonable.

It was noted earlier that the limb-darkening data imply an enhanced backscattering lobe in the single scattering phase function of some constituent with appreciable optical thickness in the jovian atmosphere. A number of physical phenomena which give rise to enhanced backscatter occur in transparent or semi-transparent

spherical particles of sizes comparable to and larger than the wavelength of the incident light (that is, $\gtrsim 0.5\,\mu m$ in radius). Enhanced backscattering may arise from rays which undergo one internal reflection and re-emerge at a scattering angle of 180°, provided that the refractive index is in the range $\sqrt{2} \leq n \leq 2$. Rays which are backscattered after more than one internal reflection are generally of weaker intensity and thus do not give rise to as pronounced an effect. An interference phenomenon which may cause enhanced backscatter results from waves which traverse part of the surface of the particle and constructively interfere in the forward and backward scattering directions (Bryant and Jarmie, 1974). The combined effect of all backscattered rays, known as the glory, can be calculated from Mie theory for scattering by spheres.

Unfortunately, it is unlikely that Mie theory is appropriate for Jupiter's visible clouds. Weidenschilling and Lewis (1973) have calculated chemical equilibrium cloud models based on various assumptions regarding the composition of the jovian atmosphere. The major cloud layers predicted by the models are an uppermost layer of NH_3 ice, an intermediate cloud of solid NH_4SH particles, and a lower cloud composed of H_2O ice. Since these substances form crystalline solids, the macroscopic aerosol particles are unlikely to be perfect spheres; instead, one expects them to be polyhedral or irregular in shape. Convex polyhedral particles exhibit very slight enhancements

in backscattered intensity (Zerull, 1976), but the effect is considerably less pronounced than in the case of spherical particles. Zerull and Giese (1974) have shown that the intensity of the scattering phase function for randomly oriented cubes with sizes on the order of the wavelength of incident light is practically independent of scattering angle for $\theta \geq 90°$ and no backscatter enhancement occurs. In general, as the degree of nonsphericity increases, scattering at intermediate angles (sideward scattering) increases at the expense of backscattering. One may conclude, therefore, that the single scattering phase functions which have been adopted by Tomasko et al. (1976) to explain the Pioneer 10 IPP results and by Cochran (1976) to explain the center-to-limb variation in equivalent width of the hydrogen quadrupole lines do not accurately portray the scattering expected from jovian cloud particles. These investigators make use of double Henyey-Greenstein phase functions which have strong forward scattering peaks to represent diffraction effects and smaller backscatter lobes to approximate glories. Although Weidenschilling and Lewis' models predict some aqueous ammonia solutions below the water ice cloud at about the 7 bar level, this layer is too deep and too thin to affect the visible reflection properties of the jovian atmosphere significantly, particularly in the zones where the optical thickness of the topmost NH_3 ice cloud is probably the largest. Cochran's (1976) models put the cloud particles as high

as the 1 bar level. Given that liquid (and therefore spherical) droplets probably do not exist at this altitude (unless Weidenschilling and Lewis' models are highly unrepresentative of the real atmospheric chemistry), one must be very cautious in attributing the backscattering properties of the belts and zones to a glory in the single scattering phase functions of the cloud particles.

Rayleigh scattering, on the other hand, exhibits enhanced backscatter even for irregularly shaped particles, and occurs when the sizes of the scattering particles are considerably smaller than $\lambda/|m|$, where λ is the wavelength of the incident light and $m = n - ik'$ is the complex refractive index. In scattering of this type, the intensity of the scattered light is proportional to $(1 + \cos^2 \theta)$ and the integral of this distribution over 4π steradians requires that the constant of proportionality be $3\,\tilde{\omega}_o/4$, where $\tilde{\omega}_o$ is the single scattering albedo. The shape of this phase function has been displayed in Figure 14a for the case $\tilde{\omega}_o = 1$. A specific instance of conservative Rayleigh scattering is scattering by the molecules in a gas. Reconciliation of the limb-darkening observations, which require enhanced backscatter, with the argument that the expected cloud particles probably do not exhibit such effects (if they are half-micron size or larger), may be obtained if it is assumed 1) that the cloud particles are small and scatter in the Rayleigh domain; 2) molecular Rayleigh scattering in the atmospheric gas contributes significantly to the jovian reflection properties; or 3) a Rayleigh scattering aerosol,

chemically distinct from the main cloud constituents (for example, a photochemical dust) is present in or above the clouds. This chapter shall therefore consider some simple atmospheric models in order to determine the extent to which Rayleigh scattering, by gas molecules and nonconservative particles, can explain the jovian limb-darkening. Initially, the models will concentrate on the limb-darkening properties of the North Equatorial Belt, since this region exhibits the strongest backscattering (i.e., the shallowest limb-darkening for a given wavelength), and therefore serves as the most critical test of the Rayleigh scattering hypothesis.

Table IV presents the results of fitting the Euler scattering model to limb-darkening of semi-infinite homogeneous Rayleigh scattering atmospheres in which the particles take on various values of single scattering albedo. The calculations show that the best-fit value of $\tilde{\omega}_o$ in the Euler model is almost identical to the value associated with the input phase function, a result which has already been demonstrated in the case of the more complicated double Henyey-Greenstein phase functions. The calculations also show that, at least in the range $\tilde{\omega}_o = 0.892$ to $\tilde{\omega}_o = 0.995$, the best-fitting values of the asymmetry parameter x are consistently in the range -0.7 to -0.8. Note that this simple Rayleigh scattering model, with a single scattering albedo of 0.892, almost exactly reproduces the observed limb-darkening and absolute reflectivity of the NEB at 4115Å (see Figures 8 and 9). Although such a model is not unique, it is an

TABLE IV

Euler scattering model parameterizations of full phase limb-darkening of semi-infinite Rayleigh scattering atmospheres with various values of single scattering albedo

Rayleigh scattering $\tilde{\omega}_o$	Euler best-fit $\tilde{\omega}_o$	Euler best-fit x
1.000	1.000	-1.00
0.995	0.996	-0.75
0.990	0.991	-0.72
0.980	0.980	-0.77
0.900	0.891	-0.79
0.892	0.883	-0.76

appropriate starting point for an investigation of the limb-darkening at the longer wavelengths. Clearly, since the model yields $x < -0.7$ independent of the value of $\tilde{\omega}_o$, it fails at wavelengths longer than 5000Å (see Figure 9).

Attempts to make a Rayleigh scattering model work for the NEB at all wavelengths will be divided into two categories, each of which assumes the presence of an atmospheric constituent with particles much smaller than visible wavelengths and of substantial optical depth at 4115Å. These categories are: 1) a semi-infinite nonconservative Rayleigh scattering atmosphere over which lies a cloud layer of finite optical depth; and 2) a semi-infinite Rayleigh scattering atmosphere homogeneously mixed at all altitudes with particles of another type. It will be shown that each category contains models capable of reproducing the observations, and the implications regarding the jovian atmospheric structure will be discussed. In keeping with the philosophy of minimizing the number of model parameters, complex models with discrete layers and distinct phase functions will not be considered; furthermore, it is unlikely that the full phase limb-darkening data are by themselves capable of justifying such an endeavor.

Category 1 models

Table V presents the Euler parameterization of the limb-darkening of three semi-infinite model atmospheres, and the Euler parameterization of the limb-darkening of the same models with an overlying pure absorbing layer ($\tilde{\omega}_o = 0$) of optical depth $\tau = 0.05$. The semi-infinite

TABLE V

Euler scattering model parameterizations of three semi-infinite atmospheres with and without an overlying pure absorbing ($\tilde{\omega}_o = 0$) layer of optical depth $\tau = 0.05$.

Model 1: Isotropic scattering, $\tilde{\omega}_o = 0.99$

Model 2: Rayleigh scattering, $\tilde{\omega}_o = 0.99$

Model 3: Rayleigh scattering, $\tilde{\omega}_o = 1$

	Without absorbing layer		With absorbing layer	
	Euler best-fit $\tilde{\omega}_o$	Euler best-fit x	Euler best-fit $\tilde{\omega}_o$	Euler best-fit x
Model 1	0.990	0	0.986	0.70
Model 2	0.991	-0.72	0.987	0.05
Model 3	1.000	-1.00	0.9999	0.28

model atmospheres are, in the first case isotropically scattering with $\tilde{\omega}_o = 0.99$, in the second case Rayleigh scattering with $\tilde{\omega}_o = 0.99$, and in the third case Rayleigh scattering with $\tilde{\omega}_o = 1$. The choice of a non-scattering overlying layer makes it unnecessary to specify explicitly the particle phase function and permits the effect of the layer on the reflection properties of the atmosphere to be understood easily. The thin absorber modulates the shape of the limb-darkening of the semi-infinite atmosphere by a factor $\exp\left[-\tau\left(\frac{1}{\mu}+\frac{1}{\mu_o}\right)\right]$, or simply $\exp(-2\tau/\mu)$ since the calculations assume full phase such that $\mu = \mu_o$. In each of the three cases, the effect of the absorber on the Euler parameterization of the limb-darkening is to reduce the value of $\tilde{\omega}_o$ only slightly while increasing x to a positive value rather easily. This behavior arises from the $1/\mu$ dependence in the exponent of the modulating function: the central disk brightness is not reduced by as large a factor as locations nearer the limb, with the net effect of steepening the limb-darkening. One may expect, based on these examples, that proper choice of τ will make any model atmosphere appear more forward scattering by a desired amount, while the value of $\tilde{\omega}_o$ will remain virtually unchanged. This allows for a very simple two-parameter, two-layer model for the NEB: a semi-infinite cloud of fine particles whose single scattering albedo is roughly given at each wavelength by the values determined from the data and displayed in Figure 8, and over which lies a pure absorbing layer of variable optical depth which adopts the particular value of τ at each

wavelength so as to yield the values of asymmetry parameter displayed in Figure 9. This thin absorber must have zero optical depth in the blue, with non-zero values in the green and red. The required quantitative dependence of τ on wavelength is given in Table VI. If it is assumed that this layer has an actual geometric thickness Δz, and the particle density N and absorption cross section k are constant over this depth, then the optical thickness is given by

$$\tau = \int_{\Delta z} kNdz = kN\Delta z \tag{17}$$

and thus except for a constant of proportionality Table VI may also be interpreted as the spectral dependence of the absorption coefficient. Barring any input from other sources of data, the success or failure of this model rests on the possibility of finding a material which has zero scattering efficiency and whose absorption efficiency depends on wavelength as given by Table VI. The requirement that $\tilde{\omega}_o \sim 0$ means that $Q_{sca} << Q_{abs}$, which is possible if the particles in this layer are themselves in the Rayleigh domain (i.e., small compared to the wavelength of visible light). Table VI implies that such particles must be better absorbers in the green and red relative to the blue. This requirement is not consistent with the spectral characteristics of substances which may be produced photochemically in the jovian atmosphere (Khare and Sagan, 1973). Thus, the physical case for this particular model is weak, despite its phenomenological success in reproducing the limb structure data.

TABLE VI

Optical depth of absorbing layer above semi-infinite Rayleigh scattering atmospheres required to fit the observed NEB limb-darkening. The single scattering albedo of the Rayleigh scatterers is assumed equal to the values given in Figure 8 for each wavelength channel.

λ	τ
4115Å	0
4865Å	0
5460Å	0.016
5810Å	0.018
7440Å	0.031
8290Å	0.021

Category 2 models

The second category of models to be considered involves homogeneous mixtures of Rayleigh scatterers with particles having a different phase function. The effective single scattering phase function of such a mixture is given by

$$p(\cos\theta) = b \cdot p_{Rayleigh}(\cos\theta) + (1-b) \cdot p_{other}(\cos\theta) \qquad (18)$$

where the parameter b represents the probability that a photon will undergo Rayleigh scattering in a particular event, and (1 - b) is the probability that the photon will be scattered by the other type of particle. The parameter is defined such that

$$b = \frac{\tau_R}{\tau_R + \tau} \qquad (19)$$

where τ_R = Rayleigh optical depth and τ = "other" particle optical depth. These optical depths refer to a given atmospheric level and thus it is possible for b to be a function of height. Clearly, it will be simplest to consider models in which b is assumed to be independent of altitude. This simplifying assumption is reasonable if the optical properties of the scatterers are independent of height and if the scale heights of all atmospheric constituents are equal. Assuming that the Rayleigh scatterers are uniform in size and that they can be characterized by an effective radius r, the Rayleigh

optical depth above a height z is given by

$$\tau_R = \int_z^\infty k(z)N(z)dz = \int_z^\infty G\, Q_{ext}(z)N(z)dz \tag{20}$$

where Q_{ext} is the extinction efficiency (the ratio of the extinction cross section to the geometric cross section G); Q_{ext} is the sum of the scattering efficiency and absorption efficiency, $Q_{sca} + Q_{abs}$. For Rayleigh scattering,

$$Q_{sca} = \frac{8}{3} a^4 \left| \frac{m^2 - 1}{m^2 + 2} \right|^2 \tag{21a}$$

$$Q_{abs} = -4a \, \mathrm{Im} \left\{ \frac{m^2 - 1}{m^2 + 2} \right\} \tag{21b}$$

(van de Hulst, 1957), where $a = 2\pi r/\lambda$, λ = wavelength and m is the complex index of refraction = $n - ik'$. Thus, if the refractive index and particle size are independent of height, G and Q_{ext} can be taken outside the integral in equation (20), and τ_R at a given level will be proportional to Q_{ext}. The Rayleigh single scattering albedo can be expressed as

$$\tilde{\omega}_{o_R} = \frac{Q_{sca}}{Q_{sca} + Q_{abs}} = \frac{Q_{sca}}{Q_{ext}} \quad . \tag{22}$$

Thus, if $\tilde{\omega}_{o_R}$ is large (i.e., $Q_{sca} >> Q_{abs}$), the Rayleigh optical depth will vary as λ^{-4}; if $\tilde{\omega}_{o_R}$ is small (i.e., $Q_{sca} << Q_{abs}$), τ_R will vary as λ^{-1} (equations 21a and 21b).

At the outset, the model will be very simple. Relaxation of any imposed constraints and use of additional parameters will be permitted only if required by some failure of the model to reproduce the observed NEB limb structure data. In any case, the main objective is to hold Rayleigh scattering responsible for the observed backscattering; the "other" particles are invoked primarily to account for any differences between the observed limb structure and that of a pure Rayleigh scattering atmosphere. The specific goal will be to determine whether the "other" particles can be primarily forward scattering without enhanced backscatter, as expected for the solid particles which probably comprise the visible jovian clouds.

In the first model to be tested, it will be assumed that the extinction coefficient of the "other" particles is independent of wavelength, a reasonable assumption if, for example, the particles are grey absorbers and very large in comparison to the wavelength of visible light. This assumption means that τ is taken to be a constant. The Rayleigh single scattering albedo and the single scattering albedo of the "other" particles also will not be permitted to vary with wavelength. Therefore, the spectral behavior of this model will be determined only by the variation of τ_R.

The following calculations will demonstrate that a λ^{-4} dependence of τ_R is insufficient to account for the variation in effective single scattering albedo of the NEB from 4115Å to 8290Å, given the constraints of this particular model. Therefore, a more gradually varying

dependence (e.g., λ^{-1}) will be even less adequate than the λ^{-4} case. To simplify the calculations, τ_R will be assumed to follow a λ^{-4} law, i.e., $\tau_R = \tau_{R_o} (\lambda/\lambda_o)^{-4}$, even though the Rayleigh single scattering albedo will be allowed to assume values <<1.

Under the foregoing assumptions, the parameter b may be written

$$b = \frac{\tau_R}{\tau_R + \tau} = \frac{1}{1 + \left(\frac{\tau}{\tau_{R_o}}\right)\left(\frac{\lambda}{\lambda_o}\right)^4} \quad . \tag{23}$$

λ_o shall be taken as 4115Å. The approach will be to solve for the values of Rayleigh single scattering albedo, $\tilde{\omega}_{o_R}$, the single scattering albedo of the "other" particles, $\tilde{\omega}_o'$, and values of b which are consistent with the observed effective single scattering albedos at 4115 and 8290Å, and then to use these values and the wavelength dependence of b as given by equation (23) to predict the effective single scattering albedo at intermediate wavelengths. At all wavelengths, this albedo is represented by

$$\tilde{\omega}_{o_{eff}} = b\, \tilde{\omega}_{o_R} + (1-b)\, \tilde{\omega}_o' \quad . \tag{24}$$

In all test cases which have been discussed heretofore, the Euler scattering model best-fit values of $\tilde{\omega}_o$ were quite close to the actual input values. Therefore, the values of $\tilde{\omega}_o$ given in Figure 8, as determined from the observational data, will be assumed to be identical to $\tilde{\omega}_{o_{eff}}$. Since the purpose of considering this simple model is to determine whether the wavelength dependence of Rayleigh optical depth

can successfully reproduce the observed spectral behavior of $\tilde{\omega}_{o_{eff}}$, it is not necessary to specify explicitly the single scattering phase function of the "other" particles. This will become necessary later, however, when the attempt is made to match the observed behavior of the asymmetry parameter, x. It is appropriate, however, that such a step should hinge on a successful modeling of $\tilde{\omega}_o$, which is the better determined of the two parameters.

The observed values of $\tilde{\omega}_o$ at 4115 and 8290Å are 0.892 and 0.990, respectively. Thus, one may write

$$b_{4115}\,\tilde{\omega}_{o_R} + (1-b_{4115})\tilde{\omega}_o' = \frac{1}{1+\left(\tau/\tau_{R_o}\right)}\tilde{\omega}_{o_R} + \frac{\left(\tau/\tau_{R_o}\right)}{1+\left(\tau/\tau_{R_o}\right)}\tilde{\omega}_o' = 0.892 \quad (25a)$$

$$b_{8290}\,\tilde{\omega}_{o_R} + (1-b_{8290})\tilde{\omega}_o' = \frac{1}{1+16.472\left(\tau/\tau_{R_o}\right)}\tilde{\omega}_{o_R} + \frac{16.472\left(\tau/\tau_{R_o}\right)}{1+16.472\left(\tau/\tau_{R_o}\right)}\tilde{\omega}_o' = 0.990 \quad (25b)$$

using the fact that $(8290/4115)^4 = 16.472$. Eliminating $\tilde{\omega}_{o_R}$ from these equations, one obtains

$$\tilde{\omega}_o' = (6.334 \times 10^{-3})\,\frac{\tau_{R_o}}{\tau} + 0.9963 \quad . \quad (26)$$

Therefore, $\tilde{\omega}_o'$ must be $\geq$ 0.9963, since τ_{R_o}/τ cannot be negative. Solving for $\tilde{\omega}_{o_R}$,

$$\tilde{\omega}_{o_R} = 0.886 - 0.104 \frac{\tau}{\tau_{R_o}} \quad . \tag{27}$$

This equation sets an upper limit on τ/τ_{R_o}, since $\tilde{\omega}_{o_R}$ cannot be less than zero. This value, $(\tau/\tau_{R_o})_{o\ max}$, is 8.519. Furthermore, since (τ/τ_{R_o}) must be ≥ 0, $\tilde{\omega}_{o_R}$ has a maximum allowable value of 0.886. The upper limit on τ/τ_{R_o} of 8.519 implies a lower limit on τ_{R_o}/τ given by 1/8.519 = 0.117. Therefore, the lower limit on $\tilde{\omega}_o'$ is even stricter than implied by equation (26) alone, and is equal to $(6.334 \times 10^{-3}) \cdot (0.117) + 0.9963 = 0.997$. Moreover, $\tilde{\omega}_o'$ cannot be greater than unity, so τ_{R_o}/τ may not take on values larger than $(1 - 0.9963)/(6.334 \times 10^{-3}) = 0.584$; this implies $(\tau/\tau_{R_o})_{o\ min} = 1/0.584 = 1.712$. Finally, this imposes a stronger limit on the maximum allowable value of $\tilde{\omega}_{o_R}$, and by virtue of equation (27), this value, $\left(\tilde{\omega}_{o_R}\right)_{max}$, is 0.708.

Summarizing the constraints,

$$0.997 \leq \tilde{\omega}_o' \leq 1 \tag{28a}$$

$$0 \leq \tilde{\omega}_{o_R} \leq 0.708 \tag{28b}$$

$$8.519 \geq \tau/\tau_{R_o} \geq 1.712 \quad . \tag{28c}$$

Since $\tilde{\omega}_{o_R}$ and $\tilde{\omega}_o'$ are taken to be constants, it is possible to consider the two extreme cases: $\tau/\tau_{R_o} = 1.712$, $\tilde{\omega}_{o_R} = 0.708$, $\tilde{\omega}_o' = 1$; and $\tau/\tau_{R_o} = 8.519$, $\tilde{\omega}_{o_R} = 0$, $\tilde{\omega}_o' = 0.997$.

Table VII presents the predictions of these two extreme cases regarding $\tilde{\omega}_{o_{eff}}$ vs. λ, and compares these predictions with the observed values of $\tilde{\omega}_o$. It is seen that the λ^{-4} dependence of τ_R is insufficient to match the steep rise in $\tilde{\omega}_o$ from the blue to the green, and thus a gentler wavelength dependence of τ_R will give an even worse fit. It may be shown, in fact, that under the assumptions of this model, if τ_R is taken to be proportional to $\lambda^{-\beta}$, physical solutions (i.e., values of $\tilde{\omega}_o' \leq 1$) cannot be obtained if $\beta<3.4$. It is therefore not even necessary to consider the asymmetry parameter, x, in order to eliminate this model.

The next logical step is to relax one (or more) of the imposed constraints; i.e., to allow either $\tilde{\omega}_{o_R}$ or $\tilde{\omega}_o'$, or both, to vary with wavelength. Since this will permit the observed values of $\tilde{\omega}_o$ to be reproduced, it will be necessary to invoke the observed asymmetry parameter, x, and its spectral dependence, to test the validity of such models. It is impractical to consider all possible models, so for demonstrative purposes, a few numerical examples will be worked out. The first supposes that the "other" particles constitute the main cloud component of the NEB, and the particles are considered to be mixed homogeneously with a conservative Rayleigh scattering gas and to scatter according to the Euler phase function. Admittedly, this phase function is chosen for its mathematical simplicity and cannot duplicate the type of scattering functions exhibited by real particles. However, it was demonstrated that the limb-darkening of a forward scattering phase function with no enhanced

TABLE VII

Values of b and $\tilde{\omega}_{o_{eff}}$ vs. λ for the two extreme cases of the model with Rayleigh scatterers + "other" particles assuming wavelength independent single scattering albedos. The values of $\tilde{\omega}_{o_{eff}}$ are constrained to match the Euler best-fit single scattering albedos determined from the data at 4115 and 8290Å.

λ	b	$\omega_{o_{eff}}$	Euler best-fit $\tilde{\omega}_o$ from NEB data
Case 1: τ/τ_{R_o} = 1.712,		$\tilde{\omega}_{o_R}$ = 0.708,	$\tilde{\omega}_o'$ = 1
4115Å	0.369	0.892	0.892 ± 0.012
4865Å	0.230	0.933	0.964 ± 0.002
5460Å	0.159	0.954	0.973 ± 0.003
5810Å	0.128	0.963	0.973 ± 0.002
7440Å	0.052	0.985	0.991 ± 0.001
8290Å	0.034	0.990	0.990 ± 0.002
Case 2: τ/τ_{R_o} = 8.519,		$\tilde{\omega}_{o_R}$ = 0,	$\tilde{\omega}_o'$ = 0.997
4115Å	0.105	0.892	0.892 ± 0.012
4865Å	0.057	0.940	0.964 ± 0.002
5460Å	0.036	0.961	0.973 ± 0.003
5810Å	0.029	0.968	0.973 ± 0.002
7440Å	0.011	0.986	0.991 ± 0.001
8290Å	0.007	0.990	0.990 ± 0.002

backscatter can be approximated by a forward scattering Euler model. In addition, an increase in the degree of backscatter results in progressively more backscattering Euler functions. The utilization of this qualitative correspondence between Euler scattering and scattering by real particles is further validated by the assertion that the cloud particles are nonspherical, so that details such as rainbows and glories are either absent or appreciably washed out. In the following exercise, the objective will be to investigate whether the backscattering exhibited by the NEB can be explained solely by conservative molecular scattering in the gas, and to determine whether the cloud particles mixed with the gas can be forward scattering without an enhanced backscatter lobe.

The effective scattering function of the atmosphere will be given by equation (18), using $p_{other}(\cos\theta) = \tilde{\omega}_o'(1 + x\cos\theta) = \tilde{\omega}_o'[(1 + x P_1(\cos\theta)]$, the Euler phase function. Equation (18) may then be written

$$p(\cos\theta) = b\left[1 + \frac{1}{2}P_2(\cos\theta)\right] + (1-b)\tilde{\omega}_o'\left[1 + x\,P_1(\cos\theta)\right]$$

$$= [b+(1-b)\tilde{\omega}_o']\left\{1 + \frac{(1-b)\tilde{\omega}_o' x}{b+(1-b)\tilde{\omega}_o'}P_1(\cos\theta) + \frac{b}{2[b+(1-b)\tilde{\omega}_o']}P_2(\cos\theta)\right\}$$

$$= \tilde{\omega}_{o_{eff}}\left\{1 + x_1 P_1(\cos\theta) + x_2 P_2(\cos\theta)\right\} \qquad (29)$$

assuming conservative Rayleigh scattering. It is apparent that in

order to solve the multiple scattering problem a solution to the case of a semi-infinite atmosphere with a phase function given by equation (29) is necessary. In anticipation of testing a number of models, with various combinations of $\tilde{\omega}_{o_{eff}}$, x_1, and x_2, and in light of the cumbersome nature of the Hansen doubling routine, an analytic solution to the radiative transfer problem was derived. The derivation is presented in the Appendix. The integral equations which result in the derivation require numerical solution, but the software uses only 25% of the computing time and cost necessary for the doubling program and is much easier to use.

At a given wavelength, there are three unknown parameters in this model: b, $\tilde{\omega}_o'$, and x. The calculations may be simplified if the extinction coefficient of the Euler scattering particles is taken to be independent of wavelength; in this case, the dependence of b on wavelength is predictable due to the λ^{-4} dependence of Rayleigh optical depth and b is given by equation (23). As in the previous model, $\tilde{\omega}_{o_{eff}}$ will be assumed to be equal to the values depicted in Figure 8. One needs only to specify the value of b at one wavelength, say 4115Å, and the value of $\tilde{\omega}_{o_{eff}}$ and b at any wavelength will determine the single scattering albedo of the particles. The asymmetry parameter of the particles is constrained by the shape of the limb-darkening curves. Thus, the data may be used to determine two of the three unknown parameters and the only free parameter is the value of b at one wavelength. This reference wavelength is chosen

to be 4115Å. The data exclude a value of b_{4115} larger than 0.892, since this would imply a negative value of $\tilde{\omega}_o'$ for the particles at this wavelength. (Actually, a value as high as 0.904 for b_{4115} is allowed by the 2σ error bars on $\tilde{\omega}_o$ at 4115Å, but for the purposes of this discussion, the nominal value will be assumed.) If b_{4115} is permitted to assume values below this upper limit, a greater fraction of the backscattering observed at this wavelength must be attributed to the particles. However, since the goal is to investigate whether it is possible for the particles to be forward scattering without requiring an enhanced backscatter lobe, the calculations need only be performed for the extreme case in which $b_{4115} = 0.892$. Table VIII shows the required values of $\tilde{\omega}_o'$ for the Euler scattering particles as a function of wavelength, along with the values of b and x_2, which do not depend on the value of x adopted by the Euler particles. Also shown are the values of x_1 for three models, which assume, respectively, that the Euler particles have x = 0, 0.5, and 1. It may be seen that the required dependence of $\tilde{\omega}_o'$ on wavelength is rather extreme in the blue. If b_{4115} is allowed to adopt values < 0.892, the behavior of $\tilde{\omega}_o$ with wavelength need not be so severe, but the Euler particles will have to be more backscattering to compensate for the reduced Rayleigh optical depth.

The limb structure of models in which $b_{4115} = 0.892$ and the cloud particles scatter according to the Euler phase functions with x = 0, x = 0.5, and x = 1 were parameterized with the Euler scattering model to

TABLE VIII

Values of b, $\tilde{\omega}_o'$, x_1, and x_2 vs. λ for gas + Euler scattering cloud models assuming $b_{4115} = 0.892$.

Model 1: Euler scattering particles, x = 0

Model 2: Euler scattering particles, x = 0.5

Model 3: Euler scattering particles, x = 1

λ	b	$\tilde{\omega}_o'$	x_2	x_1 (Model 1)	x_1 (Model 2)	x_1 (Model 3)
4115Å	0.892	0	0.500	0	0	0
4865Å	0.809	0.812	0.420	0	0.080	0.161
5460Å	0.727	0.901	0.374	0	0.126	0.253
5810Å	0.675	0.917	0.347	0	0.153	0.306
7440Å	0.436	0.984	0.220	0	0.280	0.560
8290Å	0.334	0.985	0.169	0	0.331	0.663

permit direct comparisons of the effective Euler asymmetry parameters of the models with the values determined from the actual data (Figure 9). This comparison is shown in Figure 18, in which smooth curves are plotted through the values determined for each of the six wavelength channels. This figure indicates that, with the exception of 4865Å, a model assuming Rayleigh scattering gas plus Euler scattering particles with x between 0 and 0.5 gives a reasonable fit to the data.

Figure 14a of the preceding chapter shows a predominantly forward scattering phase function with a small backscattering lobe (phase function "b" in this figure) which yields full phase limb-darkening consistent with a slightly positive Euler asymmetry parameter (x = 0.09), and a forward scattering phase function with no backscatter lobe (phase function "a"), which requires a highly positive value of the Euler asymmetry parameter to approximate the full phase limb-darkening. The work of Zerull and Giese (1974) and Zerull (1976) indicates that the scattering phase functions of nonspherical particles are even more skewed toward forward scattering than phase function "a" of Figure 14a, so that an approximation to the limb-darkening of an atmosphere composed of such particles using the Euler scattering model would require x = 1; however, this model would probably be a poor approximation in that the shape of the Euler single scattering phase function would be far too gentle. A model in which Euler particles with x = 1 are mixed with Rayleigh scattering gas becomes too forward scattering in the red, as may be seen in Figure 18. Thus,

Figure 18. Comparison of the effective Euler asymmetry parameter, x, determined from parameterizing the limb-darkening of gas + cloud models in which the particles scatter according to the Euler phase function $p(\cos\theta) = \tilde{\omega}_o' (1 + x \cos\theta)$. Three cases are considered; in the first, the Euler particles adopt a wavelength independent value of x = 0 (i.e., the particles scatter isotropically); in the second, x = 0.5; and in the third, x = 1. The wavelength dependence of the limb-darkening is primarily governed by the λ^{-4} dependence of the optical depth of the Rayleigh scattering gas. A model which includes gas + Rayleigh scattering "dust" + forward scattering cloud particles is also shown and compared with the Euler asymmetry parameters determined from the vidicon measurements. None of the models fit the data at 4865Å, and the reason for the extreme back-scattering determined at this wavelength is not understood.

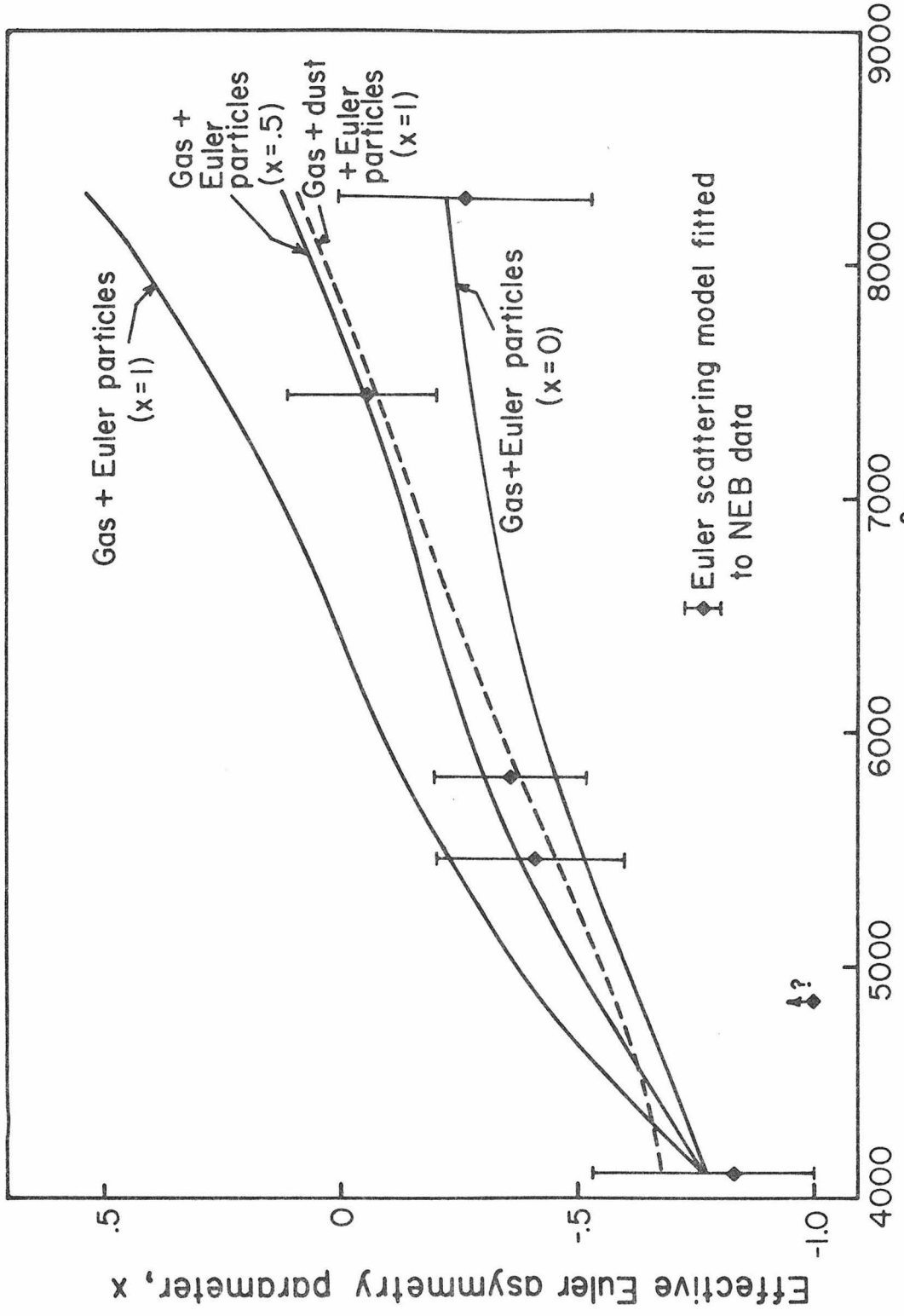
Gas + Euler particles (x=1)
Gas + Euler particles (x=.5)
Gas + dust + Euler particles (x=1)
Gas+Euler particles (x=0)
Euler scattering model fitted to NEB data
Effective Euler asymmetry parameter, x
Wavelength (Å)
.5
0
-.5
-1.0
4000
5000
6000
7000
8000
9000

Fig. 18

if one requires highly forward scattering cloud particles, this model must be ruled out.

It is useful to summarize the findings so far. Compared with the data, pure Rayleigh scattering atmospheres are too backscattering at all wavelengths, particularly in the red, although a nonconservative semi-infinite Rayleigh scattering atmosphere can reproduce the limb-darkening and reflectivity if an overlying non-scattering "cloud" of variable optical depth is assumed. The increase in single scattering albedo from the blue to the red cannot be predicted by the λ^{-4} dependence of the optical depth of Rayleigh scatterers which are mixed with other particles unless the single scattering albedo of one or both constituents is allowed to vary with wavelength. Finally, a mixture of particles with conservative Rayleigh scattering gas requires an extreme variation of the single scattering albedo of the particles with wavelength and becomes too forward scattering in the red if one assumes that the particles do not appreciably backscatter. Since a model with Rayleigh scattering "dust" is too backward scattering in the red, whereas a model with irregularly shaped particles is too forward scattering in this wavelength region, the next logical step is consideration of a model which combines these features; in other words, an atmosphere composed of gas + dust + forward scattering cloud particles.

Defining the parameters b_1 and b_2 such that

$$b_1 = \frac{\tau_{dust}}{\tau_{gas} + \tau_{dust} + \tau_{cloud}} \tag{30a}$$

$$b_2 = \frac{\tau_{gas}}{\tau_{gas} + \tau_{dust} + \tau_{cloud}} \tag{30b}$$

then the effective single scattering phase function of the atmosphere assuming Euler scattering particles is

$$\begin{aligned} p(\cos\theta) &= b_1 \tilde{\omega}_{o_R} [1+\tfrac{1}{2}P_2(\cos\theta)] + b_2 [1+\tfrac{1}{2}P_2(\cos\theta)] \\ &\quad + (1-b_1-b_2)\, \tilde{\omega}_o' [1+x P_1(\cos\theta)] \\ &= \tilde{\omega}_{o_{eff}} \left\{ 1+ \frac{(1-b_1-b_2)\, \tilde{\omega}_o' x}{\tilde{\omega}_{o_{eff}}} P_1(\cos\theta) + \right. \\ &\quad \left. + \frac{\frac{1}{2}(b_1 \tilde{\omega}_{o_R} + b_2)}{\tilde{\omega}_{o_{eff}}} P_2(\cos\theta) \right\} \end{aligned} \tag{30}$$

where $\tilde{\omega}_{o_{eff}} = [b_1 \tilde{\omega}_{o_R} + b_2 + (1-b_1-b_2)\, \tilde{\omega}_o']$ and $\tilde{\omega}_{o_R}$ and $\tilde{\omega}_o'$ are the single scattering albedos of the Rayleigh scattering dust and the Euler scattering particles, respectively. It is not actually necessary to separate the Rayleigh scattering contributions of the gas and dust, since the phase functions are identical and the mixture scatters with an effective single scattering albedo intermediate between

that of the dust ($\tilde{\omega}_{o_R}$) and that of the gas (unity). However, later discussion will show that for the purpose of determining the effective depth of penetration of solar photons it is useful to separate explicitly τ_{gas} and τ_{dust}, since the former may be readily calculated in an absolute sense for a given composition of atmospheric gases. Since the scattering calculations are sensitive only to the relative ratios τ_{dust}/τ_{gas} and τ_{cloud}/τ_{gas}, it is useful to retain some method of determining absolute abundances. The calculations which follow will demonstrate that the gas + dust + cloud model not only reproduces the jovian limb structure observations but yields an absolute gas abundance consistent with independent spectroscopic results.

The gas + dust + cloud model has a number of free parameters, but may be simplified if it is assumed that the particles are white (as are ice particles in the visible) with $\tilde{\omega}_o' = 1$ independent of wavelength, and are forward scattering with x = 1 (again independent of wavelength). The assumption that $\tilde{\omega}_o' = 1$ means that $\tilde{\omega}_{o_{eff}} = b_1\tilde{\omega}_{o_R} + 1-b_1 = 1 + b_1 \cdot (\tilde{\omega}_{o_R} - 1)$ such that taking the measured values of single scattering albedo to be equal to $\tilde{\omega}_{o_{eff}}$ results in determination of $\tilde{\omega}_{o_R}$ once b_1 is specified at a given wavelength. Nevertheless, there is still considerable leeway in the values that may be adopted by b_1 and b_2. The purpose of this discussion, therefore, will not be to derive an optimal set of model parameters, but merely to demonstrate the capabilities of the model by means of a numerical example. Making use of the λ^{-4} dependence of τ_{gas} and τ_{dust} and assuming τ_{cloud}

is independent of wavelength, the only parameters which need to be specified are τ_{dust}/τ_{gas} (which is wavelength independent) and τ_{cloud}/τ_{gas} at a particular wavelength. Table IX presents the values of b_1, b_2, $\tilde{\omega}_{o_R}$, x_1 and x_2 which are obtained if it is assumed that $\tau_{dust}/\tau_{gas} = 10$ and $\tau_{cloud}/\tau_{gas} = 0.5$ at 4115Å. The Euler parameterization of the limb-darkening for the model with this choice of parameters was calculated for each of the six wavelength channels and a smooth curve connecting the values of effective asymmetry parameter is plotted in Figure 18. As expected, the model is not as forward scattering as the model in which Euler particles with x = 1 are mixed with Rayleigh scattering gas, due to the inclusion of the backscattering dust. The model is slightly too forward scattering at 8290Å, but this could be remedied by adjusting the relative dust or gas abundances. None of the models considered here has explained the deviation of the asymmetry parameter from a smooth trend at 4865Å. While this deviation may contain significant information regarding the scattering properties of Jupiter's atmosphere, it is felt that this observation should be verified before models are engineered to match the apparent anomaly.

Since the model with $\tau_{dust}/\tau_{gas} = 10$ and $\tau_{cloud}/\tau_{gas} = 0.5$ at 4115Å gives a reasonable fit to the observed jovian limb structure data, it is useful to mention the implications of these relative abundances with respect to the levels to which solar photons penetrate the atmosphere. The scattering coefficient for Rayleigh scattering in a gas is given by

TABLE IX

Values of b_1, b_2, $\tilde{\omega}_{o_R}$, x_1 and x_2 which are obtained for the gas + dust + forward scattering cloud model assuming $\tau_{dust}/\tau_{gas} = 10$ and $\tau_{cloud}/\tau_{gas} = 0.5$ at 4115Å.

λ	b_1	b_2	$\tilde{\omega}_{o_R}$	x_1	x_2
4115Å	0.870	0.087	0.876	0.048	0.476
4865Å	0.835	0.084	0.957	0.084	0.458
5460Å	0.797	0.080	0.966	0.126	0.437
5810Å	0.770	0.077	0.965	0.157	0.435
7440Å	0.612	0.061	0.985	0.330	0.335
8290Å	0.520	0.052	0.981	0.432	0.284

$$\kappa = \frac{8\pi^3}{3} \frac{(n^2-1)^2 m}{\lambda^4 \rho^2} \tag{32}$$

(Chandrasekhar, 1960), where n = refractive index of the medium, ρ = density, and m = mass/particle. Using the Lorentz-Lorenz relation, which states that

$$\rho_o \frac{n^2 - 1}{n^2 + 2} = \rho \frac{n_o^2 - 1}{n_o^2 + 2} \tag{33}$$

where ρ_o and n_o are the density and refractive index of the gas at some standard temperature and pressure, and n is the refractive index at density ρ, and letting n = 1 + N, where N<<1 for gases, one obtains by substitution:

$$\kappa = \frac{32\pi^3}{3\lambda^4} \frac{N_o^2 m}{\rho_o^2} \tag{34}$$

which implies that κ is independent of density and thus does not vary with height in an atmosphere. The molecular scattering optical depth may be written

$$\tau_{gas} = \kappa \int_z^\infty \rho dz \quad . \tag{35}$$

Assuming hydrostatic equilibrium, the ambient pressure, p, is equal to $\int_z^\infty \rho g dz$, so that $\tau_{gas} = \kappa p/g$, where g is the acceleration of gravity = 2587 cm/sec^2 for Jupiter. Since κ exhibits a λ^{-4} dependence, one may

write $\tau_{gas} = cp\,\lambda^{-4}$. Using the relevant values of refractive index and density of hydrogen gas at STP (Handbook of Chemistry and Physics, 1972), $c = 1.045 \times 10^{-24}$ cm^5 sec^2/g.

The H_2 4-0 S(1) quadrupole line, studied by Cochran et al. (1976) and others, is a narrow feature (equivalent width $\sim$ 8 mÅ) near 6368Å. Using the value $\tau_{dust}/\tau_{gas} = 10$ and $\tau_{cloud}/\tau_{gas} = 2.87$ at 6368Å [$= 0.5 \times (6368/4115)^4$], $\tau_{total} = \tau_{gas} + \tau_{dust} + \tau_{cloud} = 13.87 \cdot \tau_{gas}$ at 6368Å. Thus, unit optical depth for 6368Å photons is reached when $\tau_{gas} = 1/13.87 = 0.072$. Making use of the expression for τ_{gas} derived above, this corresponds to a pressure level of 1.13 bars. The abundance of H_2 above this level may be calculated from

$$\alpha_{H_2} = \frac{pN_A}{gm'L} \tag{36}$$

where N_A = Avogadro's number, m' = molecular weight of H_2, and L = Loschmidts's number. The abundance of H_2 above the 1.13 bar level turns out to be roughly 50 km-amagat, which may be compared to Fink and Belton's (1969) estimate of 67 ± 17 km-amagat from the quadrupole spectrum assuming a reflecting layer model and Cochran's (1976) total vertical abundance of 62 km-amagat in his two-cloud model. Note, however, that the foregoing choice of model parameters is not unique, and different choices for τ_{dust}/τ_{gas} and τ_{cloud}/τ_{gas} can yield gas abundances significantly different from the value of 50 km-amagat obtained above while still resulting in good fits to the limb structure data. Therefore, this calculation demonstrates the need for a

combination of spectroscopic data with the photometric measurements in order to constrain fully the relative abundances of scatterers inferred from the limb-darkening observations. From the standpoint of center-to-limb equivalent width variations, which indicate that homogeneous scattering models are untenable, the models considered here are somewhat academic. However, it is unlikely that the basic conclusions regarding the types of scatterers which must be present would change as a result of considering more sophisticated, vertically inhomogeneous models, although to some degree the quantitative aspects of such models could differ from those which assume vertical homogeneity.

The remainder of this section will be concerned with the scattering properties of the South Tropical Zone. Reference to Figures 8, 9, and 10 indicates several points of contrast between the STrZ and NEB: 1) the STrZ is always brighter than the NEB; 2) the STrZ is always less backward scattering than the NEB; and 3) the variation with wavelength of the slopes of the limb-darkening profiles is more marked in the NEB than in the STrZ. The first two points are qualitatively consistent with an STrZ model which is similar to the gas + dust + cloud model devised for the NEB, but with a lesser abundance of low albedo backscattering dust, or a greater abundance of high albedo forward scattering cloud particles. However, Figure 9 shows that the STrZ data are consistent with isotropic scattering longward of 5000Å, with little variation in effective asymmetry parameter from

5460 to 8290Å. The λ^{-4} dependence of Rayleigh optical depth may therefore result in models in which the shape of the limb-darkening changes by an amount greater than permitted by the data, particularly if the cloud particles are assumed to be highly forward scattering. This may be demonstrated by returning to Figure 18, which compares several models to the NEB data; the gas + dust + cloud model is slightly more forward scattering than the data imply at 8290Å, and the gas + cloud model with x = 1 is certainly ruled out. Such models will be less adequate for the STrZ, which does not show as great a spectral variation in asymmetry parameter as the NEB. Therefore, lowering the abundance of dust or increasing the cloud particle abundance will result in a greater spectral variation in the slope of limb-darkening profiles in the STrZ relative to the NEB, rather than less, as required by point (3) above. If a gas + dust + cloud model is to work, then, either the cloud particles must be considerably more backscattering than the Euler phase function with x = 1, yielding a gradual change in effective asymmetry parameter with wavelength, or the optical depth of the dust particles must show a dependence on wavelength that is more gradual than λ^{-4}. With respect to the first suggestion, it has been argued that relaxation of the forward scattering constraint and inclusion of an enhanced backscattering lobe in the cloud particle single scattering phase functions is not consistent with the assumption of irregularly shaped particles, so the relative wavelength independence of the STrZ limb-darkening over a significant portion of the visible

spectrum presents something of a dilemma. With respect to the second hypothesis regarding scatterers with nearly wavelength independent optical depth, the observations require such particles to be back-scattering if the model also includes cloud particles (e.g., ice crystals) which are forward scattering. Measurements of the jovian limb-darkening in the near-infrared, where the Rayleigh scattering optical depth is small, would lead to better insight into the intrinsic scattering properties of the cloud particles. Vertically inhomogeneous models, with distinct, rather than mixed, gas, dust, and cloud layers should be investigated to determine whether they predict different, and preferably more gradual, spectral variations in the limb-darkening of models which include Rayleigh scatterers and forward scattering clouds. In any event, it is hoped that these remarks indicate the utility of measurements of the center-to-limb variation in intensity across isolated regions in a planetary atmosphere, and demonstrate that with additional input regarding vertical structure, more extensive wavelength coverage, and more sophisticated software, it will be possible to begin to resolve some key issues and acquire a better understanding of the nature of Jupiter's clouds.

Chapter 8

CONCLUSIONS

> When you have eliminated the impossible,
> whatever remains, however improbable,
> must be the truth.
>
> - Sir Arthur Conan Doyle
> "The Sign of the Four,"
> from The Adventures of
> Sherlock Holmes

Spectrally and spatially resolved measurements of center-to-limb variations in reflectivity provide useful constraints with regard to the proportions and distribution of clouds, dust and gas in Jupiter's belts and zones. Simple atmospheric models indicate that the spectral dependence of the limb structure in the North Equatorial Belt is explainable as a mixture of gas, Rayleigh scattering dust, and forward scattering cloud particles. The South Tropical Zone is brighter and more forward scattering than the NEB, which is consistent with a lower abundance of dust or higher abundance of cloud particles relative to the North Equatorial Belt, but there is evidence that this type of model may run into quantitative difficulties, due to the relative spectral invariance of the scattering properties of the STrZ compared with the NEB.

Extension of the work presented here can take several forms. Imaging in the ultraviolet between 3000 and 4000Å will provide valuable information regarding the contribution of Rayleigh scattering to the atmospheric reflection properties; by the same token, imaging at wavelengths in the near-infrared, where the Rayleigh optical depths

are small, will lead to greater insight into the scattering properties of the cloud particles. Better spatial coverage, with particular emphasis on regions close to the planetary limb, will lead to significant improvements in scattering models, since the oblique viewing geometries are the most diagnostic in discriminating among a set of alternatives. For example, Figure 19 shows three scattering models which all fit the 8290Å limb structure data equally well for viewing angle cosines greater than 0.4. The first model assumes pure Euler scattering with $\tilde{\omega}_o = 0.990$, $x = -0.26$; the second is a semi-infinite Rayleigh scattering atmosphere with $\tilde{\omega}_o = 0.990$, above which lies a completely absorbing layer with optical depth $\tau = 0.021$; and the third is a homogeneous mixture of conservative Rayleigh scattering gas and isotropically scattering particles with $\tilde{\omega}_o = 0.985$ and with the ratio of optical depths, $\tau_{particle}/\tau_{gas} = 1.99$. The models have been extended to values of μ below 0.4, and it may be seen that at $\mu = 0.1$, the contrast between the reflectivity of the second model and the first is 22%, while the contrast between the third model and the first is only 5%. It would be virtually impossible to distinguish between the models from ground-based measurements, even with better than 1% relative photometry, due to the difficulty in deconvolution of atmospheric seeing. While "speckle" techniques or imaging from Space Telescope would eliminate the smearing problem, the presence of bright and dark regions within a given belt or zone may present considerable problems when discrimination on the order of a few percent is required.

Figure 19. - Limb-darkening of three models which fit the 8290Å North Equatorial Belt limb structure data equally well for values of $\mu > 0.4$. The first is a semi-infinite Euler scattering model with $\tilde{\omega}_o = 0.99$, $x = -0.26$; the second is a semi-infinite Rayleigh scattering atmosphere with $\tilde{\omega}_o = 0.99$, above which lies a pure absorbing layer with optical depth $\tau = 0.021$; and the third is a semi-infinite homogeneous mixture of gas plus isotropically scattering particles with $\tilde{\omega}_o = 0.985$ and with the ratio of optical depths $\tau_{particle}/\tau_{gas} = 1.99$. The models are extended to values of μ below 0.4 in order to determine whether photometry close to the planetary limbs can distinguish among them.

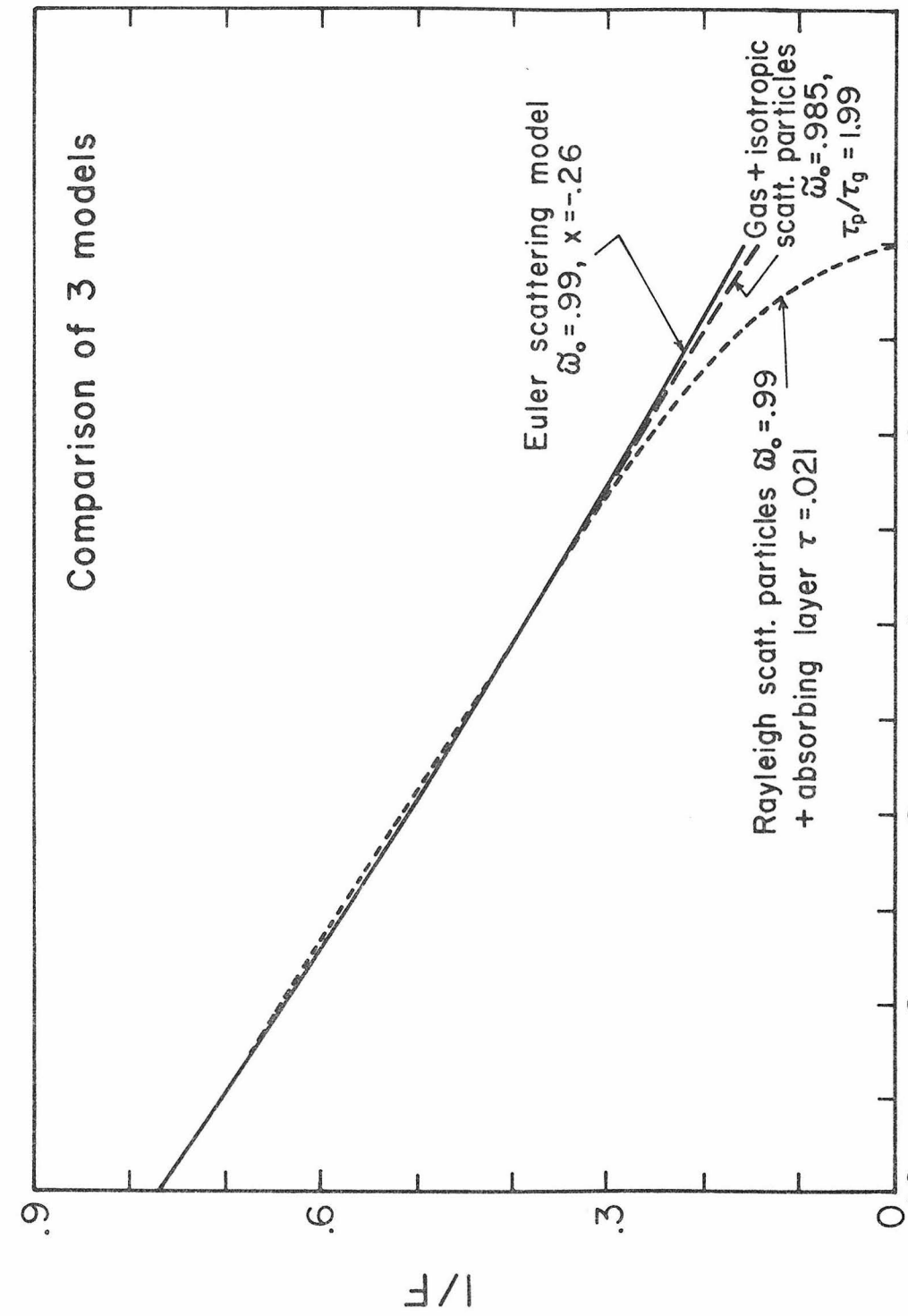
Comparison of 3 models
Euler scattering model
$\tilde{\omega}_o$=.99, x=-.26
Gas + isotropic
scatt. particles
$\tilde{\omega}_o$=.985,
τ_p/τ_g = 1.99
Rayleigh scatt. particles $\tilde{\omega}_o$=.99
+ absorbing layer τ =.021
I/F
μ
0
.3
.6
.9
1.0
.8
.6
.4
.2
0

Fig. 19

The effect of such inhomogeneities may be diminished if a number of images are taken and a single spot is followed as Jupiter rotates; alternatively, images taken at different rotational phases could be averaged together to reduce statistically the lateral variations due to local features on the disk. In the first case, consistent determination of the relevant geometric variables from one image to another could present substantial difficulties, while failure to do so would introduce considerable errors into the data, particularly near the limbs. This procedure would also require the procurement of a large number of consecutive images (perhaps on the order of 20 or 30) and the data handling and reduction capabilities would have to be appropriately designed. With regard to the second procedure of averaging images, it has been pointed out that the RMS residuals between the Euler scattering models and the actual data are on the order of 2-3 times the 1σ uncertainty in the measurements. If the residuals are due to lateral inhomogeneities, then roughly 10 uncorrelated images would need to be averaged to reduce such variations to the level of the noise; a greater number would be required if the relative photometry is better than 1.5-2.0% as reported here. If this averaging procedure did not reduce the RMS residuals, this could be construed as evidence of a real failure of the Euler scattering model in parameterizing the data. This result would imply the necessity of a three-term function to parameterize the data, leading to an added dimension in the discrimination of models of the jovian atmospheric structure.

Combined with vertical structure information obtained from spatially resolved spectroscopic and infrared thermal sounding observations, and photometry and polarimetry at high phase angles from the Pioneer and Voyager flybys, such data will provide significant information on the relative abundances and optical properties of the gas, dust and clouds in the jovian upper atmosphere. Such investigations need not be limited to the atmosphere of Jupiter, however, and studies of the limb structure of Saturn and Uranus, particularly with the high spatial resolution imaging capability of Space Telescope and data returned by planetary probes, promise numerous opportunities for comparative planetology of the objects in the outer solar system.

APPENDIX

In this appendix a general form of the law of diffuse reflection for a semi-infinite homogeneous atmosphere is derived, in which the single scattering phase function is of the form

$$p(\cos\theta) = \tilde{\omega}_o\{1 + x_1 P_1(\cos\theta) + x_2 P_2(\cos\theta)\} \qquad (1)$$

where $\tilde{\omega}_o$ is the single scattering albedo and P_n are Legendre polynomials of order n. Special cases of this phase function are Euler scattering, where $x_2 = 0$; and Rayleigh scattering, where $x_1 = 0$, $x_2 = 1/2$. This problem has been solved exactly by Chandrasekhar (1960) for the special case in which $\tilde{\omega}_o = 1$. The solution for nonconservative cases is somewhat more involved, since certain terms in the derivation do not reduce to simple expressions. Chandrasekhar presented the solution and a partial outline of the derivation for the conservative case. However, it is considerably more useful to solve the radiative transfer problem in the more general form, particularly since it presents the opportunity to consider a substantially larger variety of model atmospheres. The derivation which follows and the software which was developed present a convenient means for calculating diffuse reflection functions for the purpose of comparing such functions with actual observations.

In the following derivation, the model atmosphere is assumed to be semi-infinite, homogeneous and plane-parallel. The geometric variables are μ, the cosine of the angle between the local normal and the direction to the observer; μ_o, the cosine of the angle between

the local normal and direction to the illuminating source; and $(\varphi - \varphi_o)$, the azimuth difference between the two vectors which are at angles arccos μ and arccos μ_o to the local normal. In the case of scattering by a single particle, the dummy variables μ', μ'' and φ', φ'' alternately replace μ_o and φ_o. The atmosphere is assumed to be illuminated from above by a flux πF.

The solution is expressed in terms of a surface brightness $I(\mu,\mu_o,\varphi - \varphi_o)$, and the object shall be to derive a function S in which

$$I(\mu,\mu_o,\varphi - \varphi_o) = \frac{F}{4\mu} S(\mu,\mu_o,\varphi - \varphi_o) \tag{2}$$

and $S(\mu,\mu_o,\varphi - \varphi_o) = S(\mu_o,\mu,\varphi_o - \varphi)$. Chandrasekhar has shown that a single scattering phase function composed of n Legendre polynomials will yield a function S which may be expanded into a cosine series in $(\varphi - \varphi_o)$, with n distinct functions which depend on μ and μ_o alone. From the equation of radiative transfer, assuming a semi-infinite atmosphere, he has derived a useful integral equation which relates S to the single scattering phase function p. Using the law of cosines, $\cos\theta = \mu\mu' + (1 - \mu^2)^{\frac{1}{2}} (1 - \mu'^2)^{\frac{1}{2}} \cos(\varphi - \varphi')$, such that one may let $p = p(\mu,\mu',\varphi - \varphi')$, this integral relation is:

$$\left(\frac{1}{\mu} + \frac{1}{\mu_o}\right) S(\mu,\mu_o,\varphi - \varphi_o) = p(\mu, -\mu_o,\varphi - \varphi_o)$$

$$+ \frac{1}{4\pi} \int_0^1 \int_0^{2\pi} p(\mu,\mu'',\varphi - \varphi'') S(\mu'',\mu_o,\varphi'' - \varphi_o) \frac{d\mu''}{\mu''} d\varphi''$$

$$+ \frac{1}{4\pi} \int_0^1 \int_0^{2\pi} p(\mu',\mu_o,\varphi' - \varphi') \frac{d\mu'}{\mu'} d\varphi'$$

$$+ \frac{1}{16\pi^2} \int_0^1 \int_0^{2\pi} \int_0^1 \int_0^{2\pi} S(\mu,\mu',\varphi-\varphi')\ p(-\mu',\mu'',\varphi'-\varphi'')$$

$$\cdot\ S(\mu'',\mu_o,\varphi''-\varphi_o)\ \frac{d\mu'}{\mu'}\ d\varphi'\ \frac{d\mu''}{\mu''}\ d\varphi'' \quad . \tag{3}$$

Thus, given the analytic form of p, the problem is to derive an expression for S, which may then be related to reflected intensity by equation (2).

The first step in the derivation involves the expansion of the single scattering phase function $p(\cos\theta)$ in terms of the local variables μ, μ', and $\cos(\varphi-\varphi')$. By the law of cosines:

$$P_1(\cos\theta) = \cos\theta + \mu\mu' + (1-\mu^2)^{\frac{1}{2}}\ (1-\mu'^2)^{\frac{1}{2}} \cos\ (\varphi-\varphi') \tag{4}$$

$$P_2(\cos\theta) = \tfrac{1}{2}(3\cos^2\theta - 1) = \tfrac{1}{4} - \tfrac{3}{4}\mu^2 - \tfrac{3}{4}\mu'^2 + \tfrac{9}{4}\mu^2\mu'^2$$

$$+ 3\mu\mu'(1-\mu^2)^{\frac{1}{2}}(1-\mu'^2)^{\frac{1}{2}} \cos(\varphi-\varphi')$$

$$+ \tfrac{3}{4}(1-\mu^2)(1-\mu'^2) \cos\ 2(\varphi-\varphi') . \tag{5}$$

Therefore,

$$p(\cos\theta) = p(\mu,\mu',\varphi-\varphi') = \tilde{\omega}_o\Big\{\Big[1 + x_1\mu\mu' + \frac{x_2}{4}\ (1-3\mu^2)(1-3\mu'^2)\Big]$$

$$+ \Big[(x_1 + 3x_2\mu\mu')(1-\mu^2)^{\frac{1}{2}}(1-\mu'^2)^{\frac{1}{2}}\Big]\cos(\varphi-\varphi')$$

$$+ \Big[\frac{3}{4}\ x_2(1-\mu^2)(1-\mu'^2)\Big] \cos\ 2(\varphi-\varphi')\Big\}. \tag{6}$$

This suggests the following form for S:

$$S(\mu,\mu_o,\varphi-\varphi_o) = \tilde{\omega}_o\ \Big[S^{(o)}(\mu,\mu_o) + (1-\mu^2)^{\frac{1}{2}}(1-\mu_o^2)^{\frac{1}{2}}$$

$$\cdot\ S^{(1)}(\mu,\mu_o) \cos\ (\varphi-\varphi_o)\ +$$

$$+ \frac{3}{4} x_2 (1 - \mu^2)(1 - \mu_o^2)\, S^{(2)}(\mu,\mu_o) \cos 2(\varphi - \varphi_o)\Big] . \tag{7}$$

The simplest term to solve for is $S^{(2)}$. Substituting the expression for p in equation (6) and the expression for S in equation (7) into equation (3), multiplying both sides by $\cos 2(\varphi - \varphi_o)\, d\varphi$ and integrating over 2π, and making use of the orthogonality relations

$$\frac{1}{2\pi} \int_o^{2\pi} \cos m(\varphi' - \varphi_o) \cos n(\varphi - \varphi')\, d\varphi'$$

$$= 0 \qquad m \neq n \tag{8a}$$

$$= \frac{1}{2} \cos m(\varphi - \varphi_o) \qquad m = n \neq 0 \tag{8b}$$

$$= 1 \qquad m = n = 0 \tag{8c}$$

then the following integral expression for $S^{(2)}$ emerges:

$$\left(\frac{1}{\mu} + \frac{1}{\mu_o}\right) S^{(2)}(\mu,\mu_o) = 1 + \frac{3}{16} \tilde{\omega}_o x_2 \int_o^1 (1 - \mu''^2)^2\, S^{(2)}(\mu'',\mu_o)\, \frac{d\mu''}{\mu''}$$

$$+ \frac{3}{16} \tilde{\omega}_o x_2 \int_o^1 (1 - \mu'^2)^2\, S^{(2)}(\mu,\mu')\, \frac{d\mu'}{\mu'}$$

$$+ \frac{9}{256} \tilde{\omega}_o^2 x_2^2 \int_o^1 \int_o^1 S^{(2)}(\mu,\mu')\, (1 - \mu'^2)^2 (1 - \mu''^2)^2$$

$$\cdot\, S^{(2)}(\mu'',\mu_o)\, \frac{d\mu''}{\mu''}\, \frac{d\mu'}{\mu'}$$

$$= \left\{1 + \frac{3}{16} \tilde{\omega}_o x_2 \int_o^1 (1 - \mu''^2)^2\, S^{(2)}(\mu'',\mu_o)\, \frac{d\mu''}{\mu''}\right\} \cdot$$

$$\cdot \left\{ 1 + \frac{3}{16} \tilde{\omega}_o \, x_2 \int_o^1 (1 - \mu'^2)^2 \, S^{(2)}(\mu,\mu') \, \frac{d\mu'}{\mu'} \right\}$$

$$= H^{(2)}(\mu_o) \, H^{(2)}(\mu) \tag{9}$$

from which it may be shown that

$$H^{(2)}(\mu) = 1 + \mu H^{(2)}(\mu) \int_o^1 \frac{\frac{3}{16} \tilde{\omega}_o \, x_2 (1 - \mu'^2)^2}{\mu + \mu'} \, H^{(2)}(\mu') \, d\mu' \quad . \tag{10}$$

Chandrasekhar has defined a class of functions called H-functions defined by integral equations of the form

$$H(\mu) = 1 + \mu H(\mu) \int_o^1 \frac{\Psi(\mu')}{\mu + \mu'} \, H(\mu') \, d\mu' \tag{11}$$

where $\Psi(\mu')$ is called the characteristic function and is any even polynomial in μ' such that $\int_o^1 \Psi(\mu') \, d\mu' \leq \frac{1}{2}$. H-functions are ubiquitous in radiative transfer problems with semi-infinite atmospheres, and it may be seen that the function defined in equation (10) is a specific case of the general form, with $\Psi(\mu') = \frac{3}{16} \tilde{\omega}_o x_2 (1-\mu'^2)^2$. Letting $\tilde{\omega}_o = 1$, this expression is identical to the one derived by Chandrasekhar for the conservative case.

The next term to be derived is $S^{(1)}$. Substituting the expressions for p and S in equations (6) and (7) into equation (3), multiplying both sides by $\cos(\varphi - \varphi_o)d\varphi$ and integrating over 2π, one gets

$$\left(\frac{1}{\mu}+\frac{1}{\mu_o}\right) S^{(1)}(\mu,\mu_o) = x_1 - 3x_2\,\mu\mu_o + \frac{\tilde{\omega}_o}{4}\int_o^1 (x_1+3x_2\mu\mu'')\cdot$$

$$\cdot\,(1-\mu''^2)\,S^{(1)}(\mu'',\mu_o)\,\frac{d\mu''}{\mu''}$$

$$+\frac{\tilde{\omega}_o}{4}\int_o^1 (x_1+3x_2\,\mu'\mu_o)(1-\mu'^2)\,S^{(1)}(\mu',\mu)\,\frac{d\mu'}{\mu'}$$

$$+\frac{\tilde{\omega}_o^2}{16}\int_o^1\int_o^1 (1-\mu''^2)(1-\mu'^2)\,S^{(1)}(\mu,\mu')\cdot$$

$$\cdot\,(x_1-3x_2\,\mu'\mu'')\,S^{(1)}(\mu'',\mu_o)\,\frac{d\mu'}{\mu'}\,\frac{d\mu''}{\mu''}$$

$$= x_1\left\{1+\frac{\tilde{\omega}_o}{4}\int_o^1 (1-\mu'^2)\,S^{(1)}(\mu,\mu')\,\frac{d\mu'}{\mu'}\right\}$$

$$\cdot\left\{1+\frac{\tilde{\omega}_o}{4}\int_o^1 (1-\mu''^2)\,S^{(1)}(\mu'',\mu_o)\,\frac{d\mu''}{\mu''}\right\}$$

$$-3x_2\left\{\mu-\frac{\tilde{\omega}_o}{4}\int_o^1 \mu'(1-\mu'^2)\,S^{(1)}(\mu,\mu')\,\frac{d\mu'}{\mu'}\right\}$$

$$\cdot\left\{\mu_o-\frac{\tilde{\omega}_o}{4}\int_o^1 \mu''(1-\mu''^2)\,S^{(1)}(\mu'',\mu_o)\,\frac{d\mu''}{\mu''}\right\}$$

$$= x_1\beta(\mu)\,\beta(\mu_o) - 3x_2\,\sigma(\mu)\,\sigma(\mu_o)\ . \qquad (12)$$

It was shown by Chandrasekhar that in the case $\tilde{\omega}_o = 1$,

$$\left(\frac{1}{\mu}+\frac{1}{\mu_o}\right) S^{(1)}(\mu,\mu_o) = H^{(1)}(\mu)\,H^{(1)}(\mu_o)$$

$$\cdot\left\{x_1 - c(\mu+\mu_o) - x_2(3-x_1)\,\mu\mu_o\right\} \qquad (13a)$$

where c is a constant and $H^{(1)}$ is a function of the type expressed by equation (11) with the characteristic function $\Psi(\mu') = \frac{1}{4}(1-\mu'^2) \cdot [x_1 + x_2(3-x_1)\mu'^2]$. For the nonconservative case, let it be assumed that

$$\left(\frac{1}{\mu}+\frac{1}{\mu_o}\right) S^{(1)}(\mu,\mu_o) = H^{(1)}(\mu)\, H^{(1)}(\mu_o) \cdot \left\{x_1 - c(\mu+\mu_o) - x_2(3-\tilde{\omega}_o x_1)\mu\mu_o\right\} \qquad (13b)$$

where $H^{(1)}(\mu)$ is now defined in terms of the characteristic function $\Psi(\mu') = \frac{1}{4}\tilde{\omega}_o(1-\mu'^2)[x_1 + x_2(3-\tilde{\omega}_o x_1)\mu'^2]$. It will be seen that these assumptions are necessary to achieve consistency with equation (12). The following discussion demonstrates that equation (13b) is the solution to the problem, and an expression for the constant c is derived.

Before continuing with the discussion, it will be necessary to define the nth moment of the function $H^{(1)}$ by

$$\alpha_n = \int_o^1 \mu'^n H^{(1)}(\mu')\, d\mu' \qquad (14)$$

and to prove two useful lemmas.

Lemma 1. $$\frac{1}{4}\tilde{\omega}_o[x_1 + x_2(3-\tilde{\omega}_o x_1)\mu^2] \int_o^1 \frac{(1-\mu'^2)H^{(1)}(\mu')}{\mu+\mu'}\, d\mu'$$

$$= \frac{H^{(1)}(\mu)-1}{\mu H^{(1)}(\mu)} - \frac{1}{4}\tilde{\omega}_o x_2(3-\tilde{\omega}_o x_1)[(\alpha_1-\alpha_3) - (\alpha_o-\alpha_2)\mu] \,.$$

Proof. $$H^{(1)}(\mu) = 1 + \frac{1}{4}\tilde{\omega}_o\mu\, H^{(1)}(\mu) \cdot \int_o^1 \frac{[x_1 + x_2(3-\tilde{\omega}_o x_1)\mu'^2](1-\mu'^2)}{\mu+\mu'} H^{(1)}(\mu')\, d\mu' \qquad (15)$$

by definition. Thus

$$\frac{1}{4}\tilde{\omega}_o x_1 \int_o^1 \frac{(1-\mu'^2)\, H^{(1)}(\mu')}{\mu+\mu'}\, d\mu' = \frac{H^{(1)}(\mu)-1}{\mu H^{(1)}(\mu)} - \frac{1}{4}\tilde{\omega}_o x_2 (3-\tilde{\omega}_o x_1) \cdot$$

$$\int_o^1 \frac{(1-\mu'^2)\,\mu'^2\, H^{(1)}(\mu')}{\mu+\mu'}\, d\mu' = \frac{H^{(1)}(\mu)-1}{\mu\, H^{(1)}(\mu)} - \frac{1}{4}\tilde{\omega}_o x_2 (3-\tilde{\omega}_o x_1) \cdot$$

$$\int_o^1 (1-\mu'^2)\left[\mu' - \mu + \frac{\mu^2}{\mu+\mu'}\right] H^{(1)}(\mu')\, d\mu' = \frac{H^{(1)}(\mu)-1}{\mu\, H^{(1)}(\mu)}$$

$$- \frac{1}{4}\tilde{\omega}_o x_2 (3-\tilde{\omega}_o x_1)(\alpha_1 - \alpha_3 - \alpha_o\mu + \alpha_2\mu)$$

$$- \frac{1}{4}\tilde{\omega}_o x_2 (3-\tilde{\omega}_o x_1)\,\mu^2 \int_o^1 \frac{(1-\mu'^2)H^{(1)}(\mu')}{\mu+\mu'}\, d\mu' \quad . \qquad (16)$$

Therefore

$$\frac{1}{4}\tilde{\omega}_o\left[x_1 + x_2(3-\tilde{\omega}_o x_1)\mu^2\right] \int_o^1 \frac{(1-\mu'^2)H^{(1)}(\mu')}{\mu+\mu'}\, d\mu'$$

$$= \frac{H^{(1)}(\mu)-1}{\mu\, H^{(1)}(\mu)} - \frac{1}{4}\tilde{\omega}_o x_2\,(3-\tilde{\omega}_o x_1)\left[(\alpha_1-\alpha_3) - (\alpha_o-\alpha_2)\mu\right]$$

Q.E.D.

Lemma 2. $(\alpha_o - \alpha_2) = \frac{2}{3} + \frac{1}{8}\tilde{\omega}_o x_1 (\alpha_o-\alpha_2)^2 + \frac{1}{8}\tilde{\omega}_o x_2 (3-\tilde{\omega}_o x_1)(\alpha_1-\alpha_3)^2$.

Proof. The first step is to derive an expression for α_o. Since Ψ is of the form $\Psi(\mu') = a + b\mu'^2 + c\mu'^4$, $H^{(1)}$ may be written

$$H^{(1)}(\mu) = 1 + \mu H^{(1)}(\mu) \int_o^1 \frac{(a+b\mu'^2+c\mu'^4)\, H^{(1)}(\mu')}{\mu+\mu'}\, d\mu' \quad . \qquad (17)$$

Multiplying both sides by $d\mu$ and integrating from 0 to 1,

$$\int_0^1 H^{(1)}(\mu)\, d\mu = \alpha_o = \int_0^1\int_0^1 \frac{(a + b\mu'^2 + c\mu'^4)\ \mu H^{(1)}(\mu) H^{(1)}(\mu')}{\mu + \mu'}\, d\mu' d\mu. \quad (18)$$

Interchanging the order of integration,

$$\alpha_o = 1 + \int_0^1\int_0^1 \frac{(a + b\mu^2 + c\mu 4)\ \mu' H^{(1)}(\mu')\ H^{(1)}(\mu)}{\mu + \mu'}\, d\mu\, d\mu' \quad . \quad (19)$$

Adding equation (18) to equation (19), making use of the definition of α_n in equation (14), and dividing by 2, one obtains

$$\alpha_o = 1 + \frac{1}{2}a\alpha_o^2 + \frac{1}{2}b\alpha_1^2 + \frac{1}{2}c \int_0^1\int_0^1 \frac{(\mu'^4\mu + \mu^4\mu')}{\mu + \mu'}\, H^{(1)}(\mu)$$

$$\cdot\, H^{(1)}(\mu')\, d\mu\, d\mu' \quad . \quad (20)$$

It may be shown that

$$\frac{\mu'^4\mu + \mu^4\mu'}{\mu + \mu'} = \mu^3\mu' + \mu'^3\mu - \mu^2\mu'^2 \quad . \quad (21)$$

From equations (14), (20) and (21),

$$\alpha_o = 1 + \frac{1}{2}\, a\, \alpha_o^2 + \frac{1}{2}\, b\, \alpha_1^2 + \frac{1}{2}\, c\, (2\alpha_1\alpha_3 - \alpha_2^2) \quad . \quad (22)$$

The next step is to derive an expression for α_2. Multiplying both sides of equation (17) by $\mu^2 d\mu$ and integrating from 0 to 1,

$$\int_0^1 \mu^2 H^{(1)}(\mu)\, d\mu = \alpha_2 = \frac{1}{3} + \int_0^1\int_0^1 \frac{(a + b\mu'^2 + c\mu'^4)\ \mu^3}{\mu + \mu'}$$

$$\cdot\, H^{(1)}(\mu')\ H^{(1)}(\mu)\, d\mu' d\mu \quad .$$

As above, the order of integration is interchanged and the two equations averaged:

$$\alpha_2 = \frac{1}{3} + \frac{1}{2}\, a \int_0^1 \int_0^1 \frac{\mu^3 + \mu'^3}{\mu + \mu'} H^{(1)}(\mu)\, H^{(1)}(\mu')\, d\mu\, d\mu'$$

$$+ \frac{1}{2}\, b\alpha_2^{\,2} + \frac{1}{2}\, c\alpha_3^{\,2} \quad . \tag{23}$$

It may be shown that

$$\frac{\mu^3 + \mu'^3}{\mu + \mu'} = \mu^2 + \mu'^2 - \mu\mu' \quad . \tag{24}$$

Thus, combining equations (14), (23) and (24), one gets

$$\alpha_2 = \frac{1}{3} + \frac{1}{2}\, a\, (2\alpha_2\alpha_o - \alpha_1^{\,2}) + \frac{1}{2} b\alpha_2^{\,2} + \frac{1}{2} c\alpha_3^{\,2} \quad . \tag{25}$$

Subtracting equation (25) from equation (22),

$$(\alpha_o - \alpha_2) = \frac{2}{3} + \frac{1}{2} a[\alpha_o^{\,2} - 2\alpha_2\alpha_o + \alpha_1^{\,2}] + \frac{1}{2} b[\alpha_1^{\,2} - \alpha_2^{\,2}]$$

$$+ \frac{1}{2} c[2\alpha_1\alpha_3 - \alpha_2^{\,2} - \alpha_3^{\,2}] \quad .$$

Making use of the fact that $a = \frac{1}{4}\, \tilde{\omega}_o x_1$; $b = \frac{1}{4}\, \tilde{\omega}_o [x_2(3 - \tilde{\omega}_o x_1) - x_1]$; and $c = -\frac{1}{4}\, \tilde{\omega}_o x_2 (3 - \tilde{\omega}_o x_1)$, and combining like terms:

$$(\alpha_o - \alpha_2) = \frac{2}{3} + \frac{1}{8}\, \tilde{\omega}_o x_1 (\alpha_o - \alpha_2)^2 + \frac{1}{8}\, \tilde{\omega}_o x_2 (3 - \tilde{\omega}_o x_1)(\alpha_1 - \alpha_3)^2$$

Q.E.D.

The next step in the derivation is to derive an expression for $\beta(\mu)$. From equation (12),

$$\beta(\mu) = 1 + \frac{1}{4}\, \tilde{\omega}_o \int_0^1 (1 - \mu'^2)\, S^{(1)}(\mu,\mu')\, \frac{d\mu'}{\mu'} \quad .$$

Using equation (13b) and substituting for $S^{(1)}(\mu,\mu')$,

$$\beta(\mu) = 1 + \frac{1}{4}\tilde{\omega}_o \int_o^1 (1-\mu'^2)\,\frac{\mu}{\mu+\mu'}\,H^{(1)}(\mu)\,H^{(1)}(\mu')\cdot$$

$$\cdot\,\{x_1 - c(\mu+\mu') - x_2(3-\tilde{\omega}_o x_1)\mu\mu'\}\,d\mu'$$

$$= 1 + \frac{1}{4}\tilde{\omega}_o\,\mu\,H^{(1)}(\mu)\int_o^1 (1-\mu'^2)H^{(1)}(\mu')\,\frac{x_1}{\mu+\mu'} - c - \frac{x_2(3-\tilde{\omega}_o x_1)\mu\mu'}{\mu+\mu'}\,d\mu'$$

$$= 1 + \frac{1}{4}\tilde{\omega}_o\mu\,H^{(1)}(\mu)[x_1 + x_2(3-\tilde{\omega}_o x_1)\,\mu^2]\int_o^1 \frac{(1-\mu'^2)H^{(1)}(\mu')}{\mu+\mu'}\,d\mu'$$

$$- \frac{1}{4}\tilde{\omega}_o\mu\,H^{(1)}(\mu)\,[c + x_2(3-\tilde{\omega}_o x_1)\mu]\int_o^1 (1-\mu'^2)\,H^{(1)}(\mu')\,d\mu' \quad .$$

Using equation (14) and Lemma 1,

$$\beta(\mu) = 1 + \mu H^{(1)}(\mu)\left\{\frac{H^{(1)}(\mu)-1}{\mu H^{(1)}(\mu)} - \frac{1}{4}\tilde{\omega}_o x_2(3-\tilde{\omega}_o x_1)[(\alpha_1-\alpha_3)-(\alpha_o-\alpha_2)\mu]\right\}$$

$$- \frac{1}{4}\tilde{\omega}_o\,\mu\,H^{(1)}(\mu)\,[c + x_2(3-\tilde{\omega}_o x_1)\mu](\alpha_o-\alpha_2) \quad .$$

Combining like terms, one obtains

$$\beta(\mu) = H^{(1)}(\mu)\left\{1 - \frac{1}{4}\tilde{\omega}_o x_2(3-\tilde{\omega}_o x_1)(\alpha_1-\alpha_3)\,\mu - \frac{1}{4}\tilde{\omega}_o\,c(\alpha_o-\alpha_2)\mu\right\}$$

$$= H^{(1)}(\mu)\,\{1 - p\mu\} \quad . \qquad (26)$$

Now a relation between $\sigma(\mu)$ and $H^{(1)}(\mu)$ will be derived. Combining the expression for $\sigma(\mu)$ from equation (12) with equation (13b),

$$\sigma(\mu) = \mu - \frac{1}{4}\tilde{\omega}_o\int_o^1 (1-\mu'^2)\,\frac{\mu\mu'}{\mu+\mu'}\,H^{(1)}(\mu)H^{(1)}(\mu')\cdot$$

$$\cdot\,[x_1 - c(\mu+\mu') - x_2(3-\tilde{\omega}_o x_1)\mu\mu']\,d\mu'$$

$$= \mu - \frac{1}{4}\tilde{\omega}_o\,\mu\,H^{(1)}(\mu)\,[x_1 + x_2(3-\tilde{\omega}_o x_1)\mu^2]\,(\alpha_o-\alpha_2) +$$

$$+ \frac{1}{4}\tilde{\omega}_o\,\mu^2 H^{(1)}(\mu)[x_1 + x_2(3 - \tilde{\omega}_o x_1)\mu^2]\int_o^1 \frac{(1-\mu'^2)H^{(1)}(\mu')}{\mu+\mu'}\,d\mu'$$

$$+ \frac{1}{4}\tilde{\omega}_o\,\mu\, H^{(1)}(\mu)[c + x_2(3 - \tilde{\omega}_o x_1)\mu]\int_o^1 (1-\mu'^2)\mu' H^{(1)}(\mu')\,d\mu' \quad .$$

Making use of Lemma 1 and equation (14),

$$\sigma(\mu) = \mu - \frac{1}{4}\tilde{\omega}_o \mu H^{(1)}(\mu)[x_1 + x_2(3 - \tilde{\omega}_o x_1)\mu^2](\alpha_o - \alpha_2)$$

$$+ \mu^2 H^{(1)}(\mu)\left\{\frac{H^{(1)}(\mu) - 1}{\mu H^{(1)}(\mu)} - \frac{1}{4}\tilde{\omega}_o x_2(3 - \tilde{\omega}_o x_1)\right.$$

$$\left.\cdot\,[(\alpha_1 - \alpha_3) - (\alpha_o - \alpha_2)\mu]\right\}$$

$$+ \frac{1}{4}\tilde{\omega}_o \mu H^{(1)}(\mu)[c + x_2(3 - \tilde{\omega}_o x_1)\mu](\alpha_1 - \alpha_3) \quad .$$

Combining terms,

$$\sigma(\mu) = \mu H^{(1)}(\mu)\left\{1 + \frac{1}{4}\tilde{\omega}_o[c(\alpha_1 - \alpha_3) - x_1(\alpha_o - \alpha_2)]\right\} = q\mu H^{(1)}(\mu) \quad . \tag{27}$$

Substituting the expressions for $\beta(\mu)$ and $\sigma(\mu)$ from equations (26) and (27) into equation (12), one finds,

$$\left(\frac{1}{\mu} + \frac{1}{\mu_o}\right) S^{(1)}(\mu,\mu_o) = H^{(1)}(\mu)H^{(1)}(\mu_o)\left\{x_1 - x_1 p(\mu + \mu_o) + (x_1 p^2 - 3x_2 q^2)\cdot\right.$$

$$\left.\cdot\,\mu\mu_o\right\} \quad . \tag{28}$$

Identifying terms in this expression with those in equation (13b), one must have

$$c = x_1 p = \frac{1}{4}\tilde{\omega}_o x_1[x_2(3 - \tilde{\omega}_o x_1)(\alpha_1 - \alpha_3) + c(\alpha_o - \alpha_2)] \tag{29a}$$

$$3x_2 q^2 - x_1 p^2 = x_2(3 - \tilde{\omega}_o x_1) \quad . \tag{29b}$$

The solution of equation (29a) for p is:

$$p = \frac{\tilde{\omega}_o x_2 (3 - \tilde{\omega}_o x_1)(\alpha_1 - \alpha_3)}{4 - \tilde{\omega}_o x_1 (\alpha_o - \alpha_2)} \quad . \tag{30}$$

Substituting for $c = x_1 p$ into the expression for q defined in equation (27), one finds

$$q = \frac{1}{4[4 - \tilde{\omega}_o x_1 (\alpha_o - \alpha_2)]} \left\{ \tilde{\omega}_o^2 x_1 x_2 (3 - \tilde{\omega}_o x_1)(\alpha_1 - \alpha_3)^2 + [4 - x_1 \tilde{\omega}_o (\alpha_o - \alpha_2)]^2 \right\}$$

$$= \frac{1}{4[4 - \tilde{\omega}_o x_1 (\alpha_o - \alpha_2)]} \left\{ 16 - 8 x_1 \tilde{\omega}_o (\alpha_o - \alpha_2) + x_1 \tilde{\omega}_o^2 [x_1 (\alpha_o - \alpha_2)^2 \right.$$

$$\left. + x_2 (3 - \tilde{\omega}_o x_1)(\alpha_1 - \alpha_3)^2] \right\} \quad .$$

Invoking Lemma 2, this reduces to:

$$q = \frac{4}{3} \frac{(3 - \tilde{\omega}_o x_1)}{[4 - \tilde{\omega}_o x_1 (\alpha_o - \alpha_2)]} \quad . \tag{31}$$

With these determinations of p and q, the expression for $S^{(1)}(\mu, \mu_o)$ reduces to that given by Chandrasekhar for the conservative case.

It must finally be verified that equation (29b) is a tautology if the expressions for p and q given by equations (30) and (31) are used.

$$3x_2 q^2 - x_1 p^2 = \frac{x_2 (3 - \tilde{\omega}_o x_1)}{[4 - \tilde{\omega}_o x_1 (\alpha_o - \alpha_2)]^2} \left\{ \frac{16}{3} (3 - \tilde{\omega}_o x_1) - x_1 \tilde{\omega}_o^2 x_2 (3 - \tilde{\omega}_o x_1) \right.$$

$$\left. \cdot (\alpha_1 - \alpha_3)^2 \right\} \quad .$$

Making use of Lemma 2,

$$3x_2 q^2 - x_1 p^2 = \frac{x_2 (3 - \tilde{\omega}_o x_1)}{[4 - \tilde{\omega}_o x_1 (\alpha_o - \alpha_2)^2]} \left\{ \frac{16}{3} (3 - \tilde{\omega}_o x_1) + \tilde{\omega}_o^2 x_1^2 (\alpha_o - \alpha_2)^2 - \right.$$

$$- 8\tilde{\omega}_o x_1 [(\alpha_o - \alpha_2) - \tfrac{2}{3}]\Big\} = x_2 (3 - \tilde{\omega}_o x_1)$$

Q.E.D.

The remaining task is to derive an expression for the function $S^{(o)}$. It has been shown by Chandrasekhar that this function separates into H-functions only in the case $\tilde{\omega}_o = 1$.

Substituting the expressions for p and S given by equations (6) and (7) into equation (3), multiplying both sides by $d\varphi$ and integrating over 2π, the following expression emerges:

$$\left(\frac{1}{\mu}+\frac{1}{\mu_o}\right) S^{(o)}(\mu,\mu_o) = 1 - x_1\mu\mu_o + \frac{x_2}{4}(1 - 3\mu^2)(1 - 3\mu_o^2)$$

$$+ \frac{\tilde{\omega}_o}{2}\int_o^1 [1 + x_1\mu\mu'' + \frac{x_2}{4}(1 - 3\mu^2)(1 - 3\mu''^2)]\, S^{(o)}(\mu'',\mu_o)\, \frac{d\mu''}{\mu''}$$

$$+ \frac{\tilde{\omega}_o}{2}\int_o^1 [1 + x_1\mu_o\mu' + \frac{x_2}{4}(1 - 3\mu_o^2)(1 - 3\mu'^2)]\, S^{(o)}(\mu',\mu)\, \frac{d\mu'}{\mu'}$$

$$+ \frac{\tilde{\omega}_o^2}{4}\int_o^1\int_o^1 S^{(o)}(\mu,\mu')[1 - x_1\mu'\mu'' + \frac{x_2}{4}(1 - 3\mu''^2)(1 - 3\mu'^2)]$$

$$\cdot S^{(o)}(\mu'',\mu_o)\, \frac{d\mu''}{\mu''}\, \frac{d\mu'}{\mu'}$$

$$= \left\{1 + \tfrac{1}{2}\tilde{\omega}_o \int_o^1 S^{(o)}(\mu'',\mu_o)\, \frac{d\mu''}{\mu''}\right\}\left\{1 + \tfrac{1}{2}\tilde{\omega}_o \int_o^1 S^{(o)}(\mu',\mu)\, \frac{d\mu'}{\mu'}\right.$$

$$\left. - x_1\left\{\mu_o - \tfrac{1}{2}\tilde{\omega}_o \int_o^1 S^{(o)}(\mu'',\mu_o)\, d\mu''\right\}\left\{\mu - \tfrac{1}{2}\tilde{\omega}_o \int_o^1 S^{(o)}(\mu',\mu)\, d\mu'\right\} +\right.$$

$$+ \frac{x_2}{4} \left\{ 1 - 3\mu_o^2 + \frac{1}{2} \tilde{\omega}_o \int_o^1 (1 - 3\mu''^2)\, S^{(o)}(\mu'', \mu_o)\, \frac{d\mu''}{\mu'} \right\}$$

$$\cdot \left\{ 1 - 3\mu^2 + \frac{1}{2} \tilde{\omega}_o \int_o^1 (1 - 3\mu'^2)\, S^{(o)}(\mu', \mu)\, \frac{d\mu'}{\mu'} \right\}$$

$$= \epsilon(\mu)\, \epsilon(\mu_o) - x_1\, \eta(\mu)\, \eta(\mu_o) + \frac{x_2}{4}\, \xi(\mu)\, \xi(\mu_o)$$

$$= \gamma(\mu, \mu_o) \quad . \tag{32}$$

From this equation it may be shown that:

$$\epsilon(\mu) = 1 + \frac{1}{2} \tilde{\omega}_o \mu \int_o^1 \gamma(\mu, \mu')\, \frac{d\mu'}{\mu + \mu'} \tag{33a}$$

$$\eta(\mu) = \mu \left[1 - \frac{1}{2} \tilde{\omega}_o \int_o^1 \gamma(\mu, \mu')\, \frac{\mu' d\mu'}{\mu + \mu'} \right] \tag{33b}$$

$$\xi(\mu) = 1 - 3\mu^2 + \frac{1}{2} \tilde{\omega}_o \mu \int_o^1 (1 - 3\mu'^2)\, \gamma(\mu, \mu')\, \frac{d\mu'}{\mu + \mu'} \quad . \tag{33c}$$

The solution for $I(\mu, \mu_o, \varphi - \varphi_o)/F$ for arbitrary values of $\tilde{\omega}_o, x_1$ and x_2 boils down to the determination of the functions $H^{(2)}$, $H^{(1)}$, ϵ, η, and ξ. Equations (9), (28), and (32) are solved by initially assuming that each of these functions is identically 1 and iterating the appropriate equations. The integrations are performed numerically using 12-point gaussian quadrature. The solutions have been compared with the results of J. Hansen's doubling program for various combinations of $\tilde{\omega}_o$, x_1 and x_2. The agreement is to 1 part in 10^3, which is more than sufficient accuracy for the applications used

here. Furthermore, the technique derived in this appendix results in a considerable saving in computing time relative to the doubling routine, and is much more convenient to use when a variety of models are being explored.

REFERENCES

Arvesen, J.C., Griffin, R.N., and Pearson, B.D. (1969). Determination of extraterrestrial solar spectral irradiance from a research aircraft. Appl. Opt. 8, 2215-2232.

Axel, L. (1972). Inhomogeneous models of the atmosphere of Jupiter. Astrophys. J. 173, 451-468.

Barabashev, N.P., and Semejkin, B.E. (1933). Über die Helligkeitsverteilung auf diffusreflektierenden Kugeln im Zusammenhange mit der Planetenphotometrie. Zs. f. Ap. 7, 303-308.

Bergstralh, J.T. (1972). An observational test of absorption line formation models in the jovian atmosphere. Ph.D. Thesis, University of Texas at Austin.

Bergstralh, J.T. (1977). Private communication.

Binder, A.B., and McCarthy, D.W. (1973). IR spectrophotometry of Jupiter and Saturn. Astron. J. 78, 939-950.

Bryant, H.C., and Jarmie, N. (1974). The glory. Sci. Amer. 231, 60-71.

Chandrasekhar, S. (1960). Radiative Transfer, Dover Publications, New York.

Cochran, W.D. (1976). Jupiter: An inhomogeneous atmospheric model analysis of spatial variations of the H_2 4-0 S(1) line. Preprint.

Cochran, W.D., Gelfand, J.J., and Smith, W.H. (1976). Spatially resolved spectroscopy of Jupiter. I. H_2 quadrupole 4-0 S(1) line. Astrophys. J. 207, 639-645.

Danielson, R.E., and Tomasko, M.G. (1969). A two-layer model of the jovian clouds. J. Atmos. Sci. 26, 889-897.

Deirmendjian, D. (1969). Electromagnetic Scattering on Spherical Polydispersions. American Elsevier Publishing Co., New York.

Dlùgach, J.M., and Yanovitskij, E.G. (1974). The optical properties of Venus and the jovian planets. II. Methods and results of calculations of the intensity of radiation diffusely reflected from semi-infinite homogeneous atmospheres. Icarus 22, 66-81.

Fink, U., and Belton, M.J.S. (1969). Collision-narrowed curves of growth for H_2 applied to new photoelectric observations of Jupiter. J. Atmos. Sci. 26, 952-962.

Handbook of Chemistry and Physics (1972). 53rd edition, Chemical Rubber Co., Cleveland.

Hansen, J.E., and Travis, L.D. (1974). Light scattering in planetary atmospheres. Space Sci. Rev. 16, 527-610.

Hardie, R. (1954). Photometry with the Lowell 20-inch telescope. Astron. J. 59, 323-324.

Harris, D.L. (1961). Photometry and colorimetry of planets and satellites. In Planets and Satellites (G.P. Kuiper and B.M. Middlehurst, eds.), pp. 272-342. University of Chicago Press, Chicago.

Ingersoll, A.P., Münch, G., Neugebauer, G., Diner, D.J., Orton, G.S., Schupler, B., Schroeder, M., Chase, S.C., Ruiz, R.D., and Trafton, L.M. (1975). Pioneer 11 infrared radiometer experiment: The global heat balance of Jupiter. Science 188, 472-473.

Kattawar, G.W. (1975). A three-parameter analytic phase function for multiple scattering calculations. J. Quant. Spectr. Rad. Transf. 15, 839-849.

Khare, B.N., and Sagan, C. (1973). Red clouds in reducing atmospheres. Icarus, 20, 311-321.

MacRobert, T.M. (1967). Spherical Harmonics. Pergamon Press, New York.

McCord, T.B., and Westphal, J.A. (1972). Two-dimensional silicon vidicon astronomical photometer. Appl. Opt. 11, 522-526.

Oke, J.B. (1964). Photoelectric spectrophotometry of stars suitable for standards. Astrophys. J. 140, 689-693.

Oke, J.B., and Schild, R.E. (1970). The absolute spectral energy distribution of Alpha Lyrae. Astrophys. J. 161, 1015-1023.

Orton, G.S. (1975a). Spatially resolved absolute spectral reflectivity of Jupiter: 3390-8400Å. Icarus 26, 159-174.

Orton, G.. (1975b). The thermal structure of Jupiter. II. Observations and analysis of 8-14 micron radiation. Icarus 26, 142-158.

Pilcher, C.B., and Kunkle, T.D. (1976). Limb-darkening scans of Jupiter. Icarus 27, 407-415.

Strobel, D.F. (1969). The photochemistry of methane in the jovian atmosphere. J. Atmos. Sci. 26, 906-911.

Terrile, R.J., and Westphal, J.A. (1977). The vertical cloud structure of Jupiter from 5 μm measurements. Icarus 30, 274-281.

Tomasko, M.G., Clements, A.E., and Castillo, N.D. (1974). Limb-darkening of two latitudes of Jupiter at phase angles of 34^{o} and 109^{o}. J. Geophys. Res. 79, 3653-3660.

Tomasko, M.G., West, R., and Castillo, N.D. (1976). Photometry and polarimetry of Jupiter at large phase angles. I. Analysis of imaging data of a prominent belt and a zone from Pioneer 10. Preprint.

Weidenschilling, S.I., and Lewis, J.S. (1973). Atmospheric and cloud structures of the jovian planets. Icarus 20, 465-476.

Westphal, J.A. (1973). Application of the SIT vidicon to astronomical measurements. In Astronomical Observations with Television-Type Sensors (J.W. Glaspey and G.A.H. Walker, eds.), University of British Columbia, Vancouver.

Woodman, J.H. (1976). Jupiter: Observations of spatial variations of methane and ammonia interpreted as a cloud deck with elevated haze. Ph.D. Thesis, University of Texas at Austin.

van de Hulst, H.C. (1957). Light Scattering by Small Particles. Wiley and Sons, New York.

Zerull, R. (1976). Scattering functions of dielectric and absorbing irregular particles. In Proceedings of the IAU Colloquium No. 31, Heidelberg, 1975.

Zerull, R., and Giese, R.H. (1974). Microwave analogue studies. In Planets, Stars and Nebulae Studied with Photopolarimetry (T. Gehrels, ed.), University of Arizona Press, Tucson.

Part 2

SIMULTANEOUS ULTRAVIOLET (0.36 μm) AND INFRARED (8-20 μm) IMAGING OF VENUS: PROPERTIES OF CLOUDS IN THE UPPER ATMOSPHERE

Chapter 1

INTRODUCTION

"The time has come," the Walrus said
"To talk of many things:
Of shoes-and ships-and sealing wax-
of cabbages-and kings-
And why the sea is boiling hot-
And whether pigs have wings."

- Lewis Carroll
The Walrus and the Carpenter

Previous spatially resolved ground-based and spacecraft observations of the infrared radiation from Venus have called attention to many interesting properties of the planet's atmosphere (Sinton and Strong, 1960; Murray et al., 1963; Westphal et al., 1965; Diner et al., 1976; Ksanfomality et al., 1976). In particular, the nighttime side of the planet emits roughly as much flux as the daytime side and is actually warmer at certain longitudes; the planet is limb-darkened, with greater darkening toward the poles than along the equator; and anomalies in the thermal emission from the poles are sometimes apparent. The work described here is in essence a continuation of earlier ground-based studies, with better spatial, temporal, and spectral coverage. With the addition of a wobbling secondary to the 200-inch Hale telescope (Westphal et al., 1974) it has been possible to improve upon the effective spatial resolution and positional accuracy of two-dimensional maps of planetary radiation. In addition, the collection of the data in a digital mode, in conjunction with a picture playback system (Westphal, 1973), has allowed convenient production of digital images of Venus.

The improvement in spatial resolution has led to the discovery of a number of low contrast transient infrared features, in addition to a polar anomaly similar to that mapped by Murray et al., (1963). In combining the improvement in spatial resolution with wider temporal coverage, it has been possible to study the short and long term variability of the infrared features. The data indicate that the spatial distribution of thermal emission at low latitudes as well as the appearance of polar anomalies seem to be related to the diurnal insolation cycle. Narrowband observations of such features in the 8-20 μm region are valuable for limiting the possible explanations of the thermal contrasts, and measurements of the global infrared brightness distribution are useful for investigating the temperature and opacity structure of the Venus atmosphere.

An additional dimension to studies of the spatial distribution of the infrared flux from Venus has been obtained by recording simultaneous images of the planet in the ultraviolet. Ultraviolet albedo markings have been observed for the past 50 years, and the presence of a morphological correlation between infrared and ultraviolet features can provide valuable constraints on theories of the origin and nature of the upper atmosphere clouds. Evidence for such a correlation is presented in a later chapter. The correlation is interesting not only in terms of the information it yields regarding the source of the UV/IR features, but has relevance to the energy transport mechanisms operating in the Venus upper atmosphere.

Chapter 2

OBSERVATIONS

The twilight hours, like birds flew by,
As lightly and as free;
Ten thousand stars were in the sky,
Ten thousand in the sea.

- Amelia C. Welby
Twilight at Sea

Observatory, n, A place where astronomers conjecture away the guesses of their predecessors.

- Ambrose Bierce
The Devil's Dictionary

Venus was observed during the 1974, 1975, and 1977 apparitions at a variety of wavelengths and solar phase angles. In 1974 the data were collected at the Cassegrain focus of the Hale 200-inch telescope on Palomar Mtn.; during the later apparitions the detectors were located at the East-arm Cassegrain focus. The telescope was equipped with a "wobbling" Gregorian secondary mirror positioned about 1 meter above the prime focus. The f/72 beam from the secondary was split into a reflected infrared component and a transmitted ultraviolet/visible component using a glass plate containing a Liberty Mirror IR-81-E conductive infrared gold reflection coating and placed at a 45° angle to the light path. This dichroic has a fairly flat spectral response from 8 - 20 μm with about 94% reflectance at these wavelengths. The transmittance peaks in the visible at a value of 79% at 6000Å and drops off to about 20% at 3600Å. The ultraviolet and visible components of the transmitted beam were isolated from one another in a manner described later in this chapter. In

procurement of the ultraviolet measurements, the UV flux from Venus was of sufficient magnitude that it was not necessary to remove the IR dichroic from the light path.

Detection of the infrared flux from Venus was accomplished with a gallium doped germanium bolometer which changes conductivity in response to temperature fluctuations induced by variations in the incident radiation. The bolometer is housed in a multi-walled Low dewar and remains in thermal communication with liquid helium in the inner chamber of the dewar. Pumping on the LHe cools the detector to about 2°K. A series of concentric liquid-nitrogen-containing and evacuated chambers provide thermal insulation. The dewar contains, along with the detector: a load resistor, a variety of field-limiting apertures, a field lens, an internal cooled filter wheel, and a KBr window at the entrance port. The internal filter wheel contains broadband 8-14 μm and 16-25 μm blocking filters which could be used alone or in conjunction with external narrowband filters. In all observations the internal 2 mm focal plane aperture--corresponding to a resolution element of 1.1 arcsec on the sky--was selected.

An external room-temperature rotating filter wheel was positioned between the IR dichroic and the entrance port of the LHe dewar. A set of 6 Optical Coating Laboratory, Inc. narrowband interference filters was used for the observations, and each filter will be referred to in the text by its central wavelength as follows: 8.7, 9.5, 11.2, 12.5, 18.3, and 19.8 μm. The filter transmission functions were

measured on a Perkin-Elmer Model 180 infrared spectrophotometer and Table I presents a summary of the characteristics of each of the filters used, including full width at half-maximum (FWHM) bandpass.

During the 1974 apparition, only infrared measurements near 10 μm were made. In later observations, simultaneous ultraviolet and 20 μm data were collected as well. Initially, separation of visible light for viewing and ultraviolet light for imaging was accomplished by placing an Edmund Scientific Co. "green" dichroic at a 45° angle to intercept the transmitted portion of the beam beyond the IR dichroic. The second dichroic has about 55% reflectance at 3600Å, and the reflected beam was directed onto the S-20 photocathode of an ITT FW-130 photomultiplier. The photomultiplier was housed in a cold box and cooled with dry ice to reduce the thermal dark current. A variable focal plane iris aperture was located in front of the entrance window to the cold box and was adjusted to 2 mm diameter to correspond to the spatial resolution obtained in the infrared. The transmitted beam from the "green" dichroic was viewed with an eyepiece for finding and guiding. Unfortunately, the field of view afforded by this arrangement was fairly small, and the set-up was not only inconvenient for guiding but made it difficult to locate Venus in the sky. For these reasons the viewing portion of the system was modified by using a 4.8" field lens to convert the f/72 beam to f/10. This resulted in a convenient viewing and guiding field of roughly 1 arcmin in diameter. The placement of the lens, however, required

Table I

Filter characteristics

Filter	Peak transmission (with blocking filter)	FWHM bandpass
OCLI 8.7 μm	60%	1.1 μm
" 9.5 μm	62%	1.4 μm
" 11.2 μm	68%	1.5 μm
" 12.5 μm	66%	1.4 μm
" 8-14 μm	88%	5.2 μm
" 18.3 μm	30%	1.6 μm
" 19.8 μm	24%	2.1 μm
Spectrolab 3600Å	30%	200Å

repositioning of the photomultiplier cold box. A small elliptical flat of roughly 2 cm in minor diameter was mounted at 45° on a glass plate to divert the central portion of the f/72 beam sideways from the mounting assembly; another small 45° flat diverted the beam into the repositioned cold box. In addition to the increase in viewing field this design permitted, the elimination of the second ("green") dichroic resulted in better UV transmittance and made the system more versatile for use at other wavelengths. Bandpass in the ultraviolet was limited using a Spectrolab 3600Å interference filter placed behind the 2 mm iris aperture. The characteristics of this filter were measured on a Cary Model 17I recording spectrophotometer and are summarized in Table I.

In 1974 the infrared measurements were performed in DC mode, that is, without chopping between planet and sky. Due to problems arising from low frequency drifts in the detector and poor signal to noise ratio in the narrowband channels, measurements taken in later years were performed in a chopping mode. The signal was amplified and sent to an A/D converter for digitization to 8 bits. The data numbers (0-255) were written on IBM compatible digital magnetic tape using a Cipher Data Products 800 bpi 9 track tape recorder. Chopping between planet and sky was accomplished with the wobbling secondary mirror. The "wobble" results in displacement of an image in the north-south direction. The rocking motion of the mirror is controlled by a pair of servos which drive a deflection of the mirror in proportion to an input voltage. Thus, input of a square wave translates

into alternate positioning on two spots; the frequency and duty cycle of the square wave determine the dwell time on each spot and the amplitude controls the spatial separation. A 12.5 hz square wave with a 50% duty cycle and several volts amplitude was used to drive the mirror chop. This resulted in an integration time of 40 msec each on planet and sky, for a total of 80 msec per resolution element (also referred to as a picture element, or pixel). The square wave was simultaneously used as a reference signal for a Princeton Applied Research phase-lock amplifier; the amplified (planet minus sky) signal was then filtered, digitized, and written on magnetic tape.

Ultraviolet observations were made in a DC mode with an 80 msec integration time per resolution element. The signal from the photomultiplier was amplified with an operational amplifier and also digitized to 8 bits and recorded on magnetic tape. In light of the data handling requirements, UV and IR data were not recorded concomitantly. In addition, differential refraction in the Earth's atmosphere would insure that the UV and IR detectors would not sample identical spots on the Venus disk. Therefore, the UV data were collected when the sky was dark, and the remainder of the twilight time (either afternoon or morning, depending on Venus' elongation) was used for the IR measurements. This resulted in only a short time interval between collection of the UV and IR images; given the spatial resolution of the data and the apparent Venus atmosphere rotation period of four terrestrial days, near-simultaneous imaging is adequate.

Images of Venus were obtained by feeding a staircase voltage ramp to the wobbling secondary in 64 80-msec steps to sweep the focal plane image of Venus past the entrance apertures. The amplitude of the ramp was adjusted to yield a mirror throw that encompassed the whole disk and insured some sky signal beyond each of the limbs. In those instances in which the chopping mode was employed, the ramp was modulated by the chopping square wave. Flyback of the secondary mirror in preparation for the next scan required 640 msec per scan. Since the mirror scanned in declination, the planet was permitted to drift in right ascension by introducing an offset into the telescope sidereal tracking rate. This combination of mirror scan and flyback plus orthogonal telescope drive produced a raster scan pattern by which two-dimensional images of Venus were built up at a rate of 368.6 seconds per picture. (The foregoing timing parameters refer to the 1975 and 1977 apparitions in which chopping and simultaneous UV/IR coverage were achieved. In 1974 the mirror was driven with 128 10-msec steps with 80 msec for mirror flyback, so that an entire image was built up in 174.1 sec. With the factor of 8 longer integration time per scan in 1975 and 1977, sample density was sacrificed somewhat so that observing time per picture did not become prohibitively long and such that more images could be obtained in the limited telescope time available during twilight.) Incoming scans were monitored in real time with an oscilloscope synchronized with the mirror sweep. The pixellated images could also be viewed in real time with a 6-bit

digital scan converter and video monitor, or at leisure in the laboratory with a picture playback system (Westphal, 1973) which also permits individual scans in an image to be accessed and viewed on an oscilloscope and which can be used to produce hard copy Polaroid pictures of the two-dimensional data.

No absolute calibration of either the infrared or ultraviolet measurements was made during these observations. Absolute calibration of infrared data is reliable only from a dry, high altitude observing site and Palomar Mountain is unsuitable for such an endeavor. Thus, it was felt that the twilight hours were optimally utilized by concentrating on obtaining good spatially resolved measurements of relative brightness variations across the planetary disk, including high spatial frequency transient features with low contrast, for which the Hale 200-inch telescope is by far the best instrument available. Relative measurements of brightness temperature are accurate to between ¼ and ½°K in the 8-14 μm region and 1-2°K at 18 and 20 μm. Table II presents a summary of the dates of observation on which the weather was good and seeing was less than 3 seconds of arc. Also shown for each date are the wavelengths observed, Venus phase angle, and planet semi-diameter.

Table II

Observational log

Date (UT)	Wavelength	N*	S.D.†	$\alpha^{\S}$	Terminator in view
6 March 1974	8-14 μm	3	18.3	112°	morning
4 July 1975	8-14 μm	2	14.4	102°	evening
"	3600Å	2	"	"	"
5 July 1975	8-14 μm	3	14.6	102°	evening
"	3600Å	2	"	"	"
20 July 1975	8.7 μm	1	18.3	116°	evening
"	9.5 μm	2	"	"	"
"	11.2 μm	1	"	"	"
"	12.5 μm	1	"	"	"
"	8-14 μm	1	"	"	"
"	3600Å	4	"	"	"
1 August 1975	9.5 μm	1	22.2	130°	evening
"	11.2 μm	1	"	"	"
"	8-14 μm	1	"	"	"
"	3600Å	1	"	"	"
26 September 1975	8.7 μm	2	21.6	125°	morning
"	9.5 μm	2	"	"	"
"	11.2 μm	2	"	"	"
"	12.5 μm	2	"	"	"
"	8-14 μm	4	"	"	"
"	3600Å	3	"	"	"

Table II
(continued)

Date (UT)	Wavelength	N*	S.D.†	α§	Terminator in view
22 October 1975	8.7 μm	2	14.8	100°	morning
"	9.5 μm	2	"	"	"
"	11.2 μm	2	"	"	"
"	12.5 μm	2	"	"	"
"	8-14 μm	1	"	"	"
"	18.3 μm	2	"	"	"
"	19.8 μm	2	"	"	"
"	3600Å	2	"	"	"
27 October 1975	8.7 μm	2	13.7	96°	morning
"	9.5 μm	2	"	"	"
"	11.2 μm	1	"	"	"
"	12.5 μm	2	"	"	"
"	18.3 μm	3	"	"	"
"	19.8 μm	2	"	"	"
"	3600Å	2	"	"	"
15 November 1975	8.7 μm	4	11.2	84°	morning
"	9.5 μm	2	"	"	"
"	11.2 μm	2	"	"	"
"	12.5 μm	2	"	"	"
"	8-14 μm	1	"	"	"
"	3600Å	3	"	"	"

Table II
(continued)

Date (UT)	Wavelength	N*	S.D.†	$\alpha^{\S}$	Terminator in view
13 February 1977	8.7 μm	2	15.4	102°	evening
"	9.5 μm	2	"	"	"
"	11.2 μm	2	"	"	"
"	12.5 μm	2	"	"	"
"	8-14 μm	6	"	"	"
"	3600Å	4	"	"	"
14 February 1977	8.7 μm	1	15.6	102°	evening
"	9.5 μm	2	"	"	"
"	11.2 μm	1	"	"	"
"	12.5 μm	1	"	"	"
"	8-14 μm	7	"	"	"
"	3600Å	5	"	"	"

*N = number of usable images obtained
†S.D. = Venus semi-diameter (arcsec)
§α = phase angle

Chapter 3

IMAGE PROCESSING

"What is the use of a book," thought Alice
"without pictures or conversations?"

- Lewis Carroll
Alice's Adventures in Wonderland

Procurement of the Venus data in digital form made it fairly straightforward to obtain cosmetically improved images from the raw data. The following discussion details the procedures which were used to 1) filter and average the data to reduce high-frequency noise; 2) enhance contrast to bring out subtle features; and 3) correct for spatial shifts and distortions.

The data obtained on 6 March 1974 were the first actual images of Venus to be recorded at 10 μm and several band-like features were discovered (Diner et al., 1976). Unfortunately, all efforts to enhance the contrast were doomed to failure due to a low frequency drift in the detector, a problem which arose because of the DC mode of observation and which, due to the side-by-side stacking of individual scans, gave rise to high spatial frequency noise in the direction perpendicular to the scans. Contrast enhancement accentuated this effect and intensified the global shading due to limb-darkening, making it difficult to observe real high spatial frequency features in the data. Partial solution to the first problem was accomplished by adding several images together; since detector drift is a random process, this improved the signal-to-noise ratio by a factor roughly

equal to the square-root of the number of pictures averaged. Registration of images required determination of the disk centers. This was accomplished by fitting an ellipse to the location of the planetary limbs, where the limbs are defined as the positions of the maximum first derivatives in a scan. An ellipse was used rather than a circle since the pixel overlap was not the same in the scan and drive directions. The unequal horizontal and vertical pixel spacings were not corrected for in the 1974 data although a technique (described below) was later developed to repixellate the images to circular disks. Once registered, three 8-14 μm images were averaged; however, this did not completely eliminate the noise problem. Adjustment of individual scans to a uniform sky level afforded additional improvement but spatial filtering was still necessary. One-dimensional smoothing of the data in the direction perpendicular to the scans using a low-pass Fourier filter was experimented with and finally abandoned since removal of the high frequency information required to synthesize the sharp planetary limbs resulted in the introduction of ripple artifacts. One-dimensional spatial smoothing using a running second order polynomial least-squares filter was found to be quite successful. In this method, the central data number (DN) of a line segment is replaced by the value, at that location, of a second order polynomial fit to the points in the segment. The filter is slid along a data line one pixel at a time. The length of the segment determines

the degree of smoothing, and a length of roughly 10% of the disk diameter was found to provide adequate filtering while leaving the limb profile virtually unchanged.

Removal of global shading was accomplished in a simple and straightforward manner. For this purpose, no attempt was made to find a function which accurately approximated the low frequency harmonics in the disk brightness distribution. It was assumed that the brightness of a point at a given viewing geometry could be represented by the linear relation

$$B(\mu) = B(1)(1 - D + D\mu) \qquad (1)$$

where μ is the cosine of the angle between the directions to the observer and the local normal, B(1) represents the model brightness assuming the point to be observed at normal incidence, and D is a parameter that can adopt values between 0 and 1. Calculation of μ at a given point and division of the measured brightness by $(1 - D + D\mu)$ results in the removal of a certain amount of limb-darkening, depending upon the choice for D. Note that D is chosen arbitrarily, and that this procedure is purely cosmetic.

Contrast enhancement was accomplished by multiplying all data numbers in an entire image by an arbitrary factor; although this leaves relative contrast unchanged, the absolute differential in brightness between any two points increases by an amount proportional

to the numerical factor applied. This technique required the subtraction of a DC level to keep all DN within the 12-bit capability of the picture playback system.

Recording the infrared data in chop mode eliminated the type of drift problem encountered in 1974 such that the S/N ratio in the direction perpendicular to the scans was comparable to the S/N ratio along the scans. This improvement in overall data quality allowed production of good quality narrowband images in addition to the broadband 8-14 μm data. Although chopping yielded cleaner images, occasional seeing tears, noise spikes, data dropouts, and variable sky transmission required repeated imaging at each wavelength followed by image averaging. The resulting signal-to-noise ratio obtained (~100-200) was particularly crucial given the low contrast of the features observed on the Venus disk.

On certain dates of observation, the motion of Venus in the sky was of considerable magnitude so as to result in a noticeable drift within a field in which the telescope was tracking at the sidereal rate. The component of this motion in right ascension was of minor concern in that its only effect was to yield an R.A. offset drive rate that was slightly different from the nominally specified value. The declination component of the motion caused the scans to be progressively displaced north or south as a data frame was recorded. This drift was sometimes so rapid that an offset in the declination

tracking was required to prevent the limb of the planet from drifting off the edge altogether. In cases where this procedure was not used, or when a residual skewing remained, scan lines were shifted systematically as part of the computer digital processing of the data.

With the large number of pictures obtained during the 1975 and 1977 observing periods, it became obvious that a rigorous solution for the limb and center locations for each image using the least-squares ellipse fitting method would be not only costly but tedious and time-consuming as well. Therefore, a simpler method was employed: An east-west scan through roughly the middle of the disk was examined; the midpoint of this scan (the point halfway between the limbs) determined one Cartesian coordinate of the disk center; the midpoint of the north-south scan passing through this point determined the other. The lengths of the semi-major and semi-minor axes of the disk equal the distances from the central datum to the limbs on orthogonal scans through the point. The accuracy of this method is good, as evidenced by measurements on infrared images obtained on the same date with identical mirror drive ramp voltage settings and right ascension offset tracking rates. In such images, identical values of semi-major and semi-minor axes were obtained to within 1 or 2 pixels in a 256 x 256 format. Since the ultraviolet images represent reflected sunlight, such that radiation is not received from all parts of the disk (as in the case of thermal emission), the

geometrical parameters obtained from infrared images were applied to the partially illuminated (i.e., crescent or gibbous) UV images recorded on the same date.

Line dropouts or noise spikes in the images were edited by replacing the data number in a bad point by the average DN in unaffected neighboring points. Once edited, corrected for systematic spatial shifts, and geometrically parameterized, all images were repixellated. The primary function of repixellation is expansion of 64 x 64 or 128 x 128 data frames to a 256 x 256 format compatible with the picture playback system. In the preliminary stages of image processing, compatible images were obtained by duplicating each pixel in the horizontal and vertical directions so as to yield a 256 x 256 format. This procedure is adequate for the purposes of measuring geometric parameters, compensating for north-south drift, or line-by-line editing, but gives rise to images with a "chunky" appearance. Mapping of a 64 x 64 or 128 x 128 array into the larger format using a bilinear interpolation scheme was performed in the final stages, and was frequently combined with a geometric expansion or contraction of the Cartesian coordinates to compensate for the unequal pixel spacing in the scan and drive directions and to yield circular planetary images. A spatial translation was also included in the mapping process, thereby shifting all disk centers to the location $(x,y) = (128,128)$. This registration of images was a prerequisite for the averaging of similar data frames.

Image averaging to reduce noise was followed by a final processing step which involved the scan-by-scan removal of any remnant low frequency drift in the sky background. Points on opposite sides of the planet served as endpoints for a linearly sloping background level that was subtracted from each scan. At this point, a "finished" composite image represents the best estimate of the actual brightness distribution over the disk of Venus, and the data numbers, minus a uniform sky level, are directly proportional to the planetary flux. For the purposes of investigating diurnal phase effects in infrared flux, limb-darkening, model atmospheres, and contrast variations, these composite images are used. Further image modification procedures, including removal of global shading and contrast stretches, are performed for the purpose of obtaining enhanced pictures for visual evaluation without strict regard to the photometric decalibration involved, other than to insure that no artifacts are inadvertently introduced.

Chapter 4

RESULTS AND DISCUSSION

I keep six honest serving men
(They taught me all I knew);
Their names are What and Why and When
And How and Where and Who.

- Rudyard Kipling
The Elephant's Child

It is better to know some of the questions
than all of the answers.

- James Thurber

A summary of the results of the infrared and ultraviolet imaging will be divided into five sections. Although the subject matter in each section represents a distinct topic of interest, the order of the discussion is chosen such that each section makes use of results of the sections which precede it. Section 1 discusses the nature of the equatorial infrared brightness distribution and its relation to the diurnal insolation cycle. Section 2 presents equatorial 8-20 μm limb-darkening data and compares the results with the predictions of a simple atmospheric model. Section 3 compares the spectral dependence of the polar limb-darkening with the results of Section 2. Section 4 deals with the temporal and spectral characteristics of infrared polar anomalies. The final section presents a comparison of infrared and ultraviolet images, and discusses the evidence pertaining to the existence of a correlation between these sets of data.

Section 1. Variations in equatorial brightness

Measurements of the diurnal variation of infrared flux from a planetary atmosphere are critical for an understanding of the energy transport processes and cloud dynamics operative on a global scale. One of the major driving forces of the Venus global circulation is the periodic insolation variation. Horizontal winds may arise from temperature contrasts on isobaric surfaces, and vertical motions may be induced as a result of heating or cooling associated with insolation changes. Infrared brightness contrasts may also be associated with the motion of cloud masses; the Mariner 10 photographs (Murray et al., 1974) show, for example, that at high altitudes the subsolar region of Venus is highly convective so that the vertical displacement of aerosols will influence the infrared brightness temperatures obtained by remote sensing of this region.

An estimate of the flux emitted from a point on the planet requires measurement of the intensity (or surface brightness) at all viewing geometries; flux is then given by

$$\text{Flux} = 2\pi \int_0^1 B(\mu)\mu d\mu \qquad (2)$$

where $B(\mu)$ is the intensity in the direction defined by the cosine of the angle to the local normal, μ. The intensity observed at normal incidence is therefore denoted as $B(1)$. If the limb-darkening law is similar from one point on the planet to another, i.e.,

$B(\mu) = B(1) \cdot f(\mu)$, where B(1) may vary from point to point but the function $f(\mu)$ does not, then by equation (2) flux will be everywhere proportional to B(1). An orbiting spacecraft is well suited to measure B(1) at many locations on a planet, whereas the coverage obtained from the Earth is necessarily restricted to a small sample of points where B(1) may be directly observed. If the Venus atmosphere was homogeneous and the limb-darkening law was known, measurement of brightness at an arbitrary viewing angle could be corrected to obtain $B(1) = B(\mu)/f(\mu)$, thereby greatly extending the available coverage.

A systematic attempt to study the diurnal behavior of the 8-14 μm emission from Venus was made by Ingersoll and Orton (1974) using the infrared contour maps of Murray et al. (1963) and Westphal et al. (1965). Ingersoll and Orton defined the limb-darkening function to be invariant over the disk and from one map to another, such that the residuals which remain upon removal of this function represent an estimate of diurnal and transient effects. Utilization of maps at many phase angles therefore leads to an empirical estimate of the limb-darkening law. By fitting the data by least-squares to a model in which the limb-darkening function was assumed to be a Legendre series in μ and assuming the "solar-related" component to be represented as a series of spherical harmonics, Ingersoll and Orton were able to separate the limb-darkening and diurnal effects. They

found that the "solar-related" component of infrared intensity reaches a maximum at a longitude of 210° relative to the subsolar point and minima at about 100° and 300°. In this system, the longitude of the morning terminator is 90° and the evening terminator is at 270°. The peak-to-peak amplitude of this function was found to about 4°K, representing a gradual increase in intensity as the Sun sets on Venus and the atmosphere is immersed in darkness. Ingersoll and Orton pointed out that the interpretation of this variation is ambiguous in that it may be attributed either to thermal contrast on isobaric levels or to vertical displacement of clouds in the presence of a temperature gradient.

A number of factors, including the low spatial resolution of the infrared contour maps; an uneven distribution in phase coverage with essentially four distinct phase angles sampled prior to inferior conjunction as opposed to only one following conjunction; the fact that not all of the maps were obtained during the same apparition; and the result that the "solar-related" intensity maximum occurs at a longitude identical to the central meridian longitude of the map with the highest spatial resolution (and thus given considerable weight in the fitting procedure) suggested repetition of this experiment with better spatial resolution and more even phase converage. Thus, an analysis similar to that performed by Ingersoll and Orton was made using the imaging data obtained during the 1975 apparition. To keep the analysis simple, only data points along the illumination

equator were used. For the purpose of comparison with the results of Ingersoll and Orton this approach is valid, since the results obtained by considering only equatorial data in the 1962-64 contour maps are virtually identical to those obtained when points at higher latitudes are included (Orton, 1975). The limb-darkening function was assumed to be represented by a third order polynomial in μ. Data at points at which $\mu < 0.5$ were excluded from the analysis, due to the effects of seeing at high viewing angles. The basic conclusions are not especially sensitive to the order of the polynomial used, although the residuals are decreased somewhat as the order is increased from 2 to 3. Since the images obtained on various dates of observation were not calibrated in an absolute sense, a multiplicative gain factor was assumed for each image. These factors were treated as model parameters and returned by the least-squares solution in minimizing the residuals. This is the same procedure that was adopted by Ingersoll and Orton, who did not make use of the absolute calibrations of the 1962-64 data.

The least-squares solution is obtained by minimizing the sum of the squares of the residuals

$$R = \sum_{i,j} [DN_{ij} - g_j f(\mu_i)]^2 \qquad (3)$$

where DN_{ij} is the data number of the i^{th} point on the j^{th} image; g_j is the gain factor of the j^{th} image; and $f(\mu_i) = 1 + a(\mu_i - 1) + b(\mu_i^2 - 1) + c(\mu_i^3 - 1)$ is the model limb-darkening function evaluated

at the value of μ for the i^{th} point. The parameters of the model are the g_j's and a, b, and c. The solution is obtained using a non-linear least squares method which solves for the increments in each of the model parameters required to minimize R, starting with an initial guess for each parameter. This iterative procedure made use of the initial guess $g_j = 1$ for all j, a = 0.5, b = c = 0, and convergence was obtained after about 6 iterations. Ingersoll and Orton's technique differed from this method in that they fitted limb-darkening and "solar-related" functions to the data simultaneously, and considered the residuals to consist only of transient effects and noise. In the present analysis, the "solar-related" component is included in the residuals, i.e., only limb-darkening is fitted. Application of the latter technique to the data of Murray et al. (1963) and Westphal et al. (1965) yields a plot of residuals vs. solar longitude that is virtually identical to Ingersoll and Orton's "solar-related" function; therefore, it is possible to make a valid comparison between Ingersoll and Orton's "solar-related" phenomena and the residuals determined by removing only limb-darkening from the data acquired during the 1975 apparition. The analysis was performed on the data at 8-14 μm as well as each of the narrowband channels. The significance of the wavelength dependence of the limb-darkening function will be discussed in the following section.

The widest coverage in phase angle was obtained in 1975 for the broadband 8-14 μm channel. A total of 7 images were used in the

analysis, representing four phase angles prior to inferior conjunction, and three following conjunction. The orbital geometry for these images has been summarized in Table II. The residuals between the data and the model for the 8-14 μm channel are expressed as brightness temperatures, ΔT, and plotted versus longitude relative to the subsolar point in Figure 1. The longitude convention is the same one adopted by Ingersoll and Orton (1974). The root-mean-square (RMS) residual from the model fit is 0.4°K, which is comparable to the experimental uncertainty in the brightness temperature of each point. Nevertheless, the data show an increase in 8-14 μm flux as the atmosphere emerges from daylight into evening, although the peak-to-peak amplitude of this effect (~2°K) is not as large as Ingersoll and Orton's value of 4°K. Figure 1 shows evidence of intensity maxima, separated by nearly 180° of longitude, that is, at 70° and 246°. Note that the "solar-related" component derived by Ingersoll and Orton was also suggestive of a functional dependence containing two maxima and two minima.

In the analysis used to produce Figure 1, the use of arbitrary multiplicative gain factors from one image to another tends to minimize the amplitude of "solar-related" flux variations, given that the true phase variation of absolute disk brightness was not measured. However, the work of Ingersoll and Orton, the preceding analysis, Venera orbiter results (discussed below), and the following discussion show that there are clear systematic day-night asymmetries

Figure 1. Residuals between equatorial 8-14 μm data and least squares fit limb-darkening model expressed as brightness temperatures plotted vs. longitude relative to the subsolar point. The uncertainty in each data point is roughly ¼ - ½ °K and the RMS residual in this figure is 0.4°K. The presence of a flux increase as the atmosphere emerges from daylight into evening is consistent with the results of Ingersoll and Orton (1974).

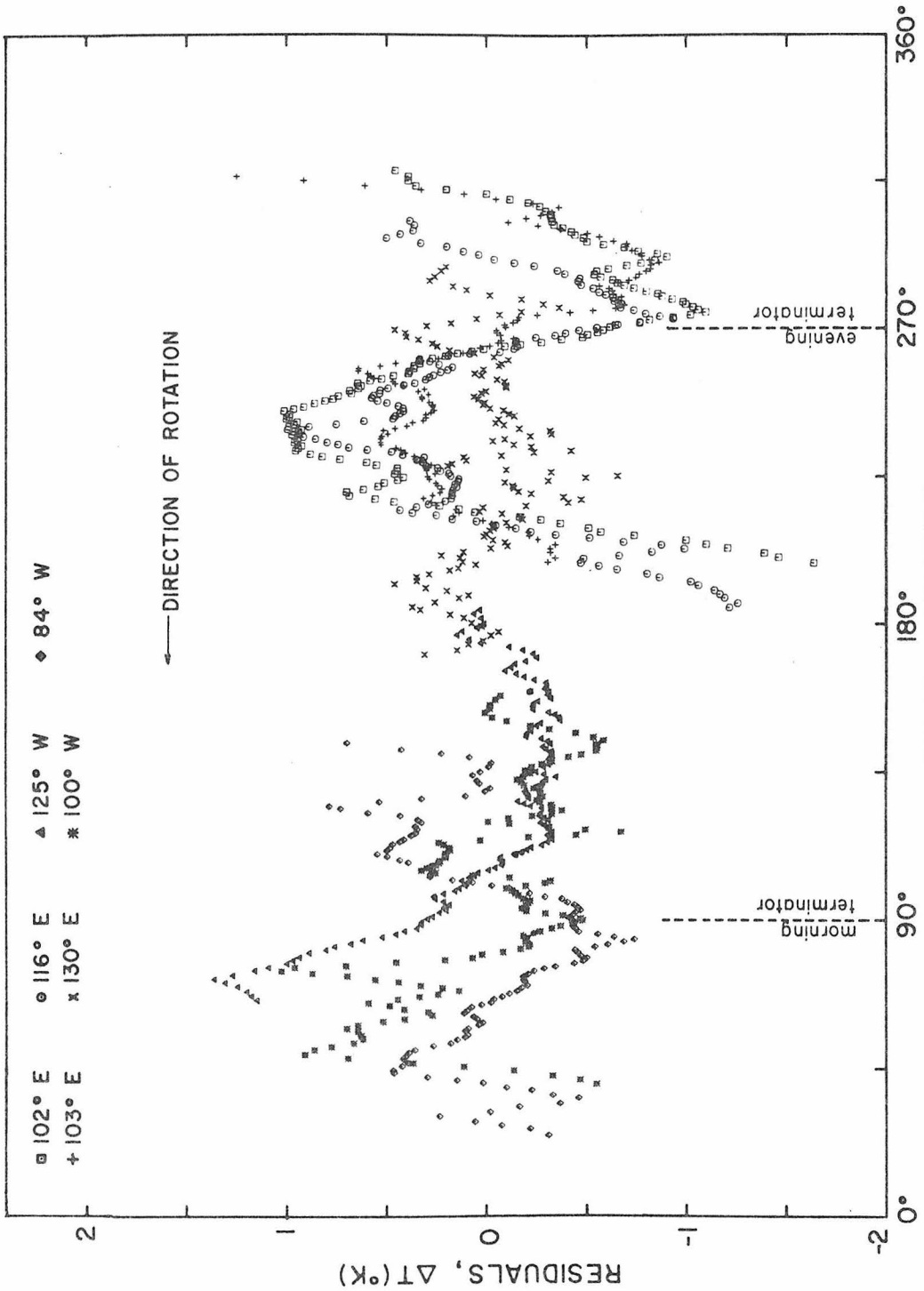
RESIDUALS, ΔT (°K)
2
1
0
-1
-2
0°
90°
180°
270°
360°
SOLAR LONGITUDE
morning terminator
evening terminator
DIRECTION OF ROTATION
102° E
103° E
116° E
130° E
125° W
100° W
84° W

Fig. 1

in the infrared flux from Venus. Furthermore, the following discussion shows that the quantitative differences in the results obtained from the 1962-64 data and the 1975 data are due to a real variability in the day-to-day spatial distribution of the thermal emission.

Figures 2a and 2b compare equatorial scans from 8-14 μm images in which the evening and morning terminators, respectively, were close to the central meridian. The data are normalized to the DN at the center of the disk. Figure 2a shows that there is a systematic west-east (that is, day-night) contrast across the evening terminator, although the magnitude of the asymmetry is variable not only from one apparition to another, but more importantly, from one day to the next. The difference in brightness temperature between dark and sunlit points equidistant from the central meridian ranges from ~2°K on UT 5 July 1975 to better than 5°K on UT 14 February 1977. In light of this variability, the differences in the results reported by Ingersoll and Orton (1974) and those reported above are not surprising. Figure 2b shows that contrast across the morning terminator is on the average much smaller than on the evening side, although on some dates differences of 1-2°K are detected near the limbs, with the sunlit side warmer than the dark side. A similar result was reported by Sinton and Strong (1960), and the asymmetry may be seen in the contrast enhanced 8-14 μm image from UT 6 March 1974 displayed later in this chapter (Figure 3c).

Figure 2a. Comparison of east-west scans from images in which the evening terminator was within 20° of the central meridian. Significant variations in the shape of these scans are observed on a daily time scale as well as from one apparition to another, although a systematic increase in brightness temperature from west to east is apparent.

Figure 2b. Same as Figure 2a except the morning terminator is close to the central meridian. A day-night asymmetry as large as that seen near the evening terminator is not observed, although close to the limb ($\mu \sim 0{,}5$) the sunlit side is sometimes 1 - 2°K warmer than the dark side.

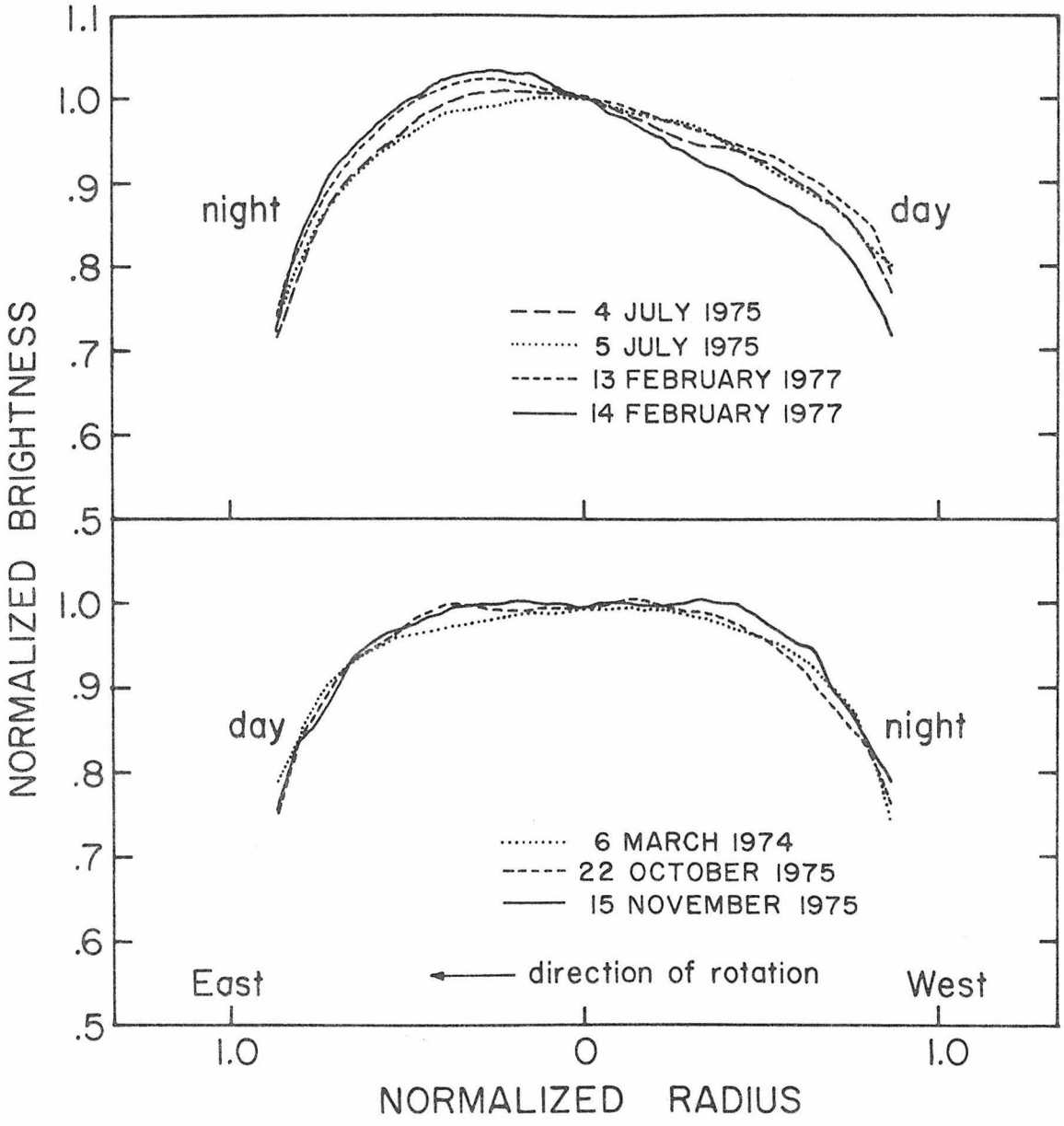
1.1
1.0
.9
.8
.7
.6
.5
night
day
4 JULY 1975
5 JULY 1975
13 FEBRUARY 1977
14 FEBRUARY 1977
day
night
6 MARCH 1974
22 OCTOBER 1975
15 NOVEMBER 1975
East
direction of rotation
West
NORMALIZED BRIGHTNESS
1.0
0
1.0
NORMALIZED RADIUS

Figs. 2a, 2b

Figures 6 and 7 in Section 5 of this chapter show that the spatial distribution of infrared features with lateral scales on the order of 1000 km changes on a time scale of a terrestrial day, so it is likely that the variability in the observed night-day contrasts is influenced by either the vertical motions of clouds or rotation of clouds of different heights through the field of view. Possibly the general increase in thermal emission on the planet's evening side is due to the gradual sinking of the average level of clouds which have previously risen by convection in the subsolar region. There is evidence of such convection in Mariner 10 UV images (Murray et al., 1974), and a similar explanation of the day-night contrast across the evening terminator was proposed by Ksanfomality et al. (1976) in their discussion of the Venera 9 and 10 infrared results. Assuming a brightness temperature increase of 5°K from day to night (the maximum value determined from Figure 2a) through an angular distance of 60° of longitude, one can calculate the vertical velocity of any such sinking cloud mass. Taking the apparent horizontal velocity to be 100 m/sec, the altitude to be 75 km above the surface, and the lapse rate to be -3°K/km (see Section 2 of this chapter), the vertical velocity turns out to be about 3 cm/sec. Alternatively, it is possible that the nighttime flux increase arises from the gradual clearing of a high level cloud, leading to a decrease in infrared opacity.

As shown in Figures 2a and 2b, the regions near the evening and morning terminators show quite different longitudinal distributions of thermal emission. O'Leary (1974a) has pointed out that "reverse-C" shaped features seen in ultraviolet photographs seem to form preferentially near the evening terminator, and are found much more rarely on the morning side. The reverse-C features may be the manifestations of waves downstream of the convective subsolar region. Thus, the evening-morning disparity which is seen in infrared images appears to have a counterpart in reflected sunlight. A small night-day asymmetry in the infrared on Venus' morning side could be due to warming of the atmosphere due to solar heating, or, as alternatively suggested for the region near the evening terminator, evaporation of a condensate permitting observation of deeper (and warmer) levels. An observational constraint on mechanisms attempting to account for the increase in flux from the dark to sunlit sides of the morning terminator is concerned with the spatial scale of the brightening, i.e., whether the increase is gradual (as on the evening side) or abrupt (that is, occurring on a short time scale in response to sunrise). The data presented here indicate the former, but some of the equatorial scans obtained by Westphal (1971) show a local brightening associated with the morning terminator. This question should be pursued in future observations; if the morning brightening arises from the evaporation of a high atmospheric "fog," the abruptness of the flux increase will be governed by the time scale associated with the phase change.

Additional observations of a day-night asymmetry in infrared emission have been obtained from the Venera 9 and 10 orbiters (Ksanfomality et al., 1976). The on-board radiometers covered the 8-30 μm bandpass and the observations included the equatorial regions of Venus. A day-night effect was observed across the evening terminator with nighttime brightness temperatures of about 244°K and daytime temperatures near 234°K. This asymmetry is consistent with the results of ground-based observations, although the magnitude of the nighttime flux excess is somewhat larger than has been supposed from ground-based measurements. Perhaps the difference between the ground-based and spacecraft results is due to the different spectral bandpasses as well as to the variability in the day-night thermal contrast as discussed above. Unfortunately, the Venera 9 and 10 observations did not include the region near the morning terminator; however, Ksanfomality et al. hypothesize that the morning and evening terminators should be similar in appearance. The results of Murray et al. (1963), Westphal et al. (1965), and the preceding discussion indicate that this is not the case. Further observations of the twilight regions of Venus, in both the infrared and ultraviolet, will hopefully bring to light the mechanisms responsible for the observed asymmetries and elucidate the differences in structure or dynamics which give rise to the observed evening-morning disparity.

Section 2. Equatorial limb-darkening

This section discusses equatorial limb-darkening profiles in order to derive information regarding the thermal structure of the Venus upper atmosphere.

The formal relation between intensity as a function of viewing angle cosine, μ, and wavelength, λ, is given by the integral expression of the equation of transfer for a semi-infinite atmosphere

$$B_\lambda(\mu) = \int_0^\infty J_\lambda(\tau_\lambda) e^{-\tau_\lambda/\mu} \frac{d\tau_\lambda}{\mu} \tag{4}$$

where $J_\lambda(\tau_\lambda)$ is the radiation source function at optical depth τ_λ. Thus $B_\lambda(\mu)$, which is the measured quantity, is related to the Laplace transform of the function J_λ. In those instances in which scattering is negligible, the source function is purely thermal, i.e., $J_\lambda(\tau_\lambda) = \mathscr{B}_\lambda(T)$, where $\mathscr{B}$ is the Planck blackbody function, which depends only on the ambient temperature and the wavelength of interest. Solution of equation (4) for $J_\lambda(\tau_\lambda) = \mathscr{B}_\lambda(T)$ translates readily into $T(\tau_\lambda)$, that is, temperature as a function of optical depth for a given wavelength. If further information is available which provides temperature as a function of height, $T(z)$, then $\tau_\lambda(z)$ may be obtained. Given data regarding chemical composition of the opacity sources, and since τ_λ is defined as

$$\tau_\lambda(z) = \int_z^\infty k_\lambda(z)\, N(z)\, dz \tag{5}$$

where k_λ = extinction cross section and N = number density, then one can obtain information regarding extinction and density vs. height in the atmosphere.

One of the simplest methods by which equation (4) may be solved is by direct inversion of an analytic function which fits B_λ to the level of the uncertainty in the measurements. Unfortunately, this inversion requires knowledge of $B_\lambda(\mu)$ over the entire range of μ, particularly since the information obtained at high viewing angles is generally most diagnostic for the evaluation of radiation source functions from remote sensing measurements. Nevertheless, the information contained in limb-darkening at $\mu > 0.5$, the observational limit in this study, may be used to evaluate atmospheric models. This section discusses the equatorial limb-darkening in the 8-20 μm region and shows that it is independent of wavelength. A simple atmospheric model will be considered in an effort to demonstrate the conditions under which this observation may be reproduced. In addition, the discussion of equatorial limb-darkening will serve as a prelude to the next section, in which it is shown that the spectral dependence of the polar limb-darkening is significantly different from the behavior in the equatorial regions.

The equatorial limb-darkening curves obtained in the analysis described in the preceding section are expressed as third order polynomials

$$\frac{B(\mu)}{B(1)} = 1 + a(\mu-1) + b(\mu^2-1) + c(\mu^3-1) \qquad (6)$$

where B(1) is the intensity of the center of the disk and a, b, and c are presented in Table III for the narrowband 8.7, 9.5, 11.2, 12.5, 18.3, and 19.8 μm channels as well as for the broadband 8-14 μm channel. Most of the data points in these narrowband channels are from images obtained after inferior conjunction, when the atmosphere is fairly symmetric east-west along the equator. Thus, the limb-darkening is not strongly influenced by the day-night asymmetry in the vicinity of the evening terminator.

Since no absolute photometric calibrations of the data were obtained, it will be necessary to adopt some value of absolute brightness temperature for the disk center. The value of 235°K will be chosen, consistent with the results of the Venera 9 and 10 and Mariner 10 infrared radiometer measurements (Ksanfomality, 1976; Chase et al., 1974; Taylor, 1975). This value implies that unit optical depth occurs in the 10-50 mbar region, assuming the Mariner 5 and 10 radio occultation profiles (Fjeldbo et al., 1971; Howard et al., 1974; Nicholson and Muhleman, 1977). CO_2 is a minor source of opacity in the 8-14 μm and 18-20 μm regions at such pressures, and the absence of sharp absorption or emission features suggests that the dominant source of opacity is particulate rather than gaseous in nature. There is a fair amount of evidence that concentrated solutions of

Table III

Infrared equatorial limb-darkening parameters for the model $B(\mu)/B(1) = 1 + a(\mu - 1) + b(\mu^2 - 1) + c(\mu^3 - 1)$. The model is reliable for $\mu \geq 0.5$ and the uncertainty in $B(\mu)/B(1)$ is $\pm$ 0.02 in the 8-14 μm region and $\pm$ 0.03 in the 18-20 μm region for $\mu = 0.5$, where this error is largest.

λ	a	b	c
8.7 μm	0.609	0.410	-0.369
9.5 μm	2.259	-1.770	0.556
11.2 μm	1.516	-0.899	0.163
12.5 μm	1.436	-0.849	0.143
8-14 μm	0.875	-0.129	-0.119
18.3 μm	1.320	-0.709	0.040
19.8 μm	3.263	-3.485	1.307

H_2SO_4 comprise the major constituent of the clouds at these levels (Hansen and Hovenier, 1974; Young, 1973; Sill, 1972; Pollack et al., 1974; Martonchik, 1974), and that these clouds are poor infrared scatterers such that the source function may be approximated by the Planck blackbody function (Samuelson et al., 1975). In this case, the relation between intensity contrast and brightness temperature difference is given by

$$\frac{\Delta B_\lambda}{B_\lambda} \cong \frac{hc}{\lambda k T_\lambda} \frac{\Delta T_\lambda}{T_\lambda} \tag{7}$$

where h = Planck's constant, k = Boltzmann's constant, and c = speed of light. The following discussion is concerned with the derivation of relative temperature contrasts, rather than absolute values; thus the choice of 235°K as the absolute brightness temperature is not too critical and it may be seen from equation (7) that the use of a value 10°K higher or lower will not significantly affect the conclusions. Furthermore, although the use of a constant value throughout the 8-14 and 18-20 μm regions is not strictly consistent with the spectral dependence of brightness temperature at these wavelengths (Gillett et al., 1968; Samuelson et al., 1975; Aumann and Orton, 1977), the fact that only relative temperature variations are to be considered renders this a useful, as well as valid, approximation.

A convenient parameterization of the limb-darkening is the brightness temperature difference between the disk center and the

point where $\mu = 0.5$, i.e., $T_\lambda(1) - T_\lambda(.5)$. Using the limb-darkening coefficients in Table III to calculate $[B_\lambda(1) - B_\lambda(.5)]/B_\lambda(1)$, and letting $T_\lambda = 235°K$, one can calculate $T_\lambda(1) - T_\lambda(.5)$ for each wavelength channel. These values are shown in Table IV. Note that this parameter is nearly independent of wavelength, with an average value of about 10.6°K. This result is consistent with any cloud model in which the absorption and scattering properties are wavelength independent. Photometric and spectroscopic measurements of Venus brightness temperature in the 8-20 μm region (Gillett et al., 1968; Samuelson et al., 1975; Aumann and Orton, 1977) and laboratory measurements of the optical properties of H_2SO_4 solutions (Palmer and Williams, 1975) indicate, however, that the Venus clouds are not grey, such that this simple class of models can be ruled out. On the other hand, a cloud model in which 1) the number density of the absorbing aerosol falls off exponentially with altitude and 2) the particle scale height and temperature lapse rate are constant over the range of altitudes sensed in the different wavelength channels also predicts wavelength independent limb-darkening, even though the extinction cross section, k_λ, may not be spectrally invariant. The following discussion is a demonstration of the validity of this assertion. The implications of this model with respect to scale height and lapse rate are also presented, and a comparison is made with the results of spacecraft radio occultation experiments.

Table IV

Equatorial center-to-limb brightness temperature differences

λ	$[T_\lambda(1) - T_\lambda(.5)]$ (°K)
8.7 μm	9.7 ± 0.7
9.5 μm	10.6 ± 0.8
11.2 μm	9.9 ± 0.9
12.5 μm	10.1 ± 1.0
8-14 μm	10.1 ± 1.0
18.3 μm	11.2 ± 2.1
19.8 μm	12.1 ± 2.4

Exponentially distributed aerosol

In this model an exponential distribution of the absorbing aerosol is assumed. The dependence of particle number density, N, on altitude, z, may be written $N = N_o e^{-(z-z_o)/H}$, where N_o is the particle number density at an altitude z_o which is below the levels sensed in the infrared and H is the aerosol scale height. Assuming that k_λ and H do not vary with altitude, then from equation (5) it follows that

$$\tau_\lambda(z) = Hk_\lambda N_o e^{-(z-z_o)/H} \quad . \tag{8}$$

The atmospheric transmission, $\mathscr{T}_\lambda$, above a given altitude z is given by

$$\mathscr{T}_\lambda (z,\mu) = e^{-\tau_\lambda(z)/\mu} \quad . \tag{9}$$

Neglecting scattering, it follows from equation (4) that

$$B_\lambda(\mu) = \int_o^\infty \mathscr{B}_\lambda(z)\, K_\lambda(z,\mu)dz \tag{10}$$

where $K_\lambda (z,\mu) = d\mathscr{T}_\lambda/dz$ and is called the radiative transfer weighting function. Equation (10) implies that the measured intensity at a given viewing angle is a weighted average of brightness of each level in the atmosphere. In this model, the contribution of $\mathscr{B}_\lambda(z)K_\lambda(z,\mu)$ becomes negligible at a certain altitude and depth and thus the integration in equation (10) can be finitely bounded. Combining equations (8) and (9), it is seen that

$$K_\lambda(z,\mu) = \exp\left[\frac{-Hk_\lambda N_o}{\mu}\, e^{-(z-z_o)/H}\right] \frac{k_\lambda N_o}{\mu}\, e^{-(z-z_o)/H} \quad . \qquad (11)$$

This function has a local maximum such that certain levels will be the most significant contributors to the observed intensity.

The model atmosphere is broken into horizontal layers of 0.5 km vertical thickness and each layer is assumed to be isothermal over its extent. $\mathscr{B}_\lambda$ for a particular layer and spectral channel is calculated from

$$\mathscr{B}_\lambda(z) = \sum_{j=1}^{n} \frac{2hc^2}{\lambda_j^5} \frac{f_j(\lambda_j)}{e^{hc/\lambda_j kT}-1} \qquad (12)$$

where $f_j(\lambda_j)$ is the normalized filter transmission function for a particular channel evaluated at n discrete points in the bandpass. $K_\lambda(z,\mu)$ is calculated from equation (11), and equation (10) is numerically integrated to yield $B_\lambda(\mu)$. The temperature at the cloud base, $T_o = T(z_o)$, is arbitrarily fixed at 270°K and the lapse rate, $\Gamma = dT/dz$, is assumed constant such that $T(z) = T_o + \Gamma(z-z_o)$.

The essential characteristics of the model are brought to light by using a simplifying approximation in which it is assumed that the observed radiation emanates from a single "effective" level of emission, rather than being a weighted sum of contributions from an extended vertical region. In other words, this "single level" approximation defines $B_\lambda(\mu) = \mathscr{B}_\lambda[z'(\mu)]$, where z' is the "effective"

altitude at which the blackbody intensity corresponding to the ambient temperature at z' is equal to the observed brightness. Letting τ_λ^* denote the constant slant optical path length between the level $z'(\mu)$ and the observer, and letting τ_λ' equal the vertical optical depth above z', then it follows that

$$\tau_\lambda' = \mu \tau_\lambda^* \quad . \tag{13}$$

Combining equations (8) and (13), one obtains

$$\tau_\lambda^* = \frac{Hk_\lambda N_o}{\mu} \quad e^{-(z'-z_o)/H} = \text{constant.} \tag{14}$$

Solving this equation for the dependence of z' on μ, and remembering that $T' = T_o + \Gamma(z'-z_o)$, then it follows from the "single level" approximation that the observed brightness temperature distribution will be given by

$$T_\lambda(\mu) = T_o + \Gamma H \ell n \frac{Hk_\lambda N_o}{\mu \tau_\lambda^*} \quad . \tag{15}$$

In order to make use of this approximation, it will be necessary to show that it yields limb-darkening profiles similar to those obtained by using the actual form for $K_\lambda(z,\mu)$ and integrating equation (10). Table V demonstrates the validity of this "single level" approximation for the 8.7 μm channel, and presents the results obtained by converting $B_\lambda(\mu)$ in equation (10) to equivalent brightness temperatures compared to the results obtained by using the "single level"

Table V

Comparison of 8.7 μm brightness temperatures calculated from integration of the equation of transfer and from the "single level" approximation in which radiation is assumed to emanate from the $\tau_\lambda^* = 0.73$ level only. The cloud model parameters are: $k_\lambda N_o = 1.5 \times 10^{-5}$ cm^{-1}, H = 4.5 km, $\Gamma = -3.3$°K/km, $T_o = 270$°K.

μ	$T_{rad.\ transf.}$ (°K)	$T_{approx.}$ (°K)
1.0	234.9	235.1
0.9	233.4	233.5
0.8	231.7	231.7
0.7	229.8	229.7
0.6	227.6	227.4
0.5	225.0	224.7

approximation. The parameters were chosen for this example so as to yield a disk center brightness temperature of ~235°K and a center-to-limb brightness temperature difference consistent with the observations. The following values were used: $k_\lambda N_o = 1.5 \times 10^{-5}$ cm^{-1}, H = 4.5 km, Γ = -3.3°K/km, T_o = 270°K, and the agreement shown in Table V was obtained by letting $\tau_\lambda^* = 0.73$.

Making use of the "single level" approximation, it follows from equation (15) that the difference in brightness temperature between the center of the disk and the location where $\mu = 0.5$ is given by

$$T_\lambda(1) - T_\lambda(.5) = -\Gamma H \ell n 2 \quad . \tag{16}$$

This equation implies that the observational data are sensitive to the product of Γ and H, and predicts $T_\lambda(1) - T_\lambda(.5)$ to be independent of wavelength, in agreement with the observations shown in Table IV. Adopting a value of 4.5 km for the scale height, H, which is roughly the atmospheric scale height implied by the Mariner 5 and 10 radio occultation experiments (Fjeldbo et al., 1971; Howard et al., 1974; Nicholson and Muhleman, 1977), or in other words, assuming that the aerosol and gas are homogeneously mixed, the average value of $T_\lambda(1) - T_\lambda(.5) = 10.6$°K translates into a lapse rate, Γ, of slightly greater than -3°K/km. This number falls between the values of -2.5 and -4°K/km determined from the two Mariner radio occultation experiments. On the other hand, if a value of 2 km is chosen for the aerosol scale height, which is closer to the value determined from

Mariner 10 limb photographs (O'Leary, 1974b), the infrared observations imply a lapse rate of nearly -8°K/km. However, the limb photographs are sensitive to levels where the pressure is a few millibars, and therefore roughly 10 km above the regions to which the infrared measurements are sensitive. Thus, if an exponentially distributed haze is a reasonable approximation to the Venus cloud structure in the 10-50 mbar region, then the limb-darkening and radio occultation measurements are mutually consistent with a model in which the aerosol/gas abundance ratio is independent of altitude, the scale height is on the order of 4.5 km, and the lapse rate is roughly -3°K/km.

In addition to spatially resolved limb-darkening measurements of the type presented here, another critical test of atmospheric models is conclusive determination of the spectral variation in absolute brightness temperature from 10 to 20 μm. Recent C-141 airborne observations (Aumann and Orton, 1977) indicate that 20 μm brightness temperatures are roughly equivalent to the 10 μm values; on the other hand, ground-based observations (Kunde, 1976) indicate that Venus is roughly 30°K warmer at 20 μm than at 10 μm. Clearly, since the combination of spatially and spectrally resolved observations provides a valuable basis for the development of atmospheric models, resolution of this controversy is vital for a better understanding of not only the spectral nature of IR opacity but the vertical distribution of clouds in Venus' upper atmosphere as well.

Section 3. Polar limb-darkening

One of the observations made by Murray et al. (1963) and Westphal et al. (1965) and confirmed by the analysis of Ingersoll and Orton (1974) was enhanced limb-darkening in the polar directions compared with the equatorial center-to-limb variation. This effect may be seen in Figure 3c of Section 4, in which the poles appear dark relative to the equator and tropics after contrast enhancement. Analysis of Mariner 10 ultraviolet images (Suomi, 1974) indicates primarily zonal transport in the upper atmosphere, and little net motion in the meridional directions. Thus, one may expect that the meridional insolation variation, in which less energy is deposited in the polar regions relative to the equator, will, in radiative equilibrium, be reflected in enhanced poleward infrared limb-darkening. This picture is complicated by the possibility of significant meridional transport of sensible or latent heat below the UV and IR clouds, and the fact that the 8-14 μm region represents only about one-third of the net infrared emission from Venus. Therefore, information regarding the heat budget of the Venus atmosphere requires greater spectral coverage than is presently available, but the spectral dependence of 8-20 μm polar limb-darkening does contain information relevant to the spatial distribution of opacity sources effective at these wavelengths.

It was shown in the previous section that the temperature difference between the disk center and the location where $\mu = 0.5$ on the

equator is practically wavelength independent from 8 to 20 μm. Table VI shows the parameter $T_\lambda(1) - T_\lambda(.5)$ for each of the wavelength channels, where in this case $T_\lambda(.5)$ refers to a point on the polar axis in the southern hemisphere. The data are shown for UT 26 September 1975 and UT 22 October 1975. As will be shown in the next section, the north polar region contained an infrared anomaly on these dates, whereas the south pole was more uniform in appearance. Thus, the temperature difference between the disk center and southern limb should be representative of the state of the atmosphere when no anomalous feature is present. It may be seen in Table VI, in contrast with the results obtained in the last section, that the center-to-limb variation in brightness temperature is strongly wavelength dependent in the polar direction. Note that the temperature contrast at 8.7 μm is lower than that obtained in the equatorial direction; at 9.5 μm is comparable in magnitude; and at all other wavelengths is significantly greater. The simplest explanation of this observation is that the optical properties of the atmosphere are latitude and wavelength dependent, that is, that at 8.7 μm the polar regions are less opaque than the equator, and become more opaque longward of 9.5 μm. This change in opacity therefore enhances or detracts from the basic temperature contrast due to the atmospheric temperature lapse rate. Particles which are on the order of 20 - 30 μm in radius would appear more opaque to the longer wavelength IR radiation

Table VI

Polar center-to-limb brightness temperature differences (S pole)

	$[T_\lambda(1) - T_\lambda(.5)]$ (°K)	
λ	UT 26 Sept 1975	UT 22 Oct 1975
8.7 μm	7.3 ± 1.2	7.7 ± 1.2
9.5 μm	9.5 ± 1.2	9.5 ± 1.2
11.2 μm	15.5 ± 1.6	15.5 ± 1.2
12.5 μm	16.3 ± 2.0	18.2 ± 2.0
8-14 μm	11.8 ± 1.5	12.7 ± 1.6
18.3 μm	------	16.9 ± 2.5
19.8 μm	------	22.0 ± 3.0

and thus a greater abundance of such particles in the polar regions relative to the low latitudes might be capable of explaining the observed spectral variation in $T_\lambda(1) - T_\lambda(.5)$. A comparison of the angular distribution of polarization at visible wavelengths of the equatorial versus polar regions may be one possible method of testing this hypothesis. In particular, an increase in polarization at a scattering angle of 90° is diagnostic of an increase in particle size for particles larger than the wavelength (Hansen and Travis, 1974).

Section 4. The infrared polar anomalies

As discussed in Chapter 1, the infrared maps of Murray et al. (1963) showed the presence of a cold thermal anomaly located near the south pole of Venus. A nearly identical type of feature was observed near the south pole in 1974 in the 8-14 μm and narrowband 8.7, 9.5, and 11.2 μm images obtained by Diner et al. (1976) on UT 6 March of that year. Figure 3a is a composite of three unprocessed 8-14 μm images obtained on this date. As described in Chapter 3, this composite was noisy due to a drift in the detector, and a smoothing filter was applied to the data. The result of this filtering and division of the image by an axisymmetric cosine surface to remove some global shading is shown in Figure 3b. Figure 3c is similar to Figure 3b except that the contrast has been enhanced by a factor of four with a linear stretch.

Figure 3a (left). Composite of three unprocessed 8-14 μm images obtained on the morning of UT 6 March 1974. Celestial north is at the top; east is at the left.

Figure 3b (center). Image processed version of Figure 3a. The image has been filtered and partially corrected for global shading as described in Chapter 3. A south polar "cap," dark "collar," and light and dark "bands" are visible.

Figure 3c (right). Same as Figure 3b except the contrast has been enhanced. The polar limb-darkening is more severe than the equatorial darkening. The bright region on the east (sunlit) limb indicates higher brightness temperatures relative to the west limb.

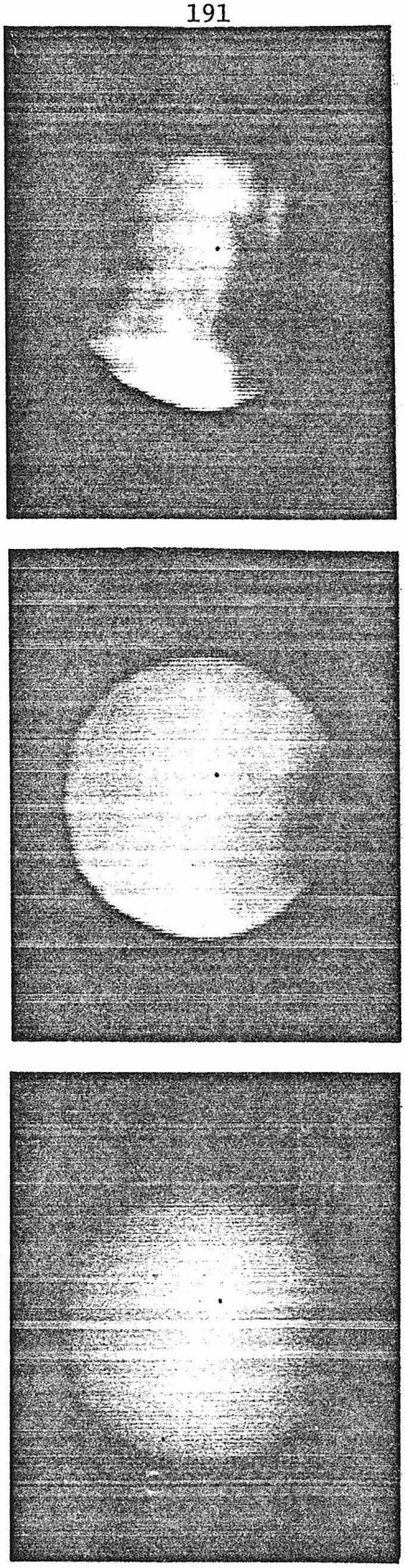

Figs. 3a, 3b, 3c

Several interesting features may be seen in the pictures: a bright south polar "cap," and broad dark "collar" surrounding the cap, and suggestions of light and dark banding at intermediate southern latitudes. The "bands" are difficult to see in the unprocessed images but show up more clearly in the processed version.

Figure 4 shows several consecutive north-south scans taken from the averaged picture (Figure 3a). Flux variations in individual scans are identified with corresponding features in the images. The data bear a strong resemblance to scans obtained by Murray et al. (1963). In particular, the brightening near the south pole appears in both sets of data. Comparison of the southern hemisphere data with flux levels in the north suggests that the polar "brightening" is not a flux enhancement but rather that adjacent regions are flux deficient; that is, the anomaly is not the "cap," but the "collar." It is possible to obtain an estimate of the magnitude of this flux deficiency by measuring the flux in the south where the collar attains minimum brightness and comparing this value with the flux at a similar viewing geometry in the north. In other words, a parameter $(\Delta B/B)_{\text{anomaly}}$ can be defined, where

$$\left(\frac{\Delta B}{B}\right)_{\text{anomaly}} = \frac{B_{\text{normal pole}}(\mu^*) - B_{\text{anomalous pole}}(\mu^*)}{B_{\text{normal pole}}(\mu^*)} \qquad (17)$$

Figure 4. Comparison of three consecutive north-south scans from the composite 8-14 μm image of Figure 3a, showing reproducibility of the data. Light and dark features visible in the 8-14 μm image are identified in these individual scans. The numbers represent the percentage contrast in brightness between adjacent regions. (After Diner et al., 1976).

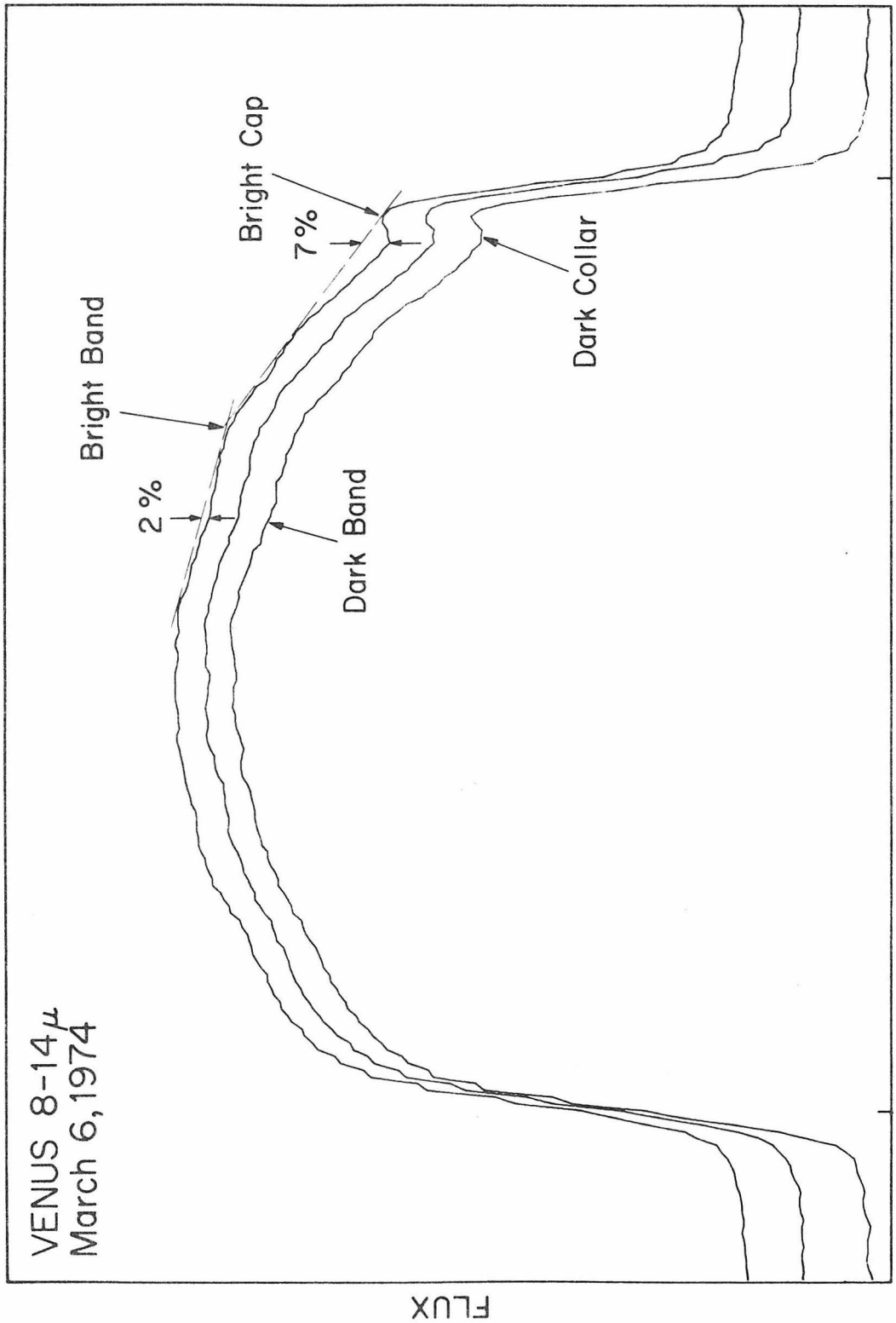
VENUS 8-14μ
March 6,1974
Bright Band
2 %
Dark Band
Bright Cap
7 %
Dark Collar
NORTH LIMB
SOUTH LIMB
FLUX

Fig. 4

in which $B(\mu)$ is the brightness of a point where the cosine of the angle between the direction to the observer and the local normal = μ; μ^* is the specific value of μ attained where the collar is darkest. For the data shown in Figure 4, $(\Delta B/B)_{anomaly} = 0.18$. This contrast may be expressed as an equivalent brightness temperature difference by virtue of equation (7) in Section 2; thus, the collar represents a temperature anomaly of approximately 7°K below "normal" (i.e., the northern hemisphere value). It may also be seen that adjacent light and dark areas represent flux differences on the order of 2-7% or about 1-3°K in brightness temperature.

It has been pointed out that the infrared measurements are sensitive to the 10-50 mbar level in the Venus atmosphere, and that particulates constitute the major sources of opacity. The light and dark features in the infrared images might therefore be attributed, in the presence of the known temperature gradient, to variations in: 1) the height of a cloud "top;" 2) the particle number density; 3) the particle size; or 4) the chemical composition of the aerosol. These parameters influence the opacity of the haze and therefore affect the level at which unit optical depth is reached. Using a value of -3°K/km for the lapse rate as derived in Section 2, brightness temperature variations of several degrees imply differences in the level of unit optical depth of on the order of 1 km. Another interpretation of the infrared features is that they are due to

lateral temperature fluctuations at an isobaric level or lateral variations in the emissivity of the radiating "surface." Later discussion will attempt to resolve these ambiguities.

Published data on the appearance of infrared polar anomalies during the 1962 and 1974 apparitions suggested that this type of feature formed preferentially near the south pole (Murray et al, 1963; Diner et al, 1976). However, the data obtained during the 1975 apparition negated this supposition and clearly revealed the presence of such a feature in the north polar region. One possible explanation for the appearance of the anomaly at only one pole (and not consistently the same one) is that the planet is actually symmetric north-south (i.e., a similar anomaly exists at both poles simultaneously) but that an apparent asymmetry arises from a geometry in which one pole is tilted toward the Earth due to the inclination of Venus' rotational or orbital axis. Carpenter (1970) has published a summary of radar determinations of the right ascension and declination (α_p, δ_p) of the Venus south rotational pole as well as the position of the south orbital pole. These coordinates are presented in Table VII. From these values a unit vector $\hat{p}$ = ($\cos \delta_p \cos \alpha_p$, $\cos \delta_p \sin \alpha_p$, $\sin \delta_p$) describing the direction of the south pole in the celestial sphere may be calculated. Taking the position of Venus on any given date from the American Ephemeris and Nautical Almanac, the direction of Venus in the sky as seen from

Table VII

Coordinates of Venus orbit S pole and radar determinations of rotation S pole

Pole	α_p (degrees)	δ_p (degrees)
Orbit S pole (OSP)	97.01	-65.55
Carpenter (1970) radar rotation S pole (RRSP)	94	-71.5
Dyce, Pettengill, and Shapiro (1967) RRSP	90.0	-66.4
Goldstein (1966) RRSP	98	-69
Shapiro (1967) RRSP	84.7	-65.8

Latitude of sub-Earth point on dates when infrared polar anomalies were observed

	Latitude sub-Earth point		
Assumed Pole	Dec. 1962 (anomaly in S)	Mar. 1974(S)	Sept.1975(N)
OSP	1.4°S	7.2°S	8.1°N
Carpenter (1970) RRSP	1.6°N	1.4°S	3.6°N
Dyce, Pettengill, and Shapiro (1967) RRSP	2.7°S	5.2°S	5.6°N
Goldstein (1966) RRSP	1.1°N	4.2°S	6.2°N
Shapiro (1967) RRSP	4.8°S	4.3°S	3.8°N
Average of 4 radar measurements	1.2°S	3.8°S	4.8°N

the Earth is $\hat{r} = (\cos \delta_v \cos \alpha_v, \cos \delta_v \sin \alpha_v, \sin \delta_v)$ where α_v and δ_v are the right ascension and declination of Venus, respectively. Adopting the convention that latitudes in Venus' northern hemisphere shall be positive, the latitude of the sub-Earth point on Venus, and therefore the number of degrees the polar axis is tipped toward or away from the Earth, is given simply by

$$\text{Latitude sub-Earth point} = \arccos [\hat{p} \cdot (-\hat{r})] - 90° \ . \qquad (18)$$

The results of using each of the assumed poles and performing the calculations for dates on which the dark collar and bright cap were observed at 8-14 μm are also summarized in Table VII, along with a notation indicating the pole at which the feature was prominent. It may be seen that the numbers suggest slight tilts of the poles in the correct directions toward the Earth on these dates, but since the polar anomalies extend over many tens of degrees of latitude, the magnitudes of the tilts are far too small to explain the north-south asymmetry. Possibly the anomalies are manifestations of instabilities in the lower atmosphere; future monitoring of their positions will improve the observational statistics and may give some clues as to their preferred locations.

The infrared polar anomaly seen in 1962 by Murray et al. (1963) in post-inferior conjunction data was not observed in the pre-inferior conjunction maps of Westphal et al. (1965) obtained in 1964. North-

south infrared scans obtained in later years by Westphal (1975) imply that this was not a chance occurrence and instead indicate that such polar anomalies appear preferentially on Venus' morning side (that is, in data obtained after inferior conjunction). Pre- and post-inferior conjunction data obtained during the 1975 apparition support the conclusion that the appearance of IR polar anomalies is biased toward the morning hours. The following discussion includes a presentation of the 1975 data and a few speculations upon some possible explanations of this observation.

The presence of a cold anomaly at one of the poles may be parameterized by definition of a parameter

$$\frac{B_{pole}}{B_{center}} = \frac{B(\mu = .5)}{B(\mu = 1)} \tag{19}$$

for each of the poles. This parameter measures the contrast between the flux at the disk center (where $\mu = 1$) and the flux 87% of the distance to the limb at a latitude of 60° (where $\mu = 0.5$). A more pronounced flux depression within the collar at one pole yields a smaller value of this parameter for that pole and a greater difference between the values characterizing the two poles. For example, for the data of UT 26 September 1975, when a prominent north polar anomaly was observed, the values at 8-14 μm are:

$$\frac{B_{pole}}{B_{center}} = 0.51 \text{ (N pole)}; \quad \frac{B_{pole}}{B_{center}} = 0.69 \text{ (S pole)}.$$

Figure 5 is a plot of this parameter vs. solar phase angle for both poles. The data are taken from 8-14 μm images obtained during the 1975 apparition. Several points may be made about this plot. First, the value of the polar darkening parameter defined in equation (19) is relatively constant for the south pole, with an average value of 0.71. Second, the north-south asymmetry and presence of a north polar collar are clearly skewed toward dates following inferior conjunction. Third, the images of UT 1 August and 26 September were obtained at similar phase angles, at similar Earth-Venus distances and with similar seeing (such that they have comparable spatial resolution), but the north-south asymmetry is clearly greater in the image of 26 September. Fourth, the contrast between north and south is greatest during early morning, and diminishes toward dawn. It might be suggested that this diminution in the prominence of the northern polar anomaly is attributable to the increase in Earth-Venus distance as the planet recedes, such that the feature's disappearance is due to the resulting degradation in spatial resolution. However, this degradation should affect the north and south limbs similarly, and no such effect is seen for the south pole. Finally, it should be mentioned that daily observations of polar anomalies demonstrate the persistence of such features on a day-to-day basis. This implies that the temporal variability in north-south asymmetry shown in Figure 5 is part of a gradual trend, rather than a sampling of random

Figure 5. Plot of the parameter B_{pole}/B_{center} on the illumination axis for the north and south poles vs. the solar phase angle of the image from which the data were taken. The data are at 8-14 μm and from the 1975 apparition. The magnitude of the difference in the values for the north and south poles indicates the strength of the north polar anomaly observed in 1975.

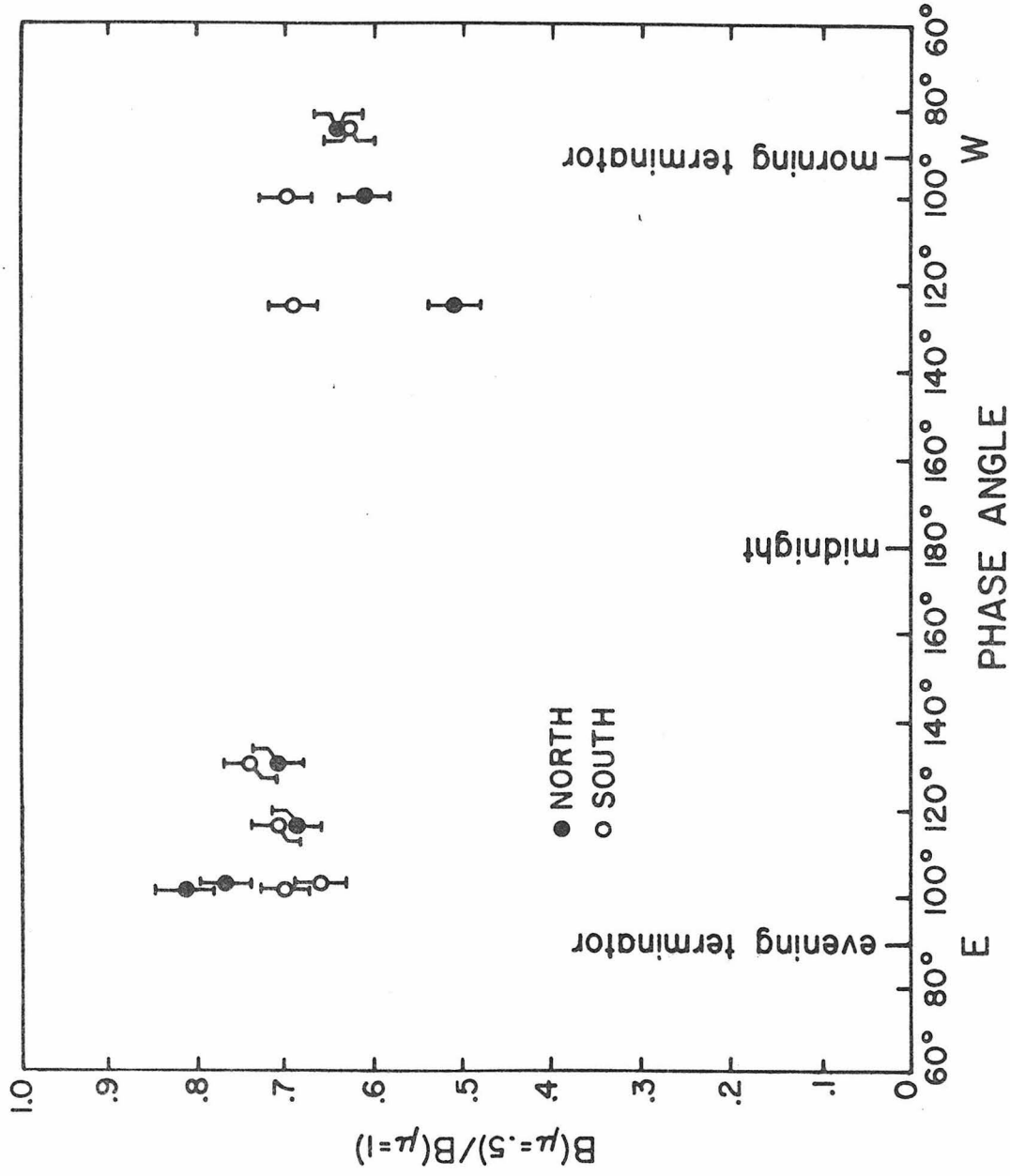
B(μ=.5)/B(μ=1)
1.0
.9
.8
.7
.6
.5
.4
.3
.2
.1
0
60° 80° 100° 120° 140° 160° 180° 160° 140° 120° 100° 80° 60°
E
evening terminator
midnight
morning terminator
W
PHASE ANGLE
● NORTH
o SOUTH

Fig. 5

fluctuations in the thermal emission from the poles on a time scale shorter than the hiatus between consecutive observing periods.

A later section discusses the correlation of simultaneous ultraviolet and infrared images. The results of this comparison show that certain infrared features, including the polar anomaly, are evident as cloud markings in reflected sunlight. This observation implies that the infrared features are attributable to variable cloud opacity, rather than thermal contrast on isobaric levels. The cold polar anomaly may therefore be associated with a particularly high or dense cloud. The observation that the anomaly appears well after sunset on Venus suggests that it might be a cloud which condenses after the atmosphere has cooled sufficiently during nighttime. An alternative suggestion is that the temporal variations in the polar anomaly are due to a cloud deck which gradually rises and sinks. The vertical velocity of any such motion may be determined from the following calculations: The data of UT 26 September 1975 and UT 15 November 1975 differ on the central meridian by 41° of longitude. Assuming a radius of 6052 km for Venus and an altitude of 75 km above the surface, this represents a distance of 2192 km at a latitude of 60°. Mariner 10 UV photographs (Murray et al., 1974; Suomi, 1974) show an apparent zonal velocity at this latitude of roughly 60 m/sec. Thus the rotation through 41° of longitude would take 3.65×10^4 sec. The contrast between the north and south poles at $\mu = 0.5$. i.e., $(\Delta B/B)_{anomaly}$

as defined in equation (17) (replacing μ^* by $\mu = 0.5$) decreases from 0.2 to 0 over this time period. Therefore, the temperature of the north polar anomaly increases by about 8°K on the central meridian from 26 September to 15 November. Adopting an approximate lapse rate of -3°K/km, this temperature increase corresponds to a cloud deck altitude drop of 2.7 km. Thus, if the early morning disappearance of the polar anomaly observed in 1975 is due to the gradual sinking of a polar cloud, the average vertical velocity is on the order of 7 cm/sec for the sinking motion. Analysis of the Venus circulation from Mariner 10 photographs (Suomi, 1974) indicates that horizontal motion is almost entirely zonal. If there is no meridional transport of energy, the flux emitted by a zonal band averaged over a rotational period must remain constant. Since the tilts of the Venus rotational and orbital axes are small, this average value should be approximately the same for bands at equal latitudes in the northern and southern hemispheres. Since the north pole is cooler than the south during the morning, this analysis suggests that the north polar region should emit more flux than the south at other times during a solar day. The observations of 4 and 5 July, in which the north pole was slightly warmer than the south, provide some support for this conclusion, yet by 20 July the north-south contrast was virtually zero (see Figure 5). In the ascending-descending cloud deck model of the polar collar, these observations correspond to a rising motion. A calculation similar to the one presented above, using the data of 4 July and 20 July, yields a rising velocity on the order of 10 cm/sec.

Additional information on the nature of the cold polar features is obtained from measurements of the spectral dependence of the flux anomaly. Table VIII presents north-south contrast [the parameter $(\Delta B/B)_{anomaly}$ defined in equation (17)] at several wavelengths for two dates upon which the north polar feature was prominent (UT 26 September 1975 and UT 22 October 1975). Several remarks may be made about the results. The first point is that at the wavelengths common to the two dates, the contrast decreased in each channel from 26 September to 22 October, consistent with the variation discussed above for the broadband 8-14 μm channel. The second point concerns the wavelength dependence of the thermal contrast between the poles. The intensity contrasts are converted to brightness temperature differences using equation (7) of Section 2, and the results $\Delta T_{sn} = T_{south} - T_{north}$ for each wavelength are also shown in Table VIII. The data show that in the 8-14 μm region the temperature contrast is not wavelength dependent. However, there is considerable variation from the 10 μm to the 20 μm region and a significant difference between 18.3 and 19.8 μm is shown. This spectral behavior is inconsistent with a pure height contrast between the north and south polar clouds, because such a model predicts no wavelength dependence of ΔT_{sn}. Moreover, it is unlikely that the constancy of ΔT_{sn} in the 8-14 μm region and the fairly sharp increase in this parameter from 12.5 μm to 18.3 μm and particularly from 18.3 μm to 19.8 μm can be explained

Table VIII

North-south intensity and brightness temperature contrasts;

polar collar near N pole

λ	$(\Delta B/B)_{anomaly}$		ΔT_{sn} (°K)	
	UT 26 Sept. 1975	UT 22 Oct. 1975	UT 26 Sept. 1975	UT 22 Oct. 1975
8.7 μm	0.32 ± 0.01	0.20 ± 0.01	10.7 ± 0.4	6.7 ± 0.4
9.5 μm	0.29 ± 0.01	0.14 ± 0.01	10.6 ± 0.4	5.1 ± 0.4
11.2 μm	0.27 ± 0.01	0.14 ± 0.01	11.6 ± 0.4	6.1 ± 0.4
12.5 μm	0.24 ± 0.01	0.10 ± 0.01	11.5 ± 0.5	4.8 ± 0.5
8-14 μm	0.27 ± 0.01	0.12 ± 0.01	11.4 ± 0.4	5.1 ± 0.4
18.3 μm	------	0.15 ± 0.02	------	10.5 ± 1.4
19.8 μm	------	0.23 ± 0.03	------	17.5 ± 2.3

by particle size or number density differences between the polar clouds, unless these clouds are compositionally distinct. At present, it is probably dangerous to concentrate on any specific model of the spectral characteristics of IR polar collars, since the inference of a change in contrast from the 10 to 20 μm regions has been drawn from a limited number of images obtained on a single date of observation. Nevertheless, the observation of an invariance in ΔT_{sn} throughout the 8-14 μm region is reasonably secure. If more extensive measurements were to demonstrate that ΔT_{sn} is constant throughout the entire 8-20 μm region, as well as at other infrared wavelengths, a simple height contrast between the clouds in the north and south polar regions would constitute a viable model. On the other hand, if such measurements support the results reported here, more complicated explanations must be considered.

Section 5. Ultraviolet-infrared correlations

One of the most puzzling aspects of the Venus upper atmosphere is the presence of ultraviolet markings. These light and dark features have been photographed since the 1920's (Wright, 1927; Ross, 1928). The contrast between the light and dark markings is on the order of 30% at 3600Å and diminishes sharply toward zero at 5500Å (Coffeen, 1968). The most likely explanation is a compositional difference between two types of clouds; a model in which the

brightness contrast is attributed to differential Rayleigh scattering in CO_2 must be ruled out because it predicts a CO_2 abundance, degree of polarization, and spectral dependence of bright-dark contrast which are inconsistent with observational results (see Travis, 1975 for a review of this question).

One of the first questions one may ask regarding the UV features is: Are the bright markings high albedo clouds floating above a lower, darker cloud deck, or are the dark markings due to low albedo clouds above a bright background? Possibly neither of these views is correct and the markings arise from local increases in density of one or the other types of material. If the clouds are truly at different altitudes, one might expect to observe a greater abundance of CO_2 above the lower clouds. Young (1974) reported on the inability to find such a correlation from observations of CO_2 line strengths above isolated features, although there is marginal evidence that there is somewhat lower overall CO_2 abundance when dark markings cover most of the area of the disk. This suggests that the dark clouds are at higher altitudes (on the average), but this evidence, unfortunately, is weak.

Mariner 10 spatially resolved polarization measurements (Hapke, 1974) are indicative of greater polarization over the bright areas, and thus are consistent with a model in which the dark clouds are higher than the bright clouds, such that the differential polarization arises from a slightly greater amount of Rayleigh scattering

in CO_2 above the lower clouds. Note that ground-based observations are in dispute over this result; Fountain (1974) found lower polarization over dark areas whereas Coffeen and Hansen (1974) arrived at the opposite conclusion.

Hansen and Arking (1971) and Hansen and Hovenier (1974) have analyzed polarization measurements as a function of phase angle (Coffeen and Gehrels, 1969), and were able to fit the data with a homogeneous atmosphere composed of spherical droplets of 1.05 μm radius and having a narrow size distribution about this mean. The best-fitting value of refractive index is about 1.44 in the visible. From the degree of polarization expected from Rayleigh scattering, they were able to conclude that unit optical depth in the clouds occurs near the 50 mbar level at 3600Å. Mariner 10 UV limb photographs are consistent with the presence of atmospheric hazes in the vicinity of the 10 mbar level (Murray et al., 1974). It is therefore reasonable to adopt 10-50 mbar as the levels in the atmosphere which are observed at 3600Å. It was pointed out in Section 2 that these are the same levels from which 8-14 μm radiation is emitted. One may expect, therefore, that if the clouds giving rise to the ultraviolet markings have significant opacity in the infrared, the IR images might display features that are morphologically similar to UV markings and a correlation should be observable in the two types of data. The following discussion presents the evidence in favor of such a correlation.

The conclusion is that bright areas are generally warmer than adjacent dark regions, implying that the former are either less dense or at lower altitudes. This is consistent with the spectroscopic results of Young (1974), and the conclusions drawn by Hapke (1974) from Mariner 10 polarization data.

Figures 6 and 7 show two sets of UV-IR image pairs obtained on UT 13 and 14 February 1977. All infrared images in the following discussion were obtained with the broadband 8-14 μm filter. One of the most prominent features in the IR images is the day-night contrast; these images were obtained at eastern elongation and the evening terminator is in view. This contrast between the illuminated and dark limbs has been discussed in Section 1. The infrared images show a number of smaller scale bright and dark tilted band-like features with contrasts on the order of 1-5%. It is apparent that these features change in appearance from one day to the next. As may be seen in Figures 6 and 7, the ultraviolet images also display light and dark markings. Several other methods of displaying the data are given in the following figures. Figures 8 and 9 present contour maps of the UV and IR images in Figures 6 and 7; the contour intervals are arbitrary and were selected to give the best representation of the data. Figure 10 shows ultraviolet and infrared scans taken from the images of 14 February which slice through the same

Figure 6. (Left). Composite ultraviolet image from UT 13 February 1977. (Right). Composite 8-14 μm image obtained on the same date. Celestial north is at the top; east is at the left.

Figure 7. (Left). Composite ultraviolet image from UT 14 February 1977. (Center). Composite 8-14 μm image obtained on the same date. (Right). Enhanced version of the 8-14 μm image obtained by removing some of the global shading.

Figure 8. Contour maps of the images shown in Figure 6. The contour intervals are arbitrary. Bright features are indicated by a "B" followed by a Greek letter to distinguish individual features; dark features are similarly designated by a "D" and a Greek letter. Features in the ultraviolet and infrared maps denoted by the same symbol are in the same spatial location on the Venus disk. The bright UV regions correlate with bright areas in the 8-14 μm image and the dark UV region corresponds to a relatively dark region at 8-14 μm.

Figure 9. Same as Figure 8 for the ultraviolet and unenhanced 8-14 μm images of UT 14 February 1977.

Figure 10. Ultraviolet and 8-14 μm scans through the same region of the Venus disk on UT 14 February 1977. The bright and dark regions defined in Figure 9 are identified. The error associated with the measurements may be estimated from the magnitude of the noise in the data beyond the planetary limbs, i.e., in the sky. This uncertainty is roughly 2-3 times the thickness of the scan lines plotted in this figure.

Venus UT 13 Feb, 1977

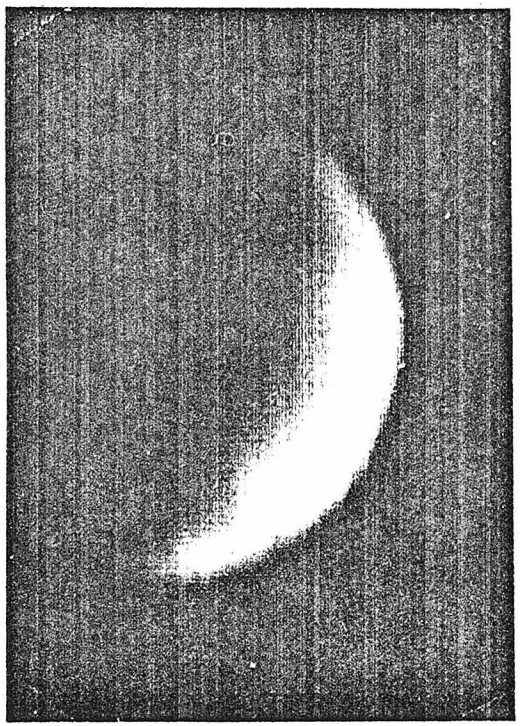

3600Å

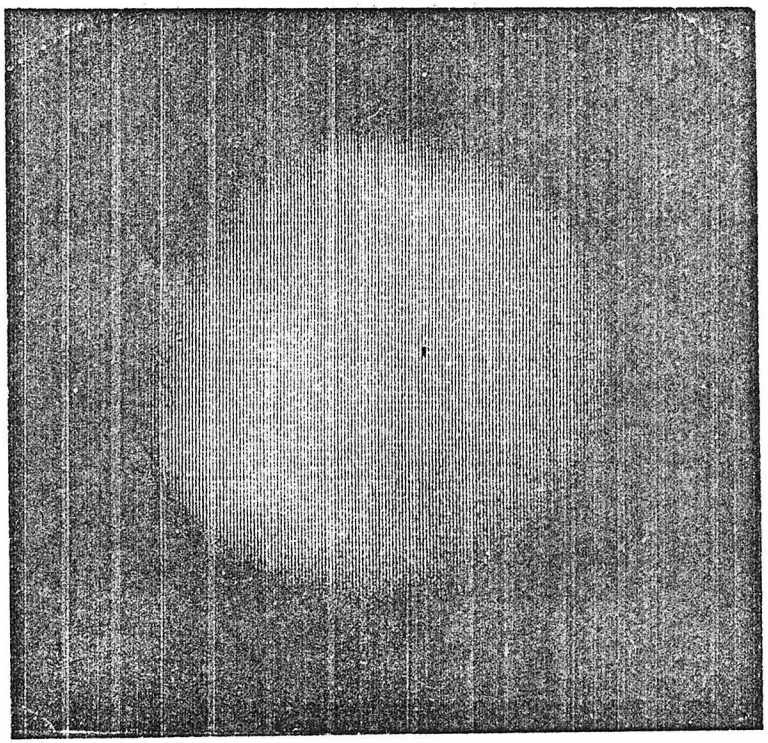

8-14 μm

Fig. 6

Venus UT 14 Feb, 1977

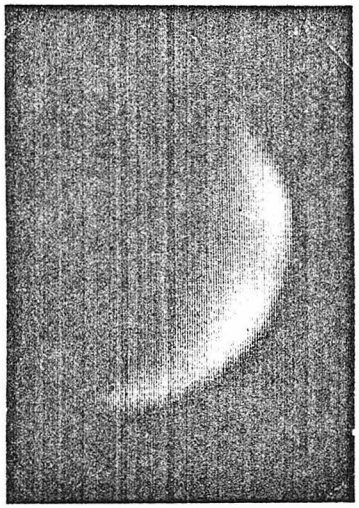

3600Å

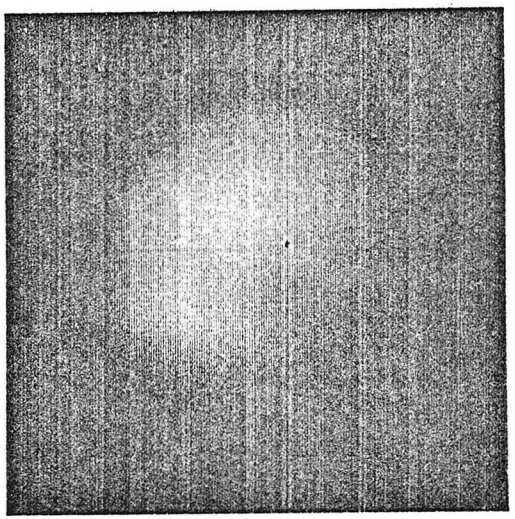

8-14μm

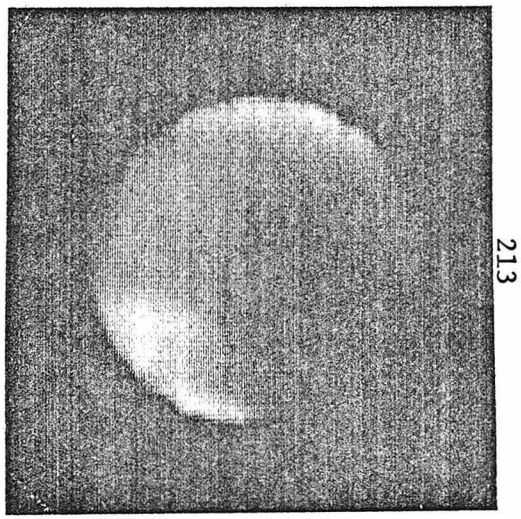

8-14μm
enhanced

Fig. 7

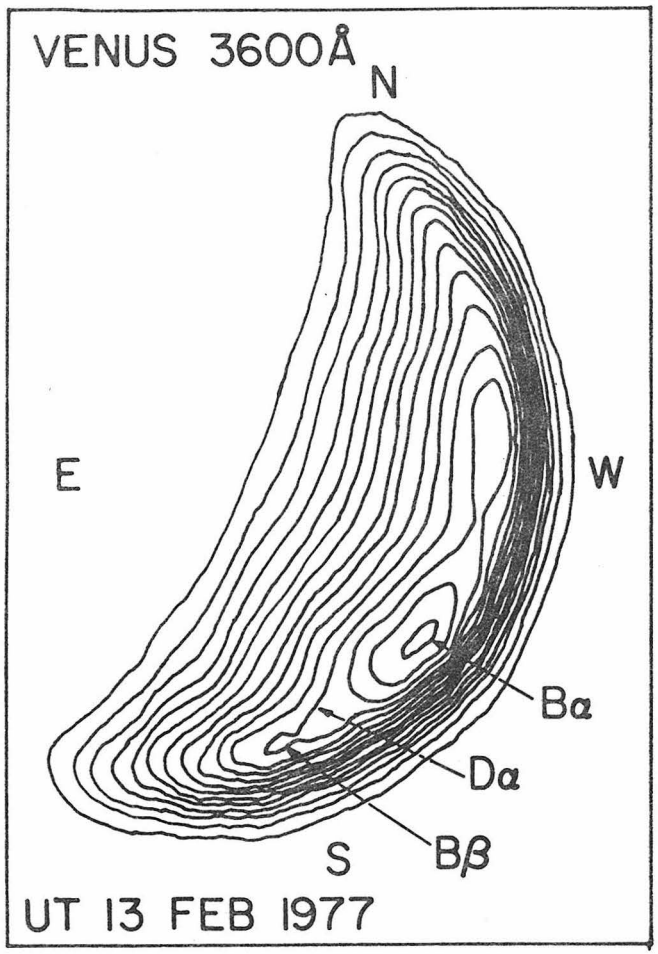
VENUS 3600Å
N
E
W
Bα
Dα
Bβ
S
UT 13 FEB 1977

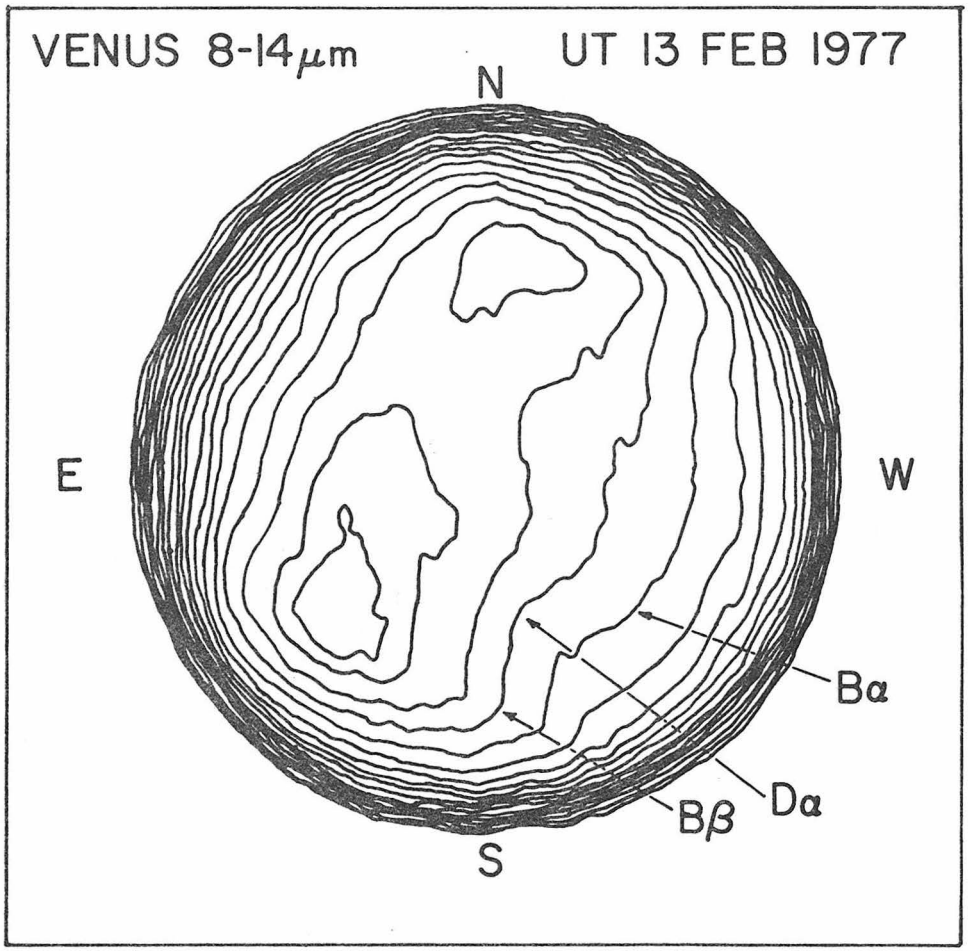
VENUS 8-14μm
UT 13 FEB 1977
N
E
W
Bα
Dα
Bβ
S

Fig. 8

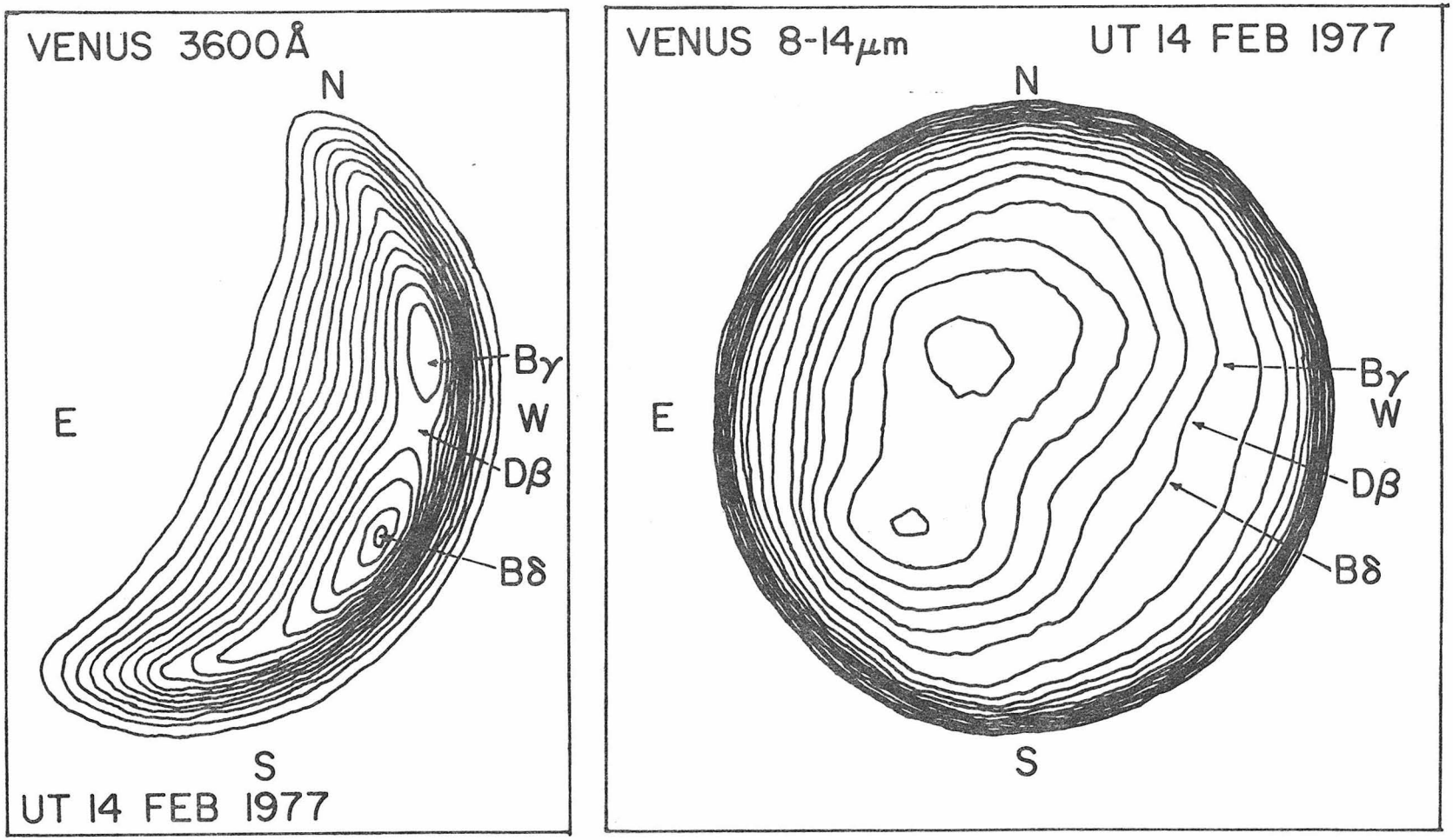
VENUS 3600Å
N
E
W
S
Bγ
Dβ
Bδ
UT 14 FEB 1977
VENUS 8-14μm
UT 14 FEB 1977
N
E
W
S
Bγ
Dβ
Bδ

Fig. 9

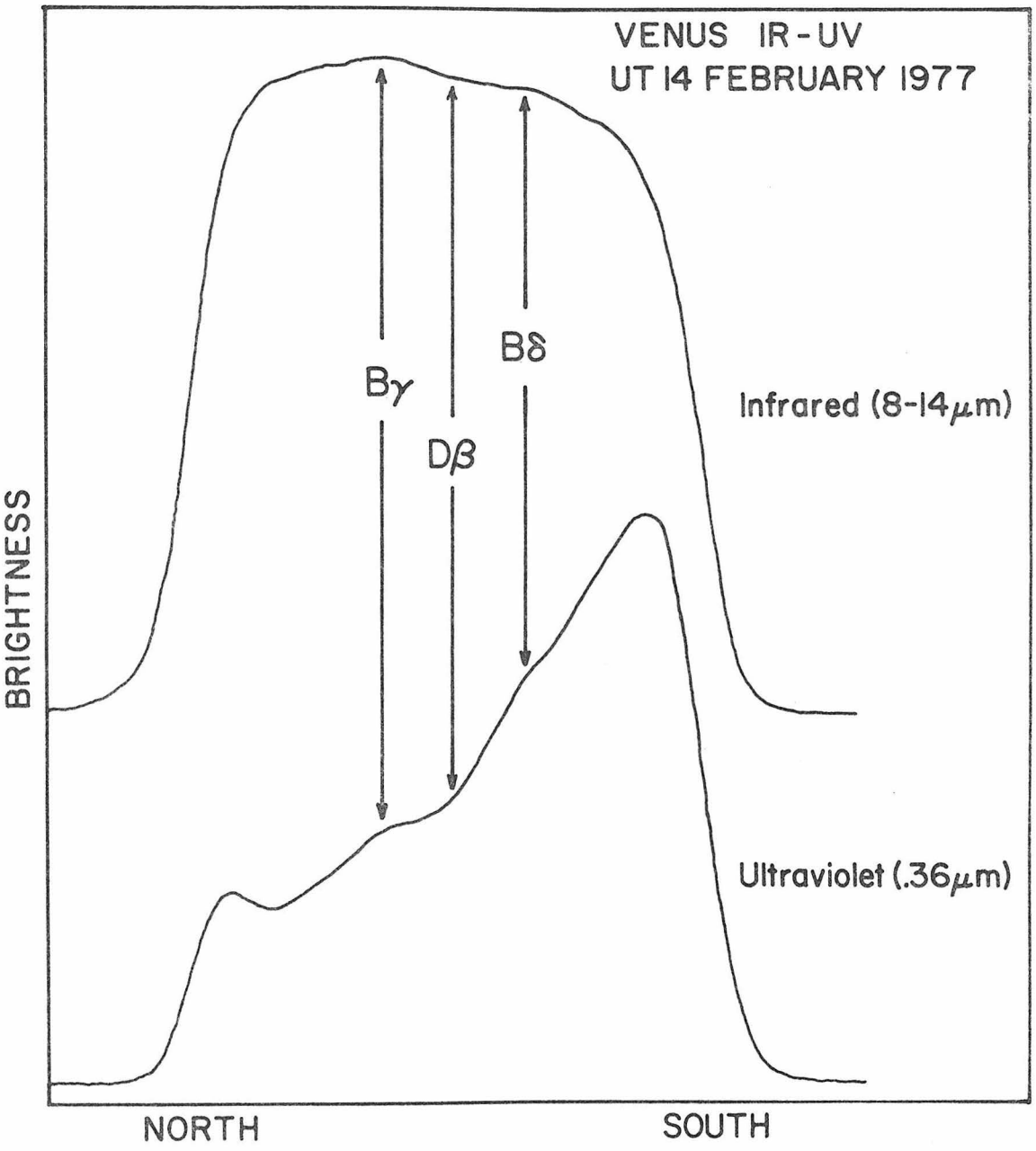
VENUS IR-UV
UT 14 FEBRUARY 1977
Bγ
Dβ
Bδ
Infrared (8-14μm)
Ultraviolet (.36μm)
BRIGHTNESS
NORTH
SOUTH

Fig. 10

locations on the Venus disk. Perhaps the simplest demonstration of a correlation between the UV and IR images is shown in this figure. Three features in the IR scan, two bright areas with an intervening dark region, correlate well with similar features in the UV scan, and the sense of the correlation is such that the bright IR areas, that is, the warmer regions, are relatively bright in the ultraviolet; similarly, the dark (cool) IR region correlates with a relatively dark UV area. The features seen in the UV-IR scan pair are also indicated in the corresponding contour maps (Figure 9) and may be seen in the images (Figure 7). Other UV and IR features correlate in the images and contour maps, with the correlation in the same sense as the features seen in the 14 February data.

Additional evidence for a UV-IR correlation is found in a set of images obtained on UT 26 September 1975 (Figure 11). In these data, a prominent northern polar "collar" was observed in the infrared images. The phase angle of Venus was 125° and the visual appearance of the planet in the telescope eyepiece indicated a sharper northern cusp relative to the southern cusp. The seeing was good (~1 arcsec) and the visible north-south asymmetry was verified in recorded UV images. Figure 12 shows contour maps of the UV-IR image pair from this date. The contours in the northern part of the ultraviolet crescent are clearly narrower and more pointed than the contours in the south. The north-south asymmetry in the 8-14 μm image is also quite apparent. This suggests that the phenomenon giving rise to the

Figure 11. (Left). Composite ultraviolet image from UT 26 September 1975. (Right). Composite 8-14 μm image from the same date. Celestial north is at the top; east is at the left. The northern cusp in the UV image is sharper (not as diffuse) as the southern cusp and a north polar anomaly is seen in the infrared image.

Figure 12. Contour maps of the images shown in Figure 11. The contour intervals are arbitrary. The contours in the northern hemisphere of the UV map are narrower and more pointed than the contours in the south. The presence of the infrared polar anomaly is apparent in the corresponding contour map and it may be seen that the anomaly (depression of the flux levels in the north) extends over much of the northern hemisphere.

Venus UT 26 Sept, 1975

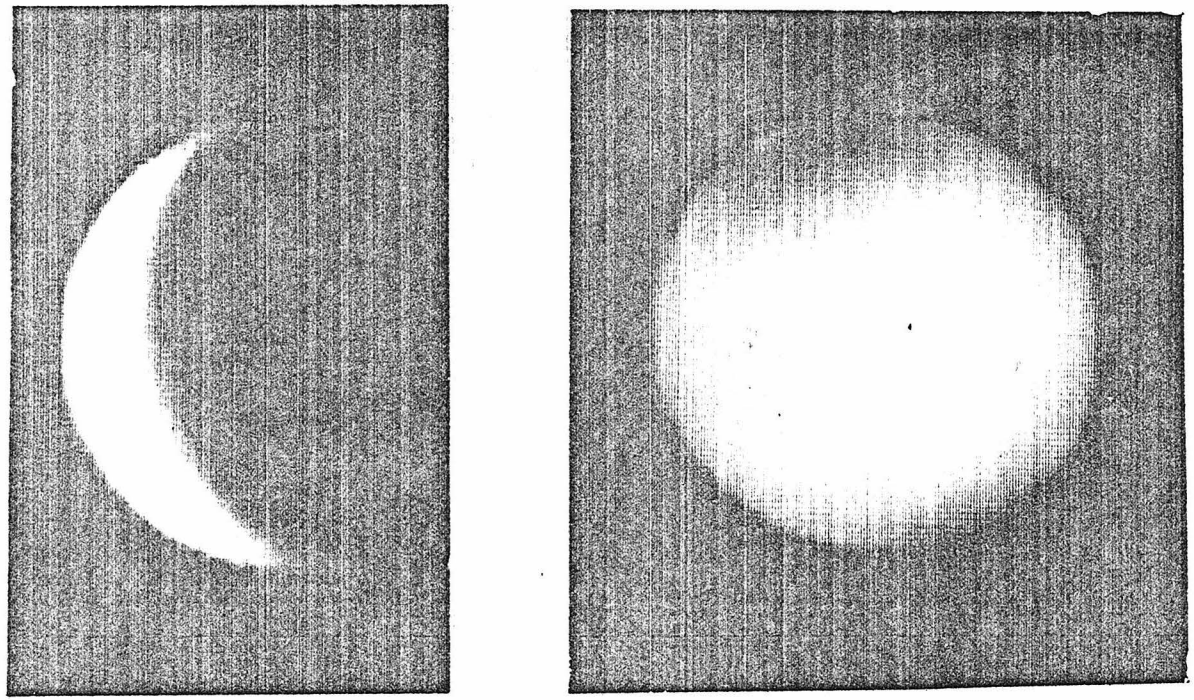

3600Å 8-14 μm

Fig. 11

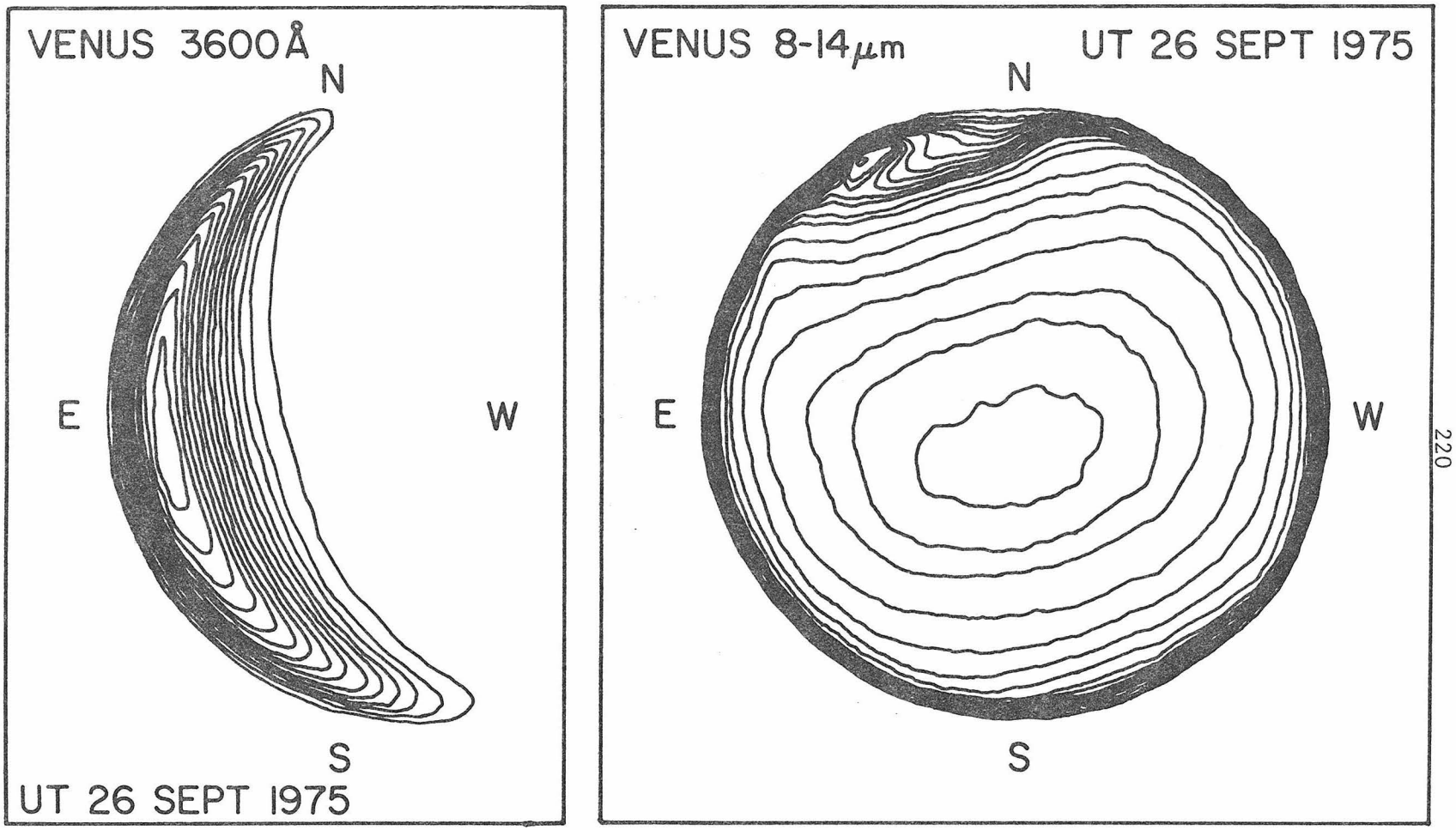
VENUS 3600Å
N
E
W
S
UT 26 SEPT 1975
VENUS 8-14μm
UT 26 SEPT 1975
N
E
W
S

Fig. 12

infrared polar anomaly may be seen in reflected sunlight, lending support to the hypothesis that this feature (and presumably other transient IR features) are due to varying opacity caused by clouds, and not thermal variations at constant pressure levels. A simple explanation for the north-south asymmetry in the UV image of 26 September is the presence of an ultraviolet absorber in the region which corresponds to the location of the infrared collar. This model is consistent with the dark UV-dark IR/bright UV-bright IR correlation suggested by the February 1977 images. It should be noted, however, that an alternative explanation is that the material whose presence gives rise to the IR collar causes greater limb-darkening in reflected light relative to regions where such material is in lower abundance or absent. This hypothesis does not necessarily require a difference in single scattering albedo between the particles which give rise to the bright and dark UV markings; instead, a difference in the shape of the single scattering phase functions would be implied.

Summarizing the observations, there is evidence that there is a dark UV-dark IR/bright UV-bright IR correlation between spatially resolved features on Venus, but the features in question are generally of extremely low contrast and the correlations are admittedly subtle. The observations presented here signal for a more extensive data base upon which this question may be pursued. The requirements for

such data must include: high spatial resolution; high signal-to-noise ratio (better than several hundred); and continuous temporal coverage. It is interesting to note that ultraviolet and infrared scans obtained by the Venera 9 and 10 orbiters (Ksanfomality, 1976) show a large number of small scale features in which a dark UV-dark IR/bright UV-bright IR correlation is exhibited. These features are on a considerably smaller spatial scale than the features observed in the ground-based images, but lend support to the existence of an ultraviolet-infrared correlation.

Some comments on the ramifications and implications of a dark UV-dark IR/bright UV-bright IR correlation are in order. These may be summarized as follows:

(1) The simplest interpretation of this correlation is that the dark clouds are cooler than the bright clouds and therefore exist at higher altitudes. A possible explanation for the predilection of dark clouds for higher average elevations is that dark areas absorb more sunlight than bright areas and therefore ascend to cooler regions as a result of convection. Alternatively, atmospheric turbulence may lead to upwelling in some areas, resulting in the formation of a material of low UV albedo, due to either a chemical change arising from lower ambient temperatures and pressures, or a photochemical change arising from greater exposure to energetic solar photons.

(2) A competing hypothesis of the UV-IR correlation is that the dark markings represent local concentrations of an ultraviolet-absorbing aerosol which is also a significant source of opacity at 8-14 μm and which exists at roughly the same altitude as the high UV albedo material. In this case, the time scale for production of the dark aerosol must be shorter than the time scale for turbulent mixing and homogenization of the two types of clouds. If the light and dark clouds are in radiative equilibrium with incident sunlight, the dark areas should be emitting more energy in the infrared. The opposite is the case, at least at 8-14 μm, implying that either the 8-14 μm region is atypical of the overall thermal emission, or lateral advection is playing a dominant role. If the latter is true, the dark UV markings would represent regions of lateral divergence of energy flux, and the bright areas would be regions of convergence.

(3) The infrared contrasts are on the order of 3% in intensity, corresponding to brightness temperature differences of about 1-2°K. If the bright and dark clouds are at different elevations, this temperature contrast corresponds to an altitude difference of less than 1 km, assuming a vertical temperature gradient of roughly -3°K/km. Although the region which contains the lower cloud would have a greater overlying gas abundance, the Rayleigh scattering optical depth increment implied by a 1 km height differential at the 10-50 mbar level

is of negligible importance. Thus, the infrared measurements support the conclusion that the ultraviolet contrasts cannot arise from differential Rayleigh scattering.

(4) Assuming that the IR polar anomaly is most prominent when the concentration of a dark UV absorber at these latitudes is greatest, the wavelength dependence of infrared opacity at 8-20 μm suggests that any candidate UV absorber must be more opaque at 20 μm than at 10 μm. Better observations at 20 μm and more extensive ultraviolet imaging on dates when a polar collar is present must be obtained in order to substantiate (or eliminate) this conclusion.

Chapter 5

SUMMARY AND CONCLUSIONS

"I can't believe that!" said Alice. "Can't you?" the Queen said in a pitying tone. "Try again: draw a long breath, and shut your eyes." Alice laughed. "There's no use in trying," she said: "one can't believe impossible things." "I daresay you haven't had much practice," said the Queen. "When I was your age, I always did it for half-an-hour a day. Why sometimes I've believed as many as six impossible things before breakfast."

- Lewis Carroll
Alice Through the Looking Glass

Simultaneous imaging of Venus in the 0.36 and 8-20 μm regions has led to the discovery of several interesting results concerning the structure of the upper atmosphere near 10-50 mbar. The following is a brief summary of the findings:

(1) The dependence of equatorial infrared brightness on longitude shows significant temporal variability although systematic asymmetries between the daytime and nighttime sides of the planet are present. The data in the vicinity of the evening terminator obtained during 1974-77 are in essential agreement with the 8-14 μm maps of Murray et al. (1963) and Westphal et al. (1965), the analysis of Ingersoll and Orton (1974), and Venera 9 and 10 orbiter results (Ksanfomality, et al., 1976) in that there is a gradual increase in thermal emission at low latitudes as the atmosphere emerges from daylight into evening. Systematically smaller asymmetries are observed on the morning side. A difference between the regions near the evening and morning terminators has also been seen in UV photographs

(O'Leary, 1974a), so it is reasonable to conclude that a fundamental difference in structure or dynamics is present between Venus' evening and morning sides. It is possible that near the equator the evening side is influenced by the convective subsolar region and represents an area of general downwelling.

(2) The equatorial limb-darkening is nearly wavelength independent in the 8-20 μm region. This spectral independence is consistent with an atmospheric model in which aerosol is distributed exponentially, and one need not require wavelength independence of the extinction cross section of the cloud particles. If the particles are assumed to be mixed homogeneously with the atmospheric gas, then the magnitude of the infrared limb-darkening implies a lapse rate of roughly -3°K/km. This value for the temperature gradient is intermediate between the results of the Mariner 5 and 10 radio occultation experiments (Fjeldbo et al., 1971; Howard et al., 1974; Nicholson and Muhleman, 1977).

(3) In contrast to the equatorial limb-darkening, the polar darkening is strongly wavelength dependent in the 8-20 μm region. The simplest explanation is that the atmosphere is meridionally inhomogeneous, such that the optical (i.e., spectrally dependent) properties of the polar and equatorial regions are dissimilar. This inhomogeneity may be maintained if atmospheric motions are primarily zonal, with little meridional mixing.

(4) An infrared south polar anomaly similar to that observed by Murray et al. (1963) appeared at that pole in 1974 but a similar feature occurred at the north pole in 1975. This type of feature is most prominent between Venus midnight and dawn, and its temporal variation may be due to the vertical motion of a polar cloud "collar." This collar is absent in the immediate vicinity of the pole. The thermal contrast between the "anomalous" pole and "normal" pole is wavelength independent in the 8-14 μm region, but there is evidence for a different temperature contrast in the 18-20 μm region.

(5) There are several examples of a correlation between ultraviolet and infrared features. The correlation matches dark UV features with dark (cool) IR features, and bright UV features with bright (warm) IR features. This correlation is consistent with Venera 9 and 10 orbiter scans (Ksanfomality, 1976), the marginal detection by Young (1974) of lower overall CO_2 abundance when dark UV features dominate the Venus disk, and the greater degree of polarization seen by Hapke (1974) over the bright regions in Mariner 10 ultraviolet images.

It is hoped that these observations will be supplemented and many of the questions resolved by the multichannel infrared radiometer and ultraviolet imaging experiments aboard the Pioneer 1978 Venus orbiter.

REFERENCES

American Ephemeris and Nautical Almanac (1962-1977). U.S. Government Printing Office, Washington, D.C.

Aumann, G., and Orton, G.S. (1977). The 12-24 μm spectrum of Venus. In preparation.

Carpenter, R.L. (1970). A radar determination of the rotation of Venus. Astron. J. 75, 61-66.

Chase, S.C., Miner, E.D., Morrison, D., Münch, G., and Neugebauer, G. (1974). Preliminary infrared radiometry of Venus from Mariner 10. Science 183, 1291-1292.

Coffeen, D.L. (1968). Venus cloud contrasts, in Planetary Atmospheres, IAU Symposium No. 40 (C. Sagan, T.C. Owen, and H.J. Smith, eds.) Reidel, Holland.

Coffeen, D.L., and Gehrels, T. (1969). Wavelength dependence of polarization. XV. Observations of Venus. Astron. J. 74, 433-445.

Coffeen, D.L., and Hansen, J.E. (1974). Polarization studies of planetary atmospheres. In Planets, Stars and Nebulae Studied with Photopolarimetry (T. Gehrels, ed.), University of Arizona Press, Tucson.

Diner, D.J., Westphal, J.A., and Schloerb, F.P. (1976). Infrared imaging of Venus: 8-14 micrometers. Icarus 27, 191-195.

Dyce, R.B., Pettengill, G.H., and Shapiro, I.I. (1967). Radar determination of the rotations of Venus and Mercury. Astron. J. 72, 351-359.

Fountain, J.W. (1974). Spatial distribution of polarization over the disks of Venus, Jupiter, Saturn, and the Moon. In Planets, Stars and Nebulae Studied With Photopolarimetry (T. Gehrels, ed.), University of Arizona Press, Tucson.

Fjeldbo, G., Kliore, A.J., and Eshleman, V.R. (1971). The neutral atmosphere of Venus as studied with Mariner V radio occultation experiments. Astron. J. 76, 123-140.

Gillett, F.C., Low, F.J., and Stein, W.A. (1968). Absolute spectrum of Venus from 2.8 to 14 microns. J. Atmos. Sci. 25, 594-595.

Goldstein, R.M. (1966). Radar studies of Venus. In Moons and Planets (A. Dollfus, ed.), North-Holland, Amsterdam.

Hansen, J.E., and Arking, A. (1971). Clouds of Venus: Evidence for their nature. Science 171, 669-672.

Hansen, J.E., and Hovenier, J.W. (1974). Interpretation of the polarization of Venus. J. Atmos. Sci. 31, 1137-1159.

Hansen, J.E., and Travis, L.D. (1974). Light scattering in planetary atmospheres. Space Sci. Rev. 16, 527-610.

Hapke, B. (1974). The Atmosphere of Venus. Proceedings of a conference held at Goddard Institute for Space Studies, New York, pp. 69-76.

Howard, H.T., Tyler, G.L., Fjeldbo, G., Kliore, A.J., Levy, G.S., Brunn, D.L., Dickinson, R., Edelson, R.E., Martin, W.L., Postal, R.B., Seidel, B., Sesplaukis, T.T., Shirley, D.L., Stelzried, C.T., Sweetnam, D.N., Zygielbaum, A.I., Esposito, P.B., Anderson, J.D., Shapiro, I.I., and Reasenberg, R.D. (1974). Venus: Mass, gravity field, atmosphere, and ionosphere as measured by the Mariner 10 dual-frequency radio system. Science 183, 1297-1301.

Ingersoll, A.P., and Orton, G.S. (1974). Lateral inhomogeneities in the Venus atmosphere: Analysis of thermal infrared maps. Icarus 21, 121-128.

Ksanfomality, L.V. (1976). Infrared thermal measurements from the artificial satellites of Venus. Publication 226 of the Space Research Institute of the Academy of Sciences, USSR.

Ksanfomality, L.V., Dedova, E.V., Obukhova, L.F., Pokras, V.M., Temnaya, N.V., and Filippov, G.F. (1976). Thermal asymmetry of Venus. Sov. Astron. 20, 476-480.

Kunde, V.G. (1976). Private communication.

Martonchik, J.V. (1974). Sulfuric acid cloud interpretation of the infrared spectrum of Venus. Astrophys. J. 193, 495-501.

Murray, B., Wildey, R.L., and Westphal, J.A. (1963). Infrared photometric mapping of Venus through the 8- to 14-micron atmospheric window. J. Geophys. Res. 68, 4813-4818.

Murray, B.C., Belton, M.J.S., Danielson, G.E., Davies, M.E., Gault, D., Hapke, B., O'Leary, B., Strom, R.G., Suomi, V., and Trask, N. (1974). Venus: Atmospheric motion and structure from Mariner 10 pictures. Science 183, 1307-1315.

Nicholson, P.D., and Muhleman, D.O. (1977). Independent radio-occultation studies of Venus' atmosphere. Preprint.

O'Leary, B. (1974a). The Atmosphere of Venus. Proceedings of a conference held at Goddard Institute for Space Studies, New York, p. 67.

O'Leary, B. (1974b). The Atmosphere of Venus. Proceedings of a conference held at Goddard Institute for Space Studies, New York, p. 129.

Orton, G.S. (1975). Private communication.

Palmer, K.F., and Williams, D. (1975). Optical constants of sulfuric acid. Applications to the clouds of Venus? Appl. Opt. 14, 208-219.

Pollack, J.B., Erickson, E.F., Witteborn, F.C., Chackerian, C., Jr., Summers, A.L., Van Camp, W., Baldwin, B.J., Angason, G.C., and Caroff, L.J. (1974). Aircraft observations of Venus' near-infrared reflection spectrum: Implications for cloud composition. Icarus 23, 8-26.

Ross, F. (1928). Photographs of Venus. Astrophys. J. 68, 57-92.

Samuelson, R.E., Hanel, R.A., Herath, L.W., Kunde, V.G., and Maguire, W.C. (1975). Venus cloud properties: Infrared opacity and mass mixing ratio. Icarus 25, 49-63.

Shapiro, I.I. (1967). Resonance rotation of Venus. Science 157, 423-425.

Sill, G.T. (1972). Sulfuric acid in the Venus clouds. Comm. Lunar Planet. Lab. 171, 191-198.

Sinton, W.M., and Strong, J. (1960). Radiometric observations of Venus. Astrophys. J. 131, 470-490.

Suomi, V. (1974). The Atmosphere of Venus. Proceedings of a conference held at Goddard Institute of Space Studies, New York, pp. 42-58.

Taylor, F.W. (1975). Interpretation of Mariner 10 infrared observations of Venus. J. Atmos. Sci. 32, 1101-1106.

Travis, L.D. (1975). On the origin of ultraviolet contrasts on Venus. J. Atmos. Sci. 32, 1190-1200.

Westphal, J.A. (1971). Limb darkening observations of Venus from 5μ to 18μ. In Planetary Atmospheres, IAU Symposium No. 40 (C. Sagan, T.C. Owen, and H.J. Smith, eds.) Reidel, Holland.

Westphal, J.A. (1973). Application of the SIT vidicon to astronomical measurements. In Astronomical Observations with Television-Type Sensors (J.W. Glaspey and G.A.H. Walker, eds.), University of British Columbia, Vancouver.

Westphal, J.A. (1975). Private communication.

Westphal, J.A., Wildey, R.L., and Murray, B.C. (1965). The 8-14 micron appearance of Venus before the 1964 conjunction. Astrophys. J. 142, 799-802.

Westphal, J.A., Matthews, K., and Terrile, R.J. (1974). Five-micron pictures of Jupiter. Astrophys. J. 188, L111-L112.

Wright, W.H. (1927). Photographs of Venus made by infrared, and by violet light. Publ. Astron. Soc. Pac. 39, 220-221.

Young. A.T. (1973). Are the clouds of Venus sulfuric acid? Icarus 18, 564-582.

Young. A.T. (1974). The Atmosphere of Venus. Proceedings of a conference held at Goddard Institute for Space Studies, New York, pp. 15-16.